Investigation of Wavelength Tunable Lasers for use in Coherent Optical Communication Systems

Kai Shi

B.Sc., M.Eng.

A Dissertation submitted in fulfilment of the

requirements for the award of

Doctor of Philosophy (Ph.D.)

to the

Dublin City University

Faculty of Engineering and Computing

School of Electronics Engineering

Supervisor: Prof. Liam P. Barry

May 3, 2012

Declaration

I hereby certify that this material, which I now submit for assessment on the programme of study leading to the award of Doctor of Philosophy (PhD) is entirely my own work, and that I have exercised reasonable care to ensure that the work is original, and does not to the best of my knowledge breach any law of copyright, and has not been taken from the work of others save and to the extent that such work has been cited and acknowledged within the text of my work.

Signed:

Student ID: 57128120

Date:

Abstract

The phase noise of wavelength tunable semiconductor lasers is becoming increasingly more important in fast optical switching networks employing advanced modulation formats. The objective of this thesis is to develop techniques to investigate the phase noise of different types of tunable lasers, and investigate the performance of these devices when used in dynamic coherent networks. Specifically sampled-grating distributed Bragg reflector (SG-DBR) lasers and a three-section tunable slotted Fabry-Pérot (SFP) laser are studied in this thesis. The optical linewidth of the devices is measured using a standard delayed self-heterodyne method and a new measurement technique using an optical quadrature front end. The effect of laser phase noise in system environments is examined by employing the lasers in a static 1.25 Gbit/s differential binary phase shift keying (DPSK) transmission system and a 10.7 Gbaud differential quadrature phase shift keying (DQPSK) packet switching system.

The work presented in this thesis also introduces a new method for calibrating SG-DBR lasers to achieve the best possible phase noise. The method is based on using the voltage signal of the gain section of the SG-DBR laser, and can achieve a linewidth reduction of up to 80% compared to techniques that only calibrate for the side-mode suppression ratio (SMSR) and the output power of SG-DBR lasers. The results in this thesis show the importance of characterization of laser phase noise when tunable lasers are used in dynamic coherent systems.

Acknowledgements

First and foremost, I would like to thank my supervisor Prof. Liam Barry for providing me with the opportunity to come to Ireland and undertake research in the Radio and Optical Communication Group in Dublin City University (DCU), which has been one of the most enjoyable experiences of my life. Without his continued motivation and support the completion of this work would have been impossible.

Another person I would like to thank is Prof. Yonglin Yu, from Wuhan National Lab for Optoelectronics (WNLO), for her supervision and kind help of my career during my master study in China. If it had not been for her introduction, it is unlikely that I would have been involved in the area of optical communications and obtained such a great chance to study abroad.

I would like to acknowledge Eamonn, Regan and Kevin for their time and kind help of the quality check while I am writing the thesis. I must also thank those whom I have collaborated with in Tyndall National Institute, the Optical Networks Group in University College London and in WNLO.

I would also like to thank all the past and present members of the Radio and Optical Communications Group and Brendan in the Vision Systems Group (VSG) lab for their friendship, constructive advice and support. Those pleasurable trips, soccer matches, dinners, games, GAA matches and other things that I have been to with you and your hospitable families and friends significantly alleviated my homesickness for the past four years. Without your friendship both in and outside the lab, the completion of this thesis would have been considerably more difficult.

Finally, I would like to thank my friends and family, especially my parents, for their commitment, support and encouragement throughout my 'eternal' education. It is to these people that this thesis is dedicated.

Contents

Abstract ii

Acknowledgements iii

List of Figures vii

List of Tables xii

Acronyms xiii

1 Introduction 1

References 5

2 High Speed Optical Communication Networks 6

2.1 Optical Switching 7

2.1.1 Fixed-Wavelength Networks with OADM 7

2.1.2 Reconfigurable Networks 8

2.1.3 Optical Burst Switching and Optical Packet Switching 9

2.2 Advanced Modulation Formats 11

2.2.1 Direct Modulation 12

2.2.2 External Modulation with MZMs 13

2.2.3 Self-coherent and Coherent Detection 16

2.2.4 Signal Degradations 17

2.3 Summary 19

References **20**

3 Tunable Semiconductor Lasers **25**

3.1 Fundamental Concepts of Tunable Semiconductor Lasers 26

3.1.1 The Fabry-Pérot Laser 26

3.1.2 Bragg Grating 28

3.1.3 Tuning Mechanisms 30

3.2 Fast Switching Widely Tunable Lasers 32

3.2.1 The Vernier Effect 32

3.2.2 Wavelength Switching 36

3.3 Summary 40

References **42**

4 Characterization of SG-DBR Lasers **47**

4.1 Laser Phase Noise 48

4.1.1 White FM Noise 48

4.1.2 Additional FM Noise 52

4.1.3 Phase Noise Characterization Methods 53

4.2 Phase Noise Characterization of SG-DBR Lasers 55

4.2.1 Effect of Linewidth on DPSK System 55

4.2.2 Linewidth Characterization Results 58

4.2.3 Linewidth Calibration Technique 60

4.3 Dynamic linewidth and Time-resolved BER 64

4.3.1 Linewidth Characterization Using an Optical Quadrature Frontend . 64

4.3.2 Static Linewidth 66

4.3.3 Dynamic Linewidth 68

4.3.4 Time Resolved BER 70

4.4 Summary 73

References **75**

5 A Three-Section Tunable Slotted Fabry-Pérot Laser **78**

5.1 Characterization of the SFP Laser 79

5.1.1 Device Structure and Operation 79

5.1.2 Device Characterization 84

5.2 Applications of SFP Lasers in Dynamic Coherent Networks 86

5.2.1 Static DPSK Transmission 86

5.2.2 Wavelength Switching 88

5.2.3 Time Resolved BER 93

5.3 Summary 95

References **97**

6 Conclusion and Future Research **100**

Conclusion 100

Future Research 102

A List of Publications Arising From This Work **104**

A.1 Referred Journals 104

A.2 Conference Papers 106

List of Figures

2.1 A ring topology with OADMs and a head end. 8

2.2 Flexible wavelength provisioning with tunable lasers and filters. 9

2.3 An OPS forwarding module. 10

2.4 (a) Direct modulation of a laser. (b) Optical spectra of the directly and externally modulated signal 12

2.6 The optical intensity eye diagrams 14

2.6 The constellation diagrams for (d) OOK. (e) BPSK. (f) QPSK. 15

2.7 Structure of a delayed interferometer and an optical quadrature front end for self-coherent and coherent detection 16

2.8 Eye diagram for DQPSK system for a laser frequency offset Δf equals to (a) 0 and (b) 2% of the bit rate. 18

2.9 The constellation diagrams for (a) 1.25G baud DQPSK with $\Delta\nu$=5MHz. (b) 10 Gbaud DQPSK with $\Delta\nu$=50MHz. (c) 10 Gbaud D8PSK with $\Delta\nu$=50MHz. 19

3.1 Propagation and reflection in a "square" grating. (Adapted from [2]). The matrices describe the two elementary parts of the refractive index step and the homogeneous waveguide. 28

3.2 Power reflectivity of (a) a DBR and (b) an SG-DBR 29

3.3 Examples of tunable lasers types: (a) ECL, (b) MEMS/VCSEL, (c) selectable DFB array. adapted from [10] 30

3.4 Structure diagram of an SG-DBR laser with integrated SOA. 33

3.5 Power reflectivity of SG-DBRs with two different lengths of sampling period, which are 58 μm (red line) and 64 μm (blue line). Lasing occurs where the maxima of R_f (front grating) and R_b (back grating) are aligned. The tuning current on the front grating is 15 mA in (a) and (b), and 24 mA for (c) and (d). 34

3.6 Wavelength tuning curve of a SG-DBR laser. (a)3-D surface obtained by varying both the front and back SG-DBR current. (b)The contour of the 3-D curve in (a). Colour is used to delineate the wavelength. 35

3.7 (a) A static tuning curve of the switching range. (b) A brief illustration of the mode competition of the three areas in (a) 37

3.9 Time response of the carrier density of the front SG-DBR by a pulse-current with two different high levels (inset). 39

4.1 (a) The instantaneous changes of the phase, ϕ, and intensity, I, of the optical field caused by the i th spontaneous emission event (adapted from [1]). (b) Complex amplitude, E, for laser light. 49

4.2 (a) The mean square value of the phase change. (b) The FM-noise spectrum. (c) The field spectrum. 51

4.3 (a) Experimental setup of the linewidth characterization using the delayed self-heterodyne method. (b) Measured lineshape of the SG-DBR laser with a linewidth of 19.8 MHz (□) and 4.6 MHz (♢). The lineshape is also fitted with a Lorentzian (solid black line), a Gaussian (purple dots) and a Voigt (green dashes) function respectively. 54

4.4 Experimental setup for DPSK transmission system. 56

4.5 BER of 1.25 Gb/s DPSK transmission using a SG-DBR laser at 194.2 THz channel with a linewidth of 19.8MHz (♦) and 4.6MHz (■). The inset shows the received eye at power of -41.8 dBm for the two linewidth. 57

4.6 The tuning maps of the SG-DBR laser versus front and back grating currents. (a) Linewidth. (b) Wavelength. 58

4.7 Operating points (filled circles) with (a) highest SMSR and (b) lowest linewidth in different longitudinal modes. The arrows indicate the modes to which the operating points belong. 59
4.8 Voltage across the active section of the SG-DBR laser and the minimum points inside each longitudinal mode (black dots). 59
4.9 (a) Signal plane V3 with sharpened mode boundaries. (b) Signal plane V5 after removing the gradually varying trend. 62
4.10 Histogram of linewidth reduction between the operating points with highest SMSR and narrowest linewidth. 63
4.11 Setup of the linewidth characterization using a delayed self-homodyne technique with an optical quadrature front end. 64
4.12 (a) Derived linewidths (♦) using this method and the DSH linewidth (■) of an SG-DBR laser (left) and a DFB laser (right) as a function of 1/power. (b) FM-noise spectrum measured at P=1 mW. 67
4.13 (a) Wavelength variation during the switching of the signal and the delayed replica. (b) Measured in phase and quadrature photocurrent. (c) Schematic illustration of dynamic linewidth measurement. 68
4.14 Dynamic linewidth of two different switching combinations. 70
4.15 Experimental setup of time resolved bit error rate (BER) measurement. The inset shows the timing diagram at points a, b and c. 71
4.16 (a) BER vs received power in static scenario, (b) time resolved BER in switching scenario. 71
4.17 (a) Frequency offset. (b) Measured data packets and maximum error free gating pulses. 72

5.1 (a) Mask layout of the device. (b) Longitudinal structure of the three-section SFP laser. 80

5.2 (a) Power versus current characteristic under different bias combinations. Ib, Im and If represent the current on the back, middle and front section respectively. (b) Temperature sensitivity of two different modes (■ and ●). The solid lines represent the lasing wavelength while the dotted lines represent the corresponding SMSR. 81

5.3 Wavelength (solid line) and corresponding SMSR (dotted line) tuning curves versus (a) voltage across the front section and (b) total voltage across both the middle and the back sections equally. The squares represent the chosen switching points. (c) 3D wavelength tuning map. (d) 3D SMSR tuning map. 83

5.4 Schematic diagram illustrating the potential cavity modes inside different sections of the SFP laser. 83

5.5 (a) Optical spectrum at different ITU channels. The inset shows the spectrum of the channel at 192.6 THz. (b) The RIN spectra of six ITU channels with different launch powers. Data is averaged over 20 sweeps. 85

5.6 (a) Drive currents on each section and the output power of different ITU channels. (b) Linewidth and SMSR at different ITU channels. The dotted lines show the average values. 86

5.7 Experimental setup of the DPSK transmission system. 87

5.8 BER of 1.25 Gb/s DPSK transmission using (a) the SFP laser, and (b) the SG-DBR laser 87

5.9 Experimental setup of wavelength switching using tunable filter method (dotted line B) and self heterodyne method (solid line A). 88

5.10 Switching waveforms of different modes when the SFP laser is switched from (a) $\lambda 1$ to $\lambda 7$ and (b) $\lambda 7$ to $\lambda 1$ in Figure 5.3a, (c) $\lambda 2$ to $\lambda 4$ and (d) $\lambda 4$ to $\lambda 2$ in Figure 5.3b. 90

5.11 Beating signal generated when the laser get into 1.87 GHz range of the target frequency (a) $\lambda 4$ and (b) $\lambda 2$ in Fig. 2 (b). The dotted lines represent the beginning of the switching event. 92

5.12 Histogram of the switching time of different switching combinations. . . . 93

5.13 Experimental setup of time resolved BER measurement. 93

5.14 (a) Oscilloscope traces of the in-phase components of received packets at the end of the 192.8 THz packet and the beginning of the 193.0 THz packet. (b). Time resolved BER as the laser switches between 198.2 THz and 193 THz. 94

List of Tables

4.1 Drive currents for the two operation points 56

5.1 Switching Combination (TOF Method/Self Heterodyne Method) 92

Acronyms

3-D three-dimensional. 34

AOLS all-optical label swapping. 10, 11

ASE amplified spontaneous emission. 56

BD balanced detector. 65

BER bit error rate. ix, 3, 18, 48, 57, 70–74, 87, 88, 94, 96, 100–102

BL bit rate-distance product. 6, 7

BPSK binary phase shift keying. 14–16

CD chromatic dispersion. 12

CoWDM coherent wavelength division multiplexing. 15

CW continuous wave. 17, 65, 101

CWDM coarse WDM. 11

DAQ data acquisition. 63

DBR distributed Bragg reflector. 29, 31, 32, 61, 79, 95

DFB distributed-feedback. 29, 31, 32, 66, 67, 86

DP dual-polarization. 15

DPSK differential binary phase shift keying. ii, viii, 2, 3, 16–18, 47, 55–57, 74, 86, 95, 100, 102

DQPSK differential quadrature phase shift keying. ii, 2, 3, 16–18, 48, 70, 72, 73, 86, 94–96, 100–102

DS-DBR digital supermode distributed Bragg reflector. 36

DSH delayed self-homodyne. 64, 67, 74

DSMSR dynamic side-mode suppression ratio. 39, 40

DSP digital signal processing. 17

DWDM dense WDM. 1, 11, 91

ECL external-cavity laser. 30, 31, 40

ED error detector. 71, 100

EDFA erbium-doped fibre amplifier. 7, 32, 56, 66, 88

ESA electrical spectrum analyser. 53, 54, 84

FP Fabry-Pérot. 25–28, 40, 79

FWHM full-width half-maximum. 17, 48, 51–53, 64

GACC grating-assisted co-directional coupler. 36

GCSR Grating assisted co-directional Coupler with Sampled Reflector. 36, 90

IF intermediate frequency. 53, 54

IMDD intensity modulation/direct detection. 16

IP Internet Protocol. 10

IQ in-phase and quadrature. 13–15, 72

IRSN injection-recombination shot noise. 52, 53, 73

ITU international telecommunication union. 3, 11, 31, 55, 56, 60, 62, 84, 91, 95

LO local oscillator. 16–18, 53

MDI Michelson delay interferometer. 56

MEMS micro-electromechanical system. 30

MGY modulated Y-structure. 36

MZDI Mach-Zehnder delay interferometer. 16, 72, 73

MZI Mach-Zehnder interferometer. 16

MZM Mach-Zehnder modulator. 13–15, 55

OADM optical add-drop multiplexer. 8, 9

OBPF optical bandpass filter. 1, 11, 56

OBS optical burst switching. 3, 10, 19, 31, 41

OEO opto-electronic-opto. 6–8, 11

OFDM orthogonal frequency division multiplexing. 15

OOK on-off keying. 12, 14–16, 41, 47, 60, 95

OPS optical packet switching. 3, 10, 19, 31, 41, 78

OSNR optical signal-to-noise ratio. 17

PC polarization controller. 65

PG pulse generator. 70

PM phase modulator. 13

PMD polarization-division multiplexing. 15

PMD polarization-mode dispersion. 12

PPG pulse pattern generator. 56, 72, 94

PRBS pseudorandom bit sequence. 56, 72

PSD power spectral density. 17, 50, 51, 53, 67

PSK phase shift keying. 93

PtP point-to-point. 7

QAM quadrature amplitude modulation. 15, 102

QPSK quadrature phase shift keying. 15

QW quantum well. 79

RIN relative intensity noise. 79, 84, 95

ROADM reconfigurable OADM. 9, 11, 19

SE spectral efficiency. 1, 6, 7, 12, 15, 19, 47

SFP slotted Fabry-Pérot. ii, 2, 3, 78, 79, 82, 84–89, 91, 94–96, 100–102

SG-DBR sampled-grating distributed Bragg reflector. ii, viii, 2, 3, 29, 32–37, 39–41, 47, 48, 53–55, 57, 58, 60–64, 66–70, 74, 78, 82, 84–88, 90, 93, 94, 96, 100–102

SMF single mode fibre. 54, 66, 88, 91

SMSR side-mode suppression ratio. ii, 3, 25, 29, 35–37, 39–41, 47, 55, 57, 59–63, 74, 78, 79, 82, 84–86, 95, 101

SOA semiconductor optical amplifier. 39, 63, 84, 91

SSG-DBR superstructure-grating distributed Bragg reflector. 30, 35, 36, 61

TEC thermoelectric cooler. 79, 82

TIA transimpedance amplifier. 84

TMM transfer matrix method. 29, 30, 38, 40

TOF tunable optical filter. 2, 3, 89, 92, 93, 102

Tx transmitter. 9

ULH ultra-long haul. 7

VCSEL vertical-cavity surface-emitting laser. 30, 31, 40

VOA variable optical attenuator. 56

Vpp peak-to-peak amplitude. 89, 94

WDM wavelength-division multiplexing. 1, 6, 7, 11, 19, 25, 32, 39, 40, 47

Chapter 1

Introduction

Today's network services such as high-speed internet access and video entertainment have driven the traffic growth of the internet, which continues at a rate of about 50% per year, without showing signs of slowing [1]. To accommodate these bandwidth demands, network carriers have employed wavelength-division multiplexing (WDM) techniques to exploit the capacity of an optical fibre. As the channel spacing in dense WDM (DWDM) systems is limited by the symbol rate and the bandwidth of optical bandpass filters (OBPFs) in the link, advanced modulation formats with high spectral efficiency (SE) are desired to increase the data rate on each DWDM channel while maintaining the full bandwidth allocation [2]. In addition, at each node of the network all entering wavelength channels are required to be electronically terminated. As traffic levels grow, deploying the necessary electronics at each node becomes very costly [1, 3]. Optically switched networks such as burst or packet switched networks, providing sub-wavelength granularity, allow automated reconfigurability and reduce network latency. This has been shown to significantly facilitate limitations such as the speed and power consumption of electronics at the routers [3].

Widely tunable lasers with fast wavelength switching is a key component in reconfigurable optical networks. As dynamic networks begin to employ advanced modulation formats, the phase noise of the laser is becoming more important. The overall objective of this thesis is to study the phase noise of two types of tunable semiconductor lasers and investigate their performance in dynamic coherent networks. The phase noise is characterized us-

ing the standard delayed self-heterodyne technique and a new method employing an optical quadrature front end. The dynamic linewidth of the sampled-grating distributed Bragg reflector (SG-DBR) laser during a switching event is also investigated using the new method, while wavelength switching dynamics of the three-section slotted Fabry-Pérot (SFP) laser are characterized using a tunable optical filter (TOF) method and a self-heterodyne method. The effect of the laser phase noise in phase modulated systems using differential detection is examined by utilizing the two lasers as a transmitter in both a 1.25 Gbit/s differential binary phase shift keying (DPSK) transmission system and a 10.7 Gbaud differential quadrature phase shift keying (DQPSK) packet switching system. The major contributions of this work are:

- Development of a new phase noise measurement method — With the in-phase and quadrature components of the optical field being recovered using an optical quadrature front end. The FM-noise spectrum of the laser phase noise can be calculated, where different types of noise can be distinguished. The derivation of the instantaneous phase of the laser during a wavelength switching event allows the phase noise dynamics to be investigated.

- Characterization of the performance of tunable lasers in coherent optically switched networks — The effect of laser linewidth and a new calibration method for archiving narrow linewidth is presented. The feasibility of using two types of tunable lasers in dynamic self-coherent networks with nanosecond scale latency is demonstrated.

- Detailed characterization of a novel discretely tunable laser with two single slots structure — The single growth fabrication reduces the cost and complexity. The SFP laser is found to exhibit much narrower linewidth compared to the SG-DBR laser. Fast wavelength switching is also achieved for different switching combinations using two different measurement techniques.

The thesis is structured as follows:

Chapter 2 outlines different architectures of optical switching. The wavelength tunable semiconductor lasers are shown to be a key component in the switching node, which enable

different switching functions with different required switching times. Within this section, different modulation and detection schemes for both intensity and phase modulation formats are studied. The importance of laser phase noise and other impairments which degrade the system performance are studied through simulation.

Chapter 3 introduces the fundamentals of tunable semiconductor lasers. Current tuned lasers which use the free-carrier plasma effect are found to be suitable for fast switching functions such as optical packet switching (OPS) and optical burst switching (OBS). SG-DBR lasers using the Vernier effect is demonstrated to be an ideal candidate in reconfigurable networks with a wide tuning range and nanosecond scale switching time.

Chapter 4 explores the phase noise characteristics of SG-DBR lasers. The linewidth broadening due to the additional FM-noise in the passive sections of the devices is investigated. The effect of the laser linewidth is shown by comparing the performance of a 1.25 Gbit/s DPSK system. The optical linewidth of the SG-DBR lasers measured using the standard delayed self-heterodyne method is found to be correlated with the voltage of the gain section. Consequently, a linewidth calibration method is developed to locate the operating points with the lowest linewidth instead of the highest side-mode suppression ratio (SMSR). The dynamic linewidth of the SG-DBR laser is measured using a time domain technique, by which the instantaneous phase of the optical field is recovered. The importance of the frequency offset in self-coherent systems is demonstrated through the employment of a time resolved bit error rate (BER) measurement of a DQPSK packet switching system.

Chapter 5 focuses on the characterization of the three-section tunable SFP laser. Twenty five available channels at 100 GHz international telecommunication union (ITU) grid spacings are presented, with SMSR above 30 dB and linewidth below 800 kHz for all channels. The narrow linewidth benefits of the SFP laser compared to the SG-DBR laser is investigated in the 1.25 Gbit/s DPSK transmission system experiment. The wavelength switching dynamics of the SFP laser is examined with the TOF method and the self-heterodyne method. The time resolved BER measurement of a 10.7 Gbaud DQPSK packet switching system utilizing the SFP laser is also presented.

Chapter 6 presents a brief conclusion and provides some directions for future investigation.

Finally, Appendix A presents a list of the author's publications arising from this work.

References

[1] J. Berthold, A. A. Saleh, L. Blair, and J. M. Simmons, "Optical networking: Past, present, and future," *Journal of Lightwave Technology*, vol. 26, no. 9, pp. 1104–1118, May 2008.

[2] P. J. Winzer and R. J. Essiambre, "Advanced modulation formats for High-Capacity optical transport networks," *Journal of Lightwave Technology*, vol. 24, no. 12, pp. 4711–4728, Dec. 2006.

[3] L. A. Coldren, "High-performance photonic integrated circuits (PICs)," in *Optical Fiber Communication (OFC), collocated National Fiber Optic Engineers Conference, 2010 Conference on (OFC/NFOEC)*. IEEE, Mar. 2010, pp. 1–52.

Chapter 2

High Speed Optical Communication Networks

The research of modern optical communication systems started around the 1970s thanks to two key developments in optical fibres and associated semiconductor lasers. These were the reduction of loss of fibre to 20 dB/km in 1970 [1] and the successful demonstration of room-temperature operation of a heterostructure laser in 1969 [2]. Ever since, there has been enormous progress in fibre-optics communication systems corresponding to a doubling of the bit rate-distance product (BL) every year [3]. The architecture and functionality of the optical networks have evolved accordingly to accommodate the increasing data rate requirement, with the advent of new technologies such as optical amplification and wavelength-division multiplexing (WDM). However, as the channel number of WDM systems keeps increasing, the channel spacing between adjacent channels is limited by the bandwidth of the optical amplifiers. The focus of current systems is on increasing the spectral efficiency (SE), which refers to the information rate that can be transmitted over a given bandwidth in a specific WDM system. Meanwhile the use of the multiplexing techniques makes today's single rack electronic routers impossible to handle the state-of-the-art single fibre capacity due to the power consumption and high speed electronics [4]. Switching techniques which route the high speed optical packets without opto-electronic-opto (OEO) conversion are becoming critical for reducing the latency in future optical networks. In this chapter, the switching

architecture and the advanced modulation formats will be described, which will be used in future agile networks with low latency and high SE.

2.1 Optical Switching

Optical networks were first used to transport information between electronic switching systems connected over point-to-point (PtP) links due to the advantages of the low loss and high capacity of optical fibre. The optical signal is converted to an electronic signal and then back to an optical signal, after a specific length of fibre, in order to regenerate the signal which is degraded due to the fibre loss, dispersion and nonlinearity. With the advent of the erbium-doped fibre amplifier (EDFA), signals on multiple wavelengths, as in WDM systems, are amplified simultaneously, which significantly increases the spacing between the optoelectronic repeaters. The predominant limitation of the BL product has been shifted from the fibre loss to dispersion and nonlinear effect [5]. However, the signal broadening caused by the fibre dispersion can be managed in practice through a suitable dispersion compensation scheme [3]. The progress in optical networks has increased the aggregate data rate per single fibre dramatically and makes PtP links suitable for ultra-long haul (ULH) systems. On the other hand, at the edge of the ULH network or at the nodes of WDM metro networks, the optical signal needs to be converted and switched by using electronic equipment [6]. Therefore, the continuing increase of the data rate per fibre will significantly expand the complexity and cost of the electronic routers. In this section, different optical switching techniques will be introduced, which are used to mitigate the bottleneck of high speed optical communication systems caused by the low speed electronics.

2.1.1 Fixed-Wavelength Networks with OADM

In order to avoid the OEO conversion at each node of the WDM systems, the data needs to be routed optically. As wavelength is the common granularity in WDM systems, it is straightforward to label the signal with a wavelength and route through different nodes in the network. Figure 2.1 shows a WDM network with a ring topology. This architecture comes

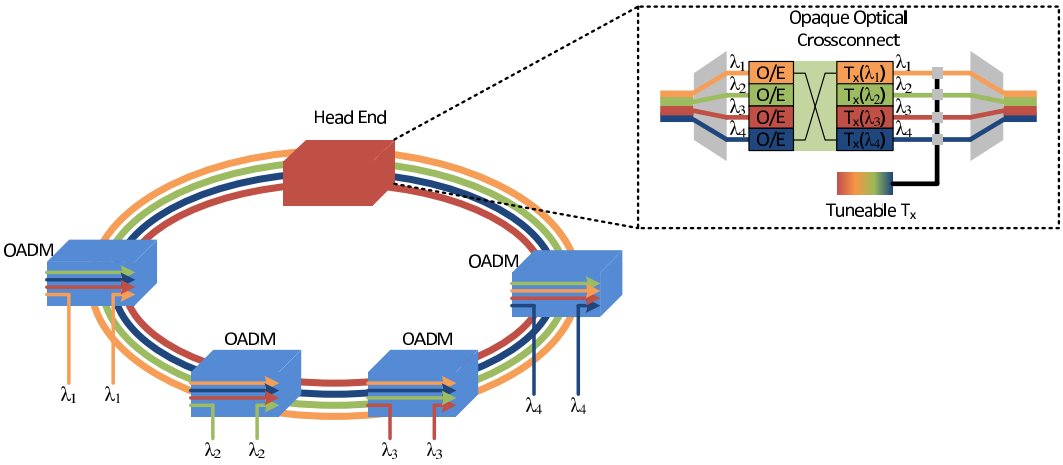

Figure 2.1: A ring topology with OADMs and a head end. A tunable transmitter is used to spare the fixed wavelength transmitters at the egress of the head end.

in many flavours, one of which is that the delay of the OEO conversion at each node of the network has been mitigated by employing a passive optical add-drop multiplexer (OADM). The routing and switching is accomplished in the head end only, which significantly reduces the complexity of the management of the whole network. As shown in Figure 2.1, the data labelled with λ_1 is transported to the head end where the label is swapped from λ_1 to λ_4 (see the black lines in the cross-connect). The signal with the new label will then be dropped at a different node. The number of wavelengths in the network is decided by the number of the ring nodes, which could be expanded up to N$\times$32 (N per OADM node) [6]. It is very expensive to keep a spare card for each and every wavelength. As shown in the inset of Figure 2.1, a single wavelength tunable laser can be used to spare all the transmitter in the head end, and it can also be used as a spare transponder card that is initially set to the node wavelength and left there statically [4].

2.1.2 Reconfigurable Networks

Although the architecture above brings great benefits to the network with high macro-level traffic demands, it results in slow service response times, high start-up costs and low capacity utilization due to its relatively fixed and static nature. The architecture cannot satisfy the micro-level bandwidth demand changes because once a new wavelength is added, the

bandwidth is constantly occupied and cannot be released unless the node is removed from the ring. These types of networks are often categorized as 'static' networks. In order to alleviate the cost and complexity of managing the micro and macro-level demand changes, new tunable technologies must be leveraged, integrated and deployed in carrier networks [7].

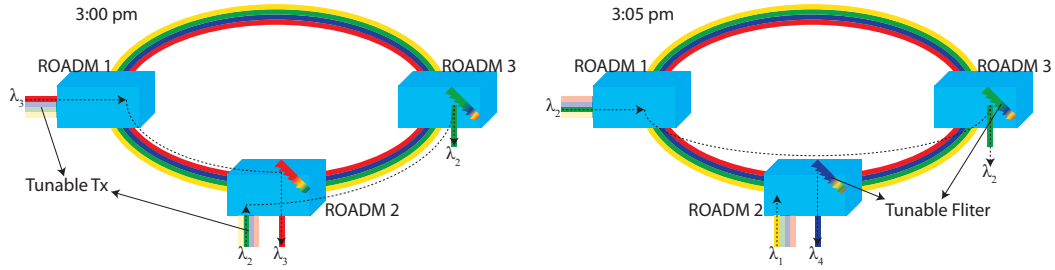

(a) (b)

Figure 2.2: Flexible wavelength provisioning with tunable lasers and filters.

Figure 2.2 shows a reconfigurable network architecture with fast wavelength provisioning. Instead of using fixed wavelength OADMs, reconfigurable OADMs (ROADMs) with tunable lasers and filters are employed. At the time when the optical path is established as in Figure 2.2a, λ_3 is added from ROADM1 and dropped at ROADM2, while λ_2 is added from ROADM2 and dropped at ROADM3. If the data from ROADM1 is required to be sent to ROADM3 at a different time as shown in Figure 2.2b, this can be achieved by switching the output wavelength of the tunable transmitter (Tx) in ROADM1 to λ_2. Meanwhile the selected wavelength of the tunable filter at ROADM2 can be changed to λ_4 to receive the data from a different node. Thus the reconfigurable network allows automated provisioning and simplifies sparing as only a universal tunable line card is necessary, which is a vital component in this type of 'dynamic' network as opposed to the 'static' networks with fixed wavelength line card.

2.1.3 Optical Burst Switching and Optical Packet Switching

The networks discussed in the previous two subsections belong to the class of optical circuit switching networks in which source-to-destination optical paths are set up ahead of time and these paths are maintained for relatively long periods of operation (semipermanent) [4]. In order to improve the utilization of optical network resources and reduce the latency of the

data, switching of optical data at the granularities of packets and bursts are being developed, such as optical burst switching (OBS) and optical packet switching (OPS) [8].

The data traffic is already dominant in today's networks with Internet Protocol (IP)-based packetized services, which are encoded into small packets or frames [5]. Inside each packet there is a header which contains the information for electronic routing and a payload which contains the actual data. For OBS networks, the packets are aggregated into bursts at the edge of the core network. A control signal is sent ahead of the burst in order to build up an optical path. The bursts are then converted to optical form, and routed through the entire core network in the optical domain. The optical path will not be released until a positive acknowledgement has been received at the input node (ingress).

To further increase the network efficiency and increase the capacity of the Internet router, individual data packets can be forwarded through the network directly in the optical layer referred to as OPS [9]. Ideally, OPS is performed all optically. However, due to the numerous technological limitations, the research community has been investigating different forms of OPS where the control signal is carried out by electronics. All-optical label swapping (AOLS) is one of the OPS schemes where the optical label is erased and rewritten at each optical packet switch while the IP payload is kept intact through the optical networks [10].

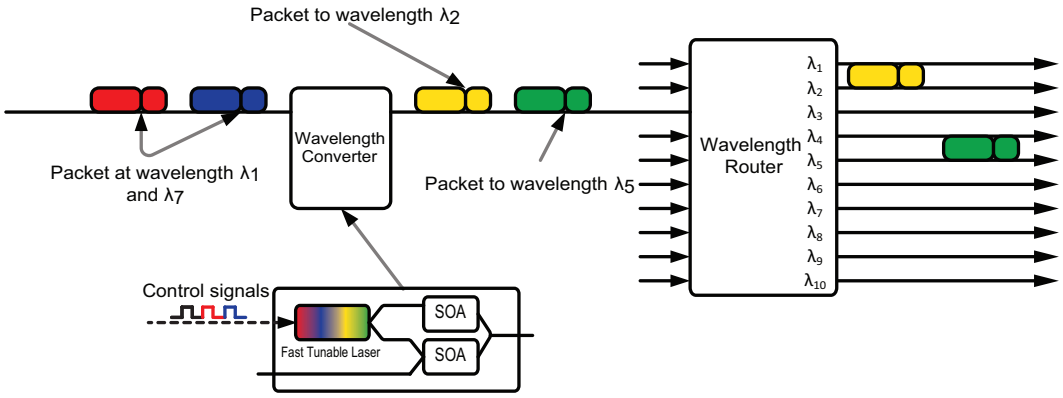

Figure 2.3: A OPS forwarding module based on a fast tunable wavelength converter and wavelength router to realized fast packet switching. (adapted from [10])

Figure 2.3 displays a simple example of how this technique would be used for forwarding individual packets. A small percentage of the light is tapped at the input of the module,

and the optical label is recovered by the receiver. The control signal is then generated and used to switch the fast tunable laser in the wavelength converter. The data packets are subsequently directed spatially to a different port of the arrayed router. The electronic-switching and power-dissipation bottlenecks can be overcome without passing the high speed payload through OEO conversion. The AOLS critically depends on the switching speed of the tunable laser used as the local source for new wavelengths [11]. There is a wide variety of tunable laser designs which enable fast (on the order of several nanoseconds) switching between the international telecommunication union (ITU) grid lasing modes over a broad range of wavelength. A detailed description of the structure and functionality of the tunable lasers will be given in the following chapter.

2.2 Advanced Modulation Formats

In the previous section we have seen that today's optical networks employ WDM channels to propagate and route data without OEO conversion. However, the bandwidth demand continues to increase exponentially due to the rapid growth of video-based Internet applications. 100G router ports and 100G optical transport interfaces are commercially available and the heavy data-centric users are starting to ask for 400G as well as 1T interfaces for the next possible standard [12]. Coarse WDM (CWDM) systems provide only 8 channels in the conventional fibre transmission window (C band) [13], while a typical dense WDM (DWDM) systems would use 40 channels at 100 GHz spacing or 80 channels with 50 GHz spacing in the C band [14]. The channel spacing should also allow for a frequency deviation of $\pm$ 20% of the channel separation caused by the frequency drift of the laser [15]. Thus, the available bandwidth on each optical carrier is less than 60% of the corresponding channel spacing. In addition, optical multiplexers which are widely used in ROADMs and wavelength routers acts as an optical bandpass filter (OBPF) to select channels [16]. Therefore, the bandwidth of the data again will be severely limited by the bandwidth of the OBPF especially after propagating through a series of the OBPFs. Spectrally efficient modulation formats are becoming increasingly important to maximise the data rate that can

be transmitted in the available bandwidth. In addition, the modulation formats with high SE offer higher signal tolerance to transmission impairments such as optical noise, chromatic dispersion (CD) and polarization-mode dispersion (PMD) [17]. In this section, some of the commonly used advanced modulation formats and the corresponding generation and detection method will be briefly described.

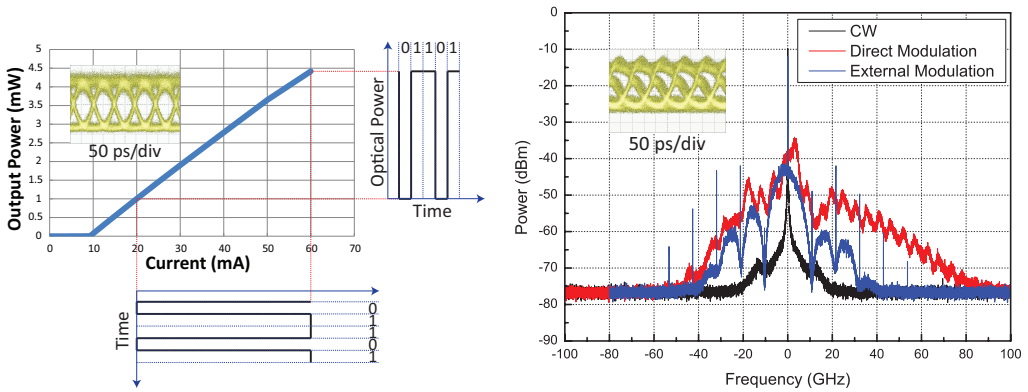

Figure 2.4: (a) Direct modulation of a laser. The inset shows the optical eye diagram of a 10.7 Gb/s OOK signal. (b) Optical spectra of the directly and externally modulated signal. The inset shows the eye diagram of the same OOK signal after propagating through 50 km of fibre.

2.2.1 Direct Modulation

Since the output power and the bias current of the laser exhibit a linear relationship above threshold (see Figure 2.4a), the intensity of the light can be easily modulated by directly driving the laser with the electrical bit stream. Figure 2.4b shows the optical spectra of a 10.7 Gb/s on-off keying (OOK) signal with direct and external modulation respectively. Although the eye in Figure 2.4a is clean and open, the optical spectrum of the direct modulated signal is broader than that generated by an external modulator. This broadening is due to the significant wavelength chirp (frequency deviation) [18] related to the desired intensity modulation by

$$\Delta\nu = -\frac{\alpha}{4\pi}\left[\frac{1}{P_0}\frac{dP}{dt} + \frac{\epsilon}{\tau_P}\Delta P\left(t\right)\right], \tag{2.1}$$

where α is the phase-amplitude coupling constant, P_0 represents the steady-state photon density, ϵ is the gain suppression ratio and τ_P denotes the photon lifetime. The contribution involving dP/dt is called the transient chirp, while the term which is proportional to $\Delta P(t)$ is called the adiabatic chirp [19]. The broad spectral width exacerbates the pulse broadening and intersymbol interference induced by the dispersion of the fibre, which counteracts the simple and low-cost configuration of the direct modulation and limits it to short-reach applications [20].

2.2.2 External Modulation with MZMs

Different methods have been developed to reduce the chirp inherent with the direct modulation to increase the reach and data rate of transmission systems [21, 22]. An external modulation technique is considered to be an alternative candidate in order to eliminate this problem [23]. Any electro-optic crystals with proper orientation can be used for phase modulation, where a LiN_bO_3 waveguide is commonly used in practice [3]. When only the Pockels effect is considered, the phase shift $\varphi_{PM}(t)$ of the phase modulator can be assumed to be linear to the applied external voltage $u(t)$ by the relation

$$\varphi(t) = \frac{2\pi}{\lambda} \cdot \Delta n_{eff}(t) \cdot l_m \sim u(t), \tag{2.2}$$

where l_m is the length of the modulator and $\Delta n_{eff}(t)$ is the change of the effective refractive index. By utilizing the principle of interference, both the amplitude and the phase of the incident light can be modulated respectively.

Figure 2.5a shows the structure of an in-phase and quadrature (IQ) modulator formed by two sub-Mach-Zehnder modulators (MZMs) and a phase modulator (PM). Figure 2.5b plots the optical power and field transmission curves of the single MZM, which is operating in push-pull mode by driving the two arms of the MZM with the same amount of voltage but in opposite polarity [5]. In this case a chirp-free amplitude modulation is obtained [5, 23, 24] by biasing the MZM at the quadrature point of the power transmission curve (see the red square in Figure 2.5b). If the MZM is operating at the minimum power transmission point

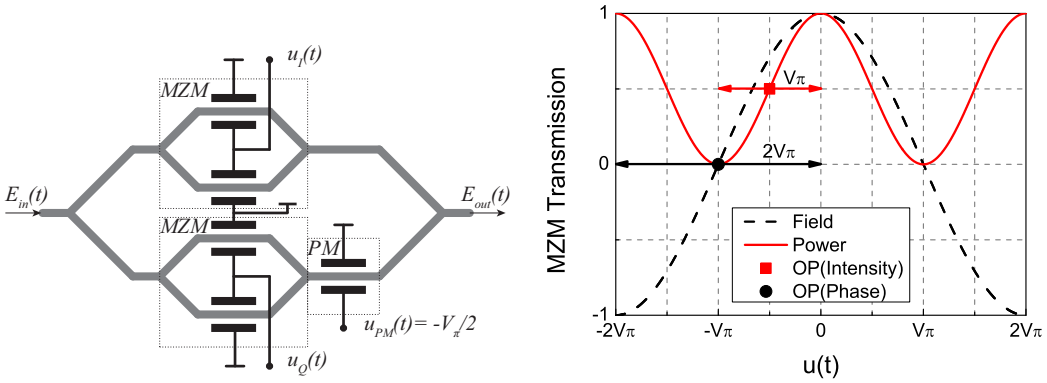

(a) (b)

Figure 2.5: (a) Schematic of an optical IQ modulator with two sub-MZM and a PM. (b) Optical field and power transmission curve for the MZM and the operating point for intensity and phase modulation.

(also referred to as null point), a π phase change occurs each time the drive signal $u(t)$ crosses the minimum point. The optical intensity eye diagram of an OOK and a binary phase shift keying (BPSK) signal generated by biasing a single MZM at the two operating points (null and quadrature), where the amplitude of $u(t)$ equals to V_π and $2V_\pi$ respectively, are shown in Figure 2.5b. The corresponding constellation diagrams of the two signals are also shown in Figure 2.6d and Figure 2.6e, which display the signal as a two-dimensional scatter diagram in the complex plane at symbol sampling instants.

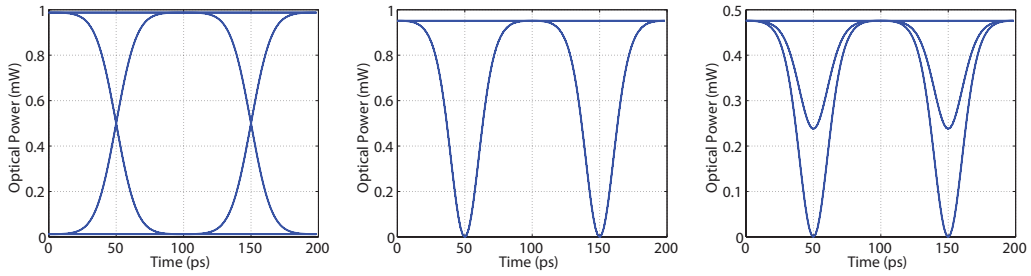

(a) (b) (c)

Figure 2.6: The optical intensity eye diagrams for (a) OOK. (b) BPSK. (c) QPSK. The average input power is 1 mW.

Although the full complex plane of the optical field can be covered by a drive voltage swing of $2V_\pi$ on each arm of the single MZM, it is more convenient to control the two quadratures independently using a true IQ modulator as shown in Figure 2.5a [3, 5]. A

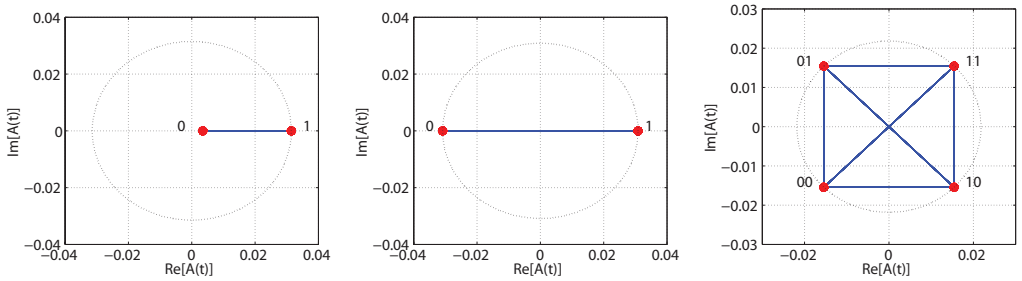

(d) (e) (f)

Figure 2.6: The constellation diagrams for (d) OOK. (e) BPSK. (f) QPSK.

third modulator introduces a $\pi/2$ phase shift, which puts the signal at the output of the two subMZMs at quadrature to each other. Figure 2.6c and Figure 2.6f show the eye and the constellation diagrams of the signal at the output of the IQ modulator, when the two sub-MZMs are driven using the same condition as described earlier for generating BPSK [25]. This signal is called quadrature phase shift keying (QPSK), which transmits the four phase shifts $\{+\pi/4, +3\pi/4, -3\pi/4, -\pi/4\}$ at the same symbol rate as the OOK and BPSK (10.7 Gb/s). Therefore the data rate is doubled while the spectral occupancy is maintained [25], which improves the SE by a factor of two [26]. The SE can be easily doubled again by employing the two orthogonal polarization states as for dual-polarization (DP) QPSK [27] and polarization-division multiplexing (PMD) QPSK [28].

The SE can be significantly improved by driving the two arms of the IQ modulator with multi-level signals such as m-ary quadrature amplitude modulation (QAM) or m-QAM. The SE of an M-level system is improved by a factor of $log_2 M$ when compared to a binary coding system at the same symbol rate. Using multi-carriers with orthogonal frequencies, which requires the sub-carrier spacing to be an integer multiple of the symbol rate, allows sub-carriers to be placed in close proximity, further increasing SE. This can be achieved by either optically multiplexing, as in coherent wavelength division multiplexing (CoWDM) [29], or electronically multiplexing, as in orthogonal frequency division multiplexing (OFDM) [30], which has gained enormous interest in the research of high-capacity optical communication systems [31].

2.2.3 Self-coherent and Coherent Detection

The photodiodes which are widely used in the OOK systems employing an intensity modulation/direct detection (IMDD) scheme are only sensitive to the intensity of the optical signal. In order to recover the phase information within the advanced modulation formats, a phase reference, which might be provided by either an optical local oscillator (LO) or a delayed replica of the signal itself, is required. These two methods that are used to convert the phase modulation into intensity modulation that can be directly detected by square-law detectors, are regarded as coherent detection and self-coherent or differentially coherent detection respectively [5]. For a BPSK signal, a one bit Mach-Zehnder delay interferometer (MZDI) can be used for self-coherent detection, which is just a simple Mach-Zehnder interferometer (MZI) where the signal is delayed by approximately one symbol period (T_S) between the the two arms of the MZDI [26] (see Figure 2.7). Precoding is required as for only the phase difference between two adjacent bits is converted to intensity modulation [32] and this type of BPSK signal is called differential binary phase shift keying (DPSK). Balanced detectors are usually used for DPSK signals to take advantage of a 3 dB receiver sensitivity offered by DPSK over OOK. Analogous to the DPSK direct detection, two orthogonal MZDIs are usually used to demodulate the in-phase (I) and quadrature (Q) component of the differential quadrature phase shift keying (DQPSK) signal. The differential optical phase between interferometer arms (φ_{DL}) is set to $\pi/4$ and $-\pi/4$ for upper and lower branches respectively [33].

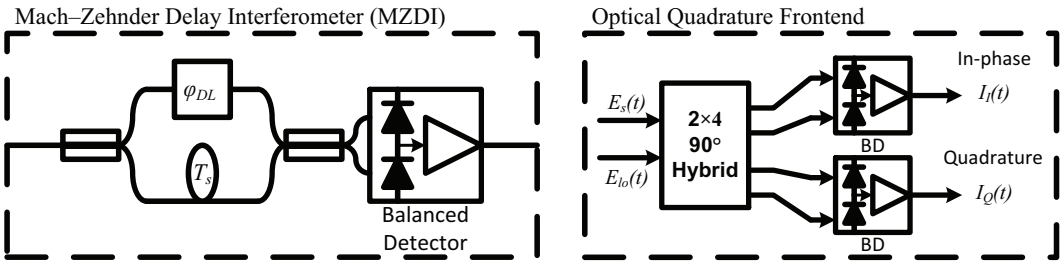

Figure 2.7: Structure of a delayed interferometer and an optical quadrature front end for self-coherent and coherent detection

The fundamental concept behind coherent detection is to take the product of the electric

field of the modulated signal light and the continuous wave (CW) LO. Figure 2.7 also shows the structure of an optical quadrature front end composed of a 90° optical hybrid. In the hybrid, the LO is split into two branches and a 90° phase shift is introduced to one of the branches in order to detect both the in-phase and quadrature components of the signal [5]. Therefore, the full constellation of the modulated signal with advanced modulation formats can be recovered.

2.2.4 Signal Degradations

There are various design parameters for both the transmitter and the receiver which will affect the detected coherent signal. The self-coherent detection is sensitive to various design parameters of the balanced differential receiver such as the detector amplitude and phase imbalance, interferometer delay mismatch, interferometer extinction and laser frequency offset [25]. The most critical impairment in a practical receiver is found to be a mismatch between the laser frequency and the interferometer phase, which directly impacts the interference quality [34]. A frequency offset of 2% of the bit rate of a DPSK system will cause an optical signal-to-noise ratio (OSNR) penalty of approximately 1 dB [34]. Figure 2.8 shows the distorted eye diagrams of a DQPSK system with a frequency offset of 2% of the bit rate (see Figure 2.8b). It has been proven that DQPSK is approximately six times more sensitive to this impairment than binary DPSK [35]. However this frequency offset is less sensitive for coherent detection as digital signal processing (DSP) can be used to compensate the offset.

Another important noise impairment which has an impact on both the self-coherent and coherent detection for advanced modulation formats is the laser phase noise. In self-coherent detection, the phase modulated signal is converted into intensity modulation by using a delayed version of the signal itself as a phase reference, while in coherent detection the reference is an optical LO. The laser phase noise is measured by the laser linewidth which is defined as the full-width half-maximum (FWHM) bandwidth ($\Delta\nu$) of the laser power spectral density (PSD) [36]. The coherence time of the laser (τ_c) is defined as the

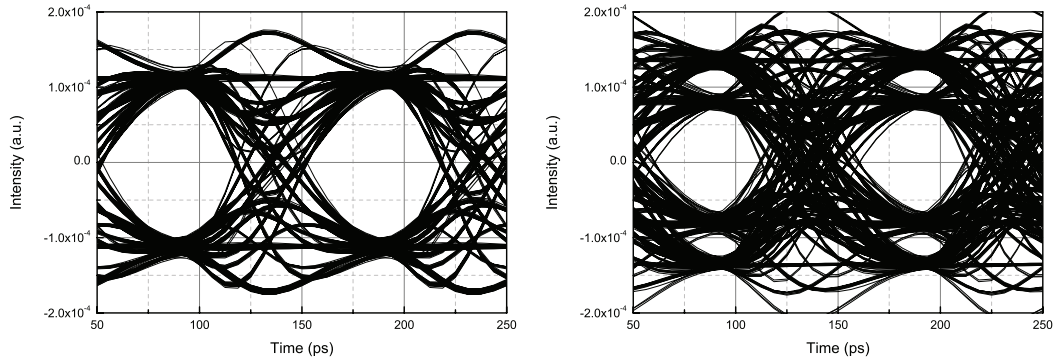

Figure 2.8: Eye diagram for DQPSK system for a laser frequency offset Δf equals to (a) 0 and (b) 2% of the bit rate.

time interval in which the phase of laser is predictable, is related to the laser linewidth as

$$\tau_c = \frac{1}{\pi \Delta \nu}. \tag{2.3}$$

Random phase changes cause an uncertainty in the phase relation between a time interval longer than τ_c, which will consequently introduce errors in phase modulated formats [37]. The lower the baud rate the longer the coherence time is required in order to achieve error free transmission, which can be seen in the constellation diagrams in Figure 2.9. The same amount of circularly spread constellation points are demonstrated for a 1.25G baud and a 10G baud DQPSK systems, where the linewidth of the laser in the 1.25G baud system is ten times smaller. For DPSK, the $\Delta \nu Ts$ is required to be less than 1% to operate with a $<$1 dB penalty at the bit error rate (BER) equal to 10^{-4} [24]. This requirement becomes more stringent for DQPSK systems, where a $\Delta \nu Ts$ value of less than 0.05% may be needed [24, 38]. For higher order modulation formats this requirement will be even higher (see Figure 2.9c), which is due to the decreased distance between adjacent constellation points. The linewidth requirement is more stringent for coherent detection compared to self-coherent detection, where the linewidth of both the signal and the LO should be remain relatively low (10% of the linewidth required for self-coherent detection) to avoid sensitivity degradation [39].

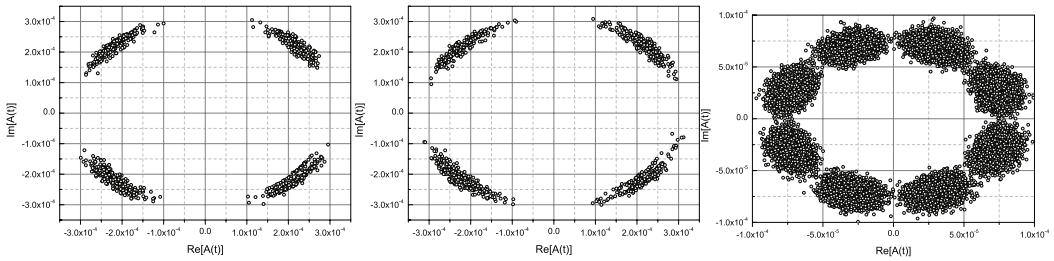

(a) (b) (c)

Figure 2.9: The constellation diagrams for (a) 1.25G baud DQPSK with $\Delta\nu$=5MHz. (b) 10 Gbaud DQPSK with $\Delta\nu$=50MHz. (c) 10 Gbaud D8PSK with $\Delta\nu$=50MHz.

2.3 Summary

Optical networks are experiencing a shift towards greater reconfigurability with the deployment of ROADM and optical cross-connects in order to increase the switching efficiency and reduce the network latency. Another key component in these reconfigurable optical networks is the wavelength tunable laser. Initially deployed for sparing and inventory management in WDM networks, tunable lasers also enable functionality such as dynamic bandwidth provisioning, protection, restoration, OBS and OPS. Depending on the function, the required switching time can range form seconds to nanoseconds.

Another growing trend in optical networks is towards the use of advanced optical modulation formats that offer improved SE and increased tolerance to fibre transmission effects, while using the phase of the optical carrier as well as its intensity to carry the information. The move towards advanced modulation formats means that the linewidth of the laser, which is related to the phase noise, is becoming increasingly important for both coherent and self-coherent detection schemes. In order to use wavelength tunable lasers in future high speed reconfigurable optical networks employing advanced modulation formats, the linewidth of the laser needs to be characterized as well as the impacts it has on the system performance.

References

[1] G. Keiser, *Optical Fiber Communications*, 4th ed. New York: Mc-Graw Hill, 2010.

[2] G. Agrawal, *Long-wavelength semiconductor lasers*. New York: Van Nostrand Reinhold, 1986.

[3] ——, *Fiber-optic communication systems*, 4th ed. Hoboken N.J.: Wiley, 2010.

[4] J. Buus, M. Amann, and D. J. Blumenthal, *Tunable Laser Diodes and Related Optical Sources*, 2nd ed. Wiley-IEEE Press, Feb. 2005.

[5] I. P. Kaminow, T. Li, and A. E. Willner, *Optical Fiber Telecommunications V B, Fifth Edition: Systems and Networks*, 5th ed. Academic Press, Feb. 2008.

[6] S. Kartalopoulos, *DWDM : networks, science, and technology*. New York ;;Chichester: Wiley, 2002.

[7] T. Day, C. B. Thompson, and J. Lee, "Widely tunable laser technologies: meeting the needs of tomorrow's networks," in *Proceedings of SPIE*, vol. 4652, San Jose, CA, USA, 2002, pp. 186–196.

[8] T. El-Bawab, *Optical switching*. New York NY: Springer, 2006.

[9] D. Blementhal, T. Ikegami, P. Prucnal, and L. Thylen, "Guest editorial photonic packet switching technologies, techniques, and systems," *Journal of Lightwave Technology*, vol. 16, pp. 2065–2067, Dec. 1998.

[10] D. J. Blumenthal, "Photonic packet switching and optical label swapping," *Optical Networks Magazine*, vol. 2, no. 6, p. 54, Nov. 2001.

[11] D. Blumenthal, B. Olsson, G. Rossi, T. Dimmick, L. Rau, M. Masanovic, O. Lavrova, R. Doshi, O. Jerphagnon, J. Bowers, V. Kaman, L. Coldren, and J. Barton, "All-optical label swapping networks and technologies," *Journal of Lightwave Technology*, vol. 18, no. 12, pp. 2058–2075, Dec. 2000.

[12] P. Winzer, "Beyond 100G ethernet," *IEEE Communications Magazine*, vol. 48, no. 7, pp. 26–30, Jul. 2010.

[13] *Spectral grids for WDM applications: CWDM wavelength grid*, The International Telecommunication Union (ITU) Std. ITU-T G.694.2, 12 2003. [Online]. Available: http://www.itu.int/rec/T-REC-G.694.2-200312-I/en

[14] *Spectral grids for WDM applications: DWDM frequency grid*, The International Telecommunication Union (ITU) Std. G.694.1, 06 2002. [Online]. Available: http://www.itu.int/rec/T-REC-G.694.1/en

[15] *Transmission media characteristics:Characteristics of optical components and sub-systems*, The International Telecommunication Union (ITU) Std. ITU-T G.692, 10 1998. [Online]. Available: http://www.itu.int/rec/T-REC-G.692/en

[16] P. J. Winzer and R. J. Essiambre, "Advanced modulation formats for High-Capacity optical transport networks," *Journal of Lightwave Technology*, vol. 24, no. 12, pp. 4711–4728, Dec. 2006.

[17] X. Liu and S. Chandrasekhar, "Advanced modulation formats for core networks," in *OptoeElectronics and Communications Conference (OECC), 2011 16th*. IEEE, Jul. 2011, pp. 399–400.

[18] R. S. Vodhanel, A. F. Elrefaie, M. Z. Iqbal, R. E. Wagner, J. L. Gimlett, and S. Tsuji, "Performance of directly modulated DFB lasers in 10-Gb/s ASK, FSK, and DPSK lightwave systems," *Journal of Lightwave Technology*, vol. 8, no. 9, pp. 1379–1386, Sep. 1990.

[19] A. Yariv, *Optical electronics in modern communications*, 5th ed. New York: Oxford University Press, 1997.

[20] K. Sato, S. Kuwahara, and Y. Miyamoto, "Chirp characteristics of 40-gb/s directly modulated distributed-feedback laser diodes," *Journal of Lightwave Technology*, vol. 23, no. 11, pp. 3790– 3797, Nov. 2005.

[21] S. Mohrdiek, H. Burkhard, and H. Walter, "Chirp reduction of directly modulated semiconductor lasers at 10 gb/s by strong CW light injection," *Journal of Lightwave Technology*, vol. 12, no. 3, pp. 418–424, Mar. 1994.

[22] D. Mahgerefteh, Y. Matsui, X. Zheng, and K. McCallion, "Chirp managed laser and applications," *IEEE Journal of Selected Topics in Quantum Electronics*, vol. 16, no. 5, pp. 1126–1139, Oct. 2010.

[23] F. Koyama and K. Iga, "Frequency chirping in external modulators," *Journal of Lightwave Technology*, vol. 6, no. 1, pp. 87–93, Jan. 1988.

[24] M. Seimetz, *High-order modulation for optical fiber transmission*. Dordrecht, New York: Springer, 2009.

[25] A. H. Gnauck and P. J. Winzer, "Optical phase-shift-keyed transmission," *Journal of Lightwave Technology*, vol. 23, no. 1, pp. 115– 130, Jan. 2005.

[26] C. Xu, X. Liu, and X. Wei, "Differential phase-shift keying for high spectral efficiency optical transmissions," *IEEE Journal of Selected Topics in Quantum Electronics*, vol. 10, no. 2, pp. 281– 293, Apr. 2004.

[27] K. Roberts, M. O'Sullivan, K. Wu, H. Sun, A. Awadalla, D. J. Krause, and C. Laperle, "Performance of Dual-Polarization QPSK for optical transport systems," *Journal of Lightwave Technology*, vol. 27, no. 16, pp. 3546–3559, Aug. 2009.

[28] A. H. Gnauck, P. J. Winzer, G. Raybon, M. Schnecker, and P. J. Pupalaikis, "10 224-Gb/s WDM transmission of 56-Gbaud PDM-QPSK signals over 1890 km of fiber," *IEEE Photonics Technology Letters*, vol. 22, no. 13, pp. 954–956, Jul. 2010.

[29] A. D. Ellis, F. C. Gunning, B. Cuenot, T. C. Healy, and E. Pincemin, "Towards 1TbE using coherent WDM," in *Opto-Electronics and Communications Conference, 2008 and the 2008 Australian Conference on Optical Fibre Technology. OECC/ACOFT 2008. Joint conference of the*. IEEE, Jul. 2008, pp. 1–4.

[30] W. Shieh, H. Bao, and Y. Tang, "Coherent optical OFDM: theory and design," *Optics Express*, vol. 16, no. 2, pp. 841–859, Jan. 2008.

[31] L. Yan, X. Liu, and W. Shieh, "Toward the shannon limit of spectral efficiency," *IEEE Photonics Journal*, vol. 3, no. 2, pp. 325–330, Apr. 2011.

[32] D. Penninckx, H. Bissessur, P. Brindel, E. Gohin, and F. Bakhti, "Optical differential phase shift keying (DPSK) direct detection considered as a duobinary signal," in *27th European Conference on Optical Communication, 2001. ECOC '01*, vol. 3. IEEE, 2001, pp. 456– 457 vol.3.

[33] R. A. Griffin and A. C. Carter, "Optical differential quadrature phase-shift key (oDQPSK) for high capacity optical transmission," in *Optical Fiber Communication Conference and Exhibit, 2002. OFC 2002*. IEEE, Mar. 2002, pp. 367– 368.

[34] P. J. Winzer and H. Kim, "Degradations in balanced DPSK receivers," *IEEE Photonics Technology Letters*, vol. 15, no. 9, pp. 1282–1284, Sep. 2003.

[35] G. Bosco and P. Poggiolini, "On the joint effect of receiver impairments on direct-detection DQPSK systems," *Journal of Lightwave Technology*, vol. 24, no. 3, pp. 1323–1333, Mar. 2006.

[36] K. Petermann, *Laser diode modulation and noise*. Dordrecht ;;Boston ;Tokyo ;Norwell MA: Kluwer Academic Publishers ;;KTK Scientific Publishers ;;Sold and distributed in the U.S.A. and Canada by Kluwer Academic Publishers, 1991.

[37] D. Derickson, *Fiber optic test and measurement*. Upper Saddle River N.J.: Prentice Hall PTR, 1998.

[38] S. Savory and A. Hadjifotiou, "Laser linewidth requirements for optical DQPSK systems," *IEEE Photonics Technology Letters*, vol. 16, no. 3, pp. 930–932, Mar. 2004.

[39] Y. Atzmon and M. Nazarathy, "Laser phase noise in coherent and differential optical transmission revisited in the polar domain," *Journal of Lightwave Technology*, vol. 27, no. 1, pp. 19–29, Jan. 2009.

Chapter 3

Tunable Semiconductor Lasers

As previously discussed, fast switching widely tunable semiconductor lasers will be a key component in future agile reconfigurable networks. When semiconductor lasers were first developed in the 1970s, the lasing was multi-moded because the two cleaved Fabry-Pérot (FP) facets were not wavelength selective. The broad output spectrum of the laser caused a severe reduction of the transmission distance due to the fiber dispersion and also the multi-mode semiconductor lasers can clearly not be used in wavelength-division multiplexing (WDM) systems. Therefore, it is necessary to design single-mode semiconductor lasers with a high side-mode suppression ratio (SMSR). By integrating a Bragg grating inside the laser along either the longitudinal or the transverse direction of the waveguide, single-mode lasing is achieved as a result of the diffraction from the Bragg grating. Since the reflected wavelength of the Bragg grating is related to the order of diffraction and the period of the grating, the lasing wavelength can be tuned by varying different parameters.

In this chapter, some fundamentals of tunable semiconductor lasers will be shown, followed by some examples of the commercially available devices. Then some fast switching widely tunable semiconductor lasers and their switching dynamics will be introduced, which are essential for using the tunable lasers in systems requiring short switching time.

3.1 Fundamental Concepts of Tunable Semiconductor Lasers

Most tunable semiconductor lasers are still based on a FP cavity, with the FP cavity modes selected by the Bragg grating. The refractive index of the Bragg grating is controlled by the tuning current and temperature which decides the reflected peak wavelength. Thus, it is important to understand the fundamental concepts of the basic elements and schemes used in designing tunable semiconductor lasers.

3.1.1 The Fabry-Pérot Laser

The laser structure described here is simplified as a one-dimensional model by using the effective refractive index (n_{eff}) and optical confinement factor Γ [1, 2]. The effective gain in the active layer of the laser is then given by:

$$g_{\text{eff}} \approx \Gamma g_{\text{a}}, \tag{3.1}$$

where the wavelength dependent gain is approximated as a parabola around the peak angular frequency ω_p according to [3]:

$$g_a(\omega, N) = g_N(N - N_0) - g_\omega(\omega - \omega_p(N))^2. \tag{3.2}$$

Here, g_N is the gain coefficient and g_ω is the gain curvature. The transparent carrier density N_0 represents the carrier density N in the active layer that satisfies the Bernard-Duraffourg condition at:

$$E_{F_C} - E_{F_V} = eV_J = h\nu, \tag{3.3}$$

where V_J represents the voltage applied to the laser junction, given from the separation in quasi-Fermi levels (E_{F_C} and E_{F_V}) [4] and e is the elementary charge. The propagating constant β in the cavity including the internal gain and loss is:

$$\beta = k_0 n_{\text{eff}}^{'} + j\frac{g_{\text{eff}} - \alpha_i}{2} \tag{3.4}$$

where α_i is the internal optical loss in the waveguide and $n_{\text{eff}}^{'}$ is the real part of the refractive index. The feedback of the FP laser is provided by the reflection from the two cleaved facets with amplitude reflectivities of r_1 and r_2 respectively. Under the steady-state oscillation condition [2, 5], the optical field is required to reproduce itself after each round trip, which is expressed as:

$$r_1 r_2 e^{-2j\beta L} = 1, \tag{3.5}$$

where L represents the length of the cavity. The imaginary part of equation (3.5) leads to a resonance condition for the cavity, defining a set of longitudinal modes as:

$$m\lambda_N = 2n_{\text{eff}}^{'}L, \tag{3.6}$$

where m is an integer which is the longitudinal mode number. The typical mode spacing of a FP laser with a length of 400 μm is around 0.3–1 nm. The gain curve of the active medium of the laser, described by equation (3.2), can normally support a few tens of longitudinal modes to be lasing simultaneously. A multi-mode rate equation is used to describe the dynamics of photon and electron populations in the FP cavity according to:

$$\frac{dP_m(t)}{dt} = v_g \left(\frac{g\left(\omega_m, N\right)}{\left(1 + \varepsilon \dfrac{P\left(t\right)}{V}\right)} - \alpha_m\left(N\right) \right) \cdot P_m\left(t\right) + R_{sp}\left(\omega_m, N\right) \tag{3.7}$$

$$\frac{dN(t)}{dt} = \frac{I}{eV} - R(N) - v_g \sum_m \frac{g\left(\omega_m, N\right)}{\left(1 + \varepsilon \dfrac{P\left(t\right)}{V}\right)} \cdot \frac{P_m\left(t\right)}{V} \tag{3.8}$$

where $P_m(t)$ is the photon number of the mth longitudinal modes for which the gain $g(\omega_{\text{m}}, N)$ is positive [5], $P(t) = \sum_m P_m(t)$ is the total photon number, v_g is the group velocity, and V is the volume of the active section. $R(N)$ represents the spontaneous re-

combination rate per unit volume and $R_{sp} = n_{sp} v_g g(\omega_m, N)$ represents the spontaneous emission contribution, where n_{sp} is the spontaneous emission coefficient. In a FP laser, the mode loss α_{m} in equation (3.7), which equals the sum of the internal loss α_i and the mirror loss α_{mi}, is wavelength independent. Therefore, a mode-selection filter is necessary for achieving single-mode lasing.

3.1.2 Bragg Grating

The Bragg grating integrated in the laser waveguide, in order to select a single mode, has a refractive index which varies with a period of Λ (see Figure 3.1). Using the Huygen's construction for constructive interference from 'identical' points but at different periods of the grating, one requires that the phase change in a subsection is $\beta\Lambda = \pi$ [4]. Here only the first-order diffraction of a first-order Bragg grating is considered for simplicity. The optimum free-space wavelength λ_B which is most strongly reflected is called the Bragg wavelength and satisfies the Bragg condition:

$$\Lambda = \frac{\lambda_B}{2n_{\mathrm{eff}}} \tag{3.9}$$

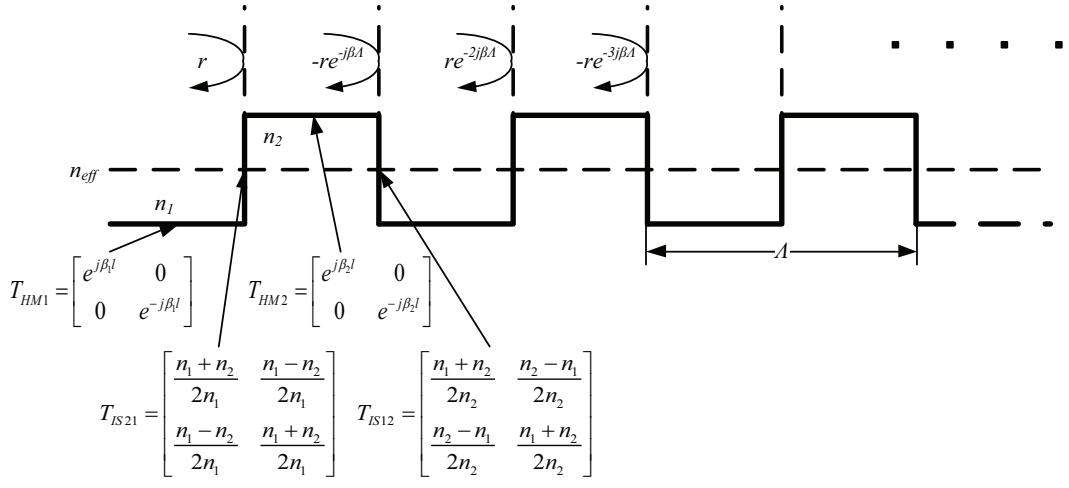

Figure 3.1: Propagation and reflection in a "square" grating. (Adapted from [2]). The matrices describe the two elementary parts of the refractive index step and the homogeneous waveguide.

As the grating structure is periodic, it can be divided into two types of elementary parts

which are a homogeneous waveguide and a refractive index step. Each of the elementary parts can then be described by a 2-by-2 complex transfer matrix which represents the relationship between the forward and backward propagating waves (see the matrices in Figure 3.1) [6]. Figure 3.2a shows the simulated power reflective spectrum of a distributed Bragg reflector (DBR) using the transfer matrix method (TMM). We can see that the width between the first two null points is approximately 1.4 nm, using $\Delta \mathrm{n} = \mathrm{n}_2 - \mathrm{n}_1 = 0.0012$ and the length of the grating $\mathrm{L} = 500\mu\mathrm{m}$. Therefore two side-modes with a spacing of $> 0.7\ \mathrm{nm}$ on each side of the main mode can be fully suppressed by employing the DBR as a mode-selection filter instead of a cleaved facet. A laser with a structure that incorporates an active region and a passive DBR is referred as to DBR laser [7]. In addition, the active region, which provides the gain, and the grating, which provides wavelength selectivity, can be combined together to simplify the fabrication. This type of laser is called the distributed-feedback (DFB) laser [5]. Both types of laser allow SMSRs to be greater than 30 dB.

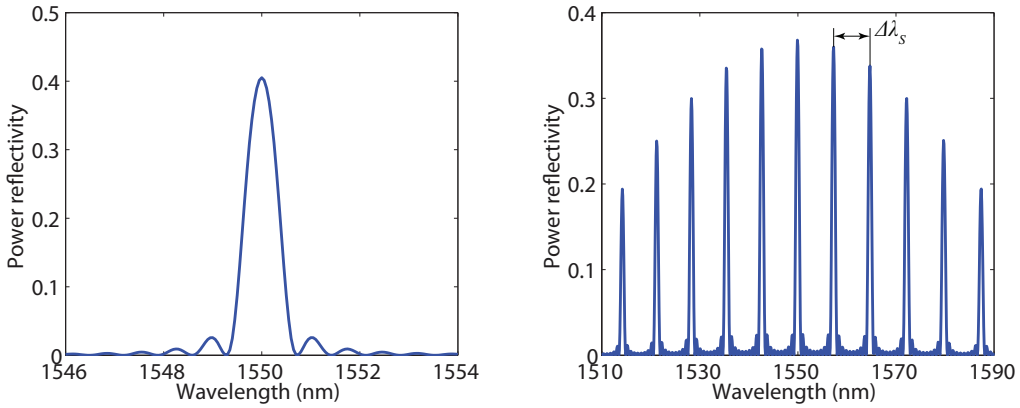

Figure 3.2: Power reflectivity of (a) a DBR and (b) an SG-DBR.

By multiplying the Bragg grating with a periodic sampling function, a comb-like reflective spectrum is generated. Each comb line in the reflective spectrum is considered to have been obtained by convolving the reflective spectrum of a uniform Bragg grating with the comb of the Fourier components in the sampling function [8]. Figure 3.2b displays the power reflective spectrum of an sampled-grating distributed Bragg reflector (SG-DBR) by

using the TMM. The grating burst length (L_g) is equal to 10 % of the length of sampling period (L_s), thus the spacing between the reflective peaks is given by:

$$\Delta\lambda_s = \frac{\lambda^2}{2n_{\text{g,eff}}L_s}, \tag{3.10}$$

where $n'_{\text{g,eff}}$ is the effective group index. The magnitude of the subsidiary reflection peaks depends on the Fourier coefficients of the sampling function. By using a more complicated sampling function, a uniform amplitude of the reflection peaks can be achieved in the superstructure-grating distributed Bragg reflector (SSG-DBR) [9].

3.1.3 Tuning Mechanisms

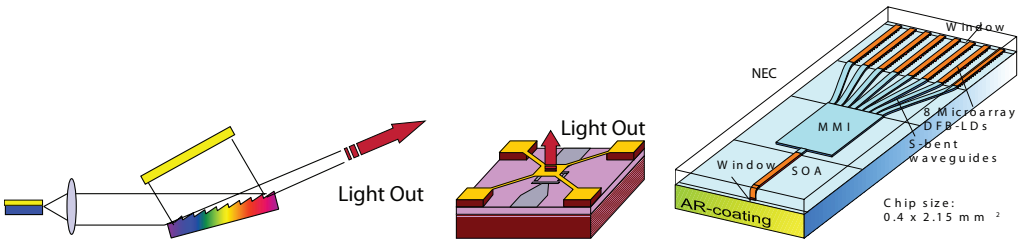

Figure 3.3: Examples of tunable lasers types: (a) ECL, (b) MEMS/VCSEL, (c) selectable DFB array. adapted from [10]

It is indicated in equation (3.6) that the lasing wavelength is related to the longitudinal mode number, the length of the cavity and the effective refractive index. The relative wavelength change derived from equation (3.6) is given in:

$$\frac{\Delta\lambda}{\lambda} = \frac{\Delta n'_{\text{eff}}}{n'_{\text{eff}}} + \frac{\Delta L}{L} - \frac{\Delta m}{m}, \tag{3.11}$$

which shows the relative wavelength change is directly proportional to the relative change in either the length, index or mode number [10]. An external diffraction grating is employed in an external-cavity laser (ECL) in order to select different longitudinal mode numbers by rotating the angle of the grating as illustrated in Figure 3.3a. A micro-electromechanical system (MEMS) is introduced in a wavelength tunable vertical-cavity surface-emitting laser

(VCSEL) to vary the resonator length as indicated in Figure 3.3b, where the fixed epitaxial top mirror of a conventional VCSEL is replaced by a movable mirror membrane [11]. A tuning range of $> 40nm$ has been reported for both the ECL [12] and the VCSEL [11]. Although there are many advantages for these two types of tunable lasers, such as narrow linewidth for the ECL [12] and simpler fiber coupling, easier packaging and the ability to be fabricated in arrays for the VCSEL [13], the wavelength is tuned mechanically which limits the switching time to a few tens of microseconds.

Alternatively, the peak frequency of the gain spectrum ($\omega_p(N)$ in equation (3.2)) as well as the refractive index are both temperature dependent with relationships of 0.5 nm/K and 0.1 nm/K respectively. Thus, it is possible to change the wavelength of all-active single-frequency lasers by varying the temperature of the device. Figure 3.3c shows a wavelength selectable microarray light source consisting of eight-microarray $\lambda/4$ shifted DFB lasers, each of which covers two or three international telecommunication union (ITU) 100 GHz channels using chip-temperature control, from 15 °C to 40 °C [14]. Nevertheless, the switching time of the microarray source is in the scale of microseconds, similar to mechanical tuning, and significantly limits the use of these types of lasers in fast optical switching networks such as optical packet switching (OPS) or optical burst switching (OBS).

In addition to the above, we have seen in equation (3.9) that the Bragg wavelength of a DBR is related to the effective refractive index and therefore the wavelength is readily tunable as the refractive index of a semiconductor can be changed by injecting electron-hole plasma into a semiconductor laser. This also yields an additional optical loss. The relationships between the injected carrier density and the change of the refractive index is given by:

$$\Delta n_{\text{eff}}(N) = \Gamma \frac{dn}{dN} N, \tag{3.12}$$

$$\Delta \alpha_i(N) = \Gamma \frac{d\alpha}{dN} N. \tag{3.13}$$

Γ is the optical confinement factor and dn/dN and $d\alpha/dN$ are material coefficients which describe the free-carrier plasma effect and free-carrier absorption, respectively. The free-carrier plasma effect dominates in the common case of the passive tuning region where the

bandgap energy is significantly larger than the photon energy [2]. The value of dn/dN is normally around $-10^{-26}\mathrm{m}^3$, while the value of $d\alpha/dN$ is usually approximately $10^{21}\mathrm{m}^2$. It is important to notice that dn/dN is negative, which means that when there is an increase in the carrier density in the semiconductor, the refractive index is decreased. The Bragg wavelength is consequently decreased according to equation (3.9). The electronic tuning by injecting current into the passive tuning region can provide much faster switching characteristics than the mechanical tuning schemes due to the short carrier lifetime ($\sim 10^{-8}$ s). Therefore the Bragg wavelength λ_B can be rapidly varied by switching the current of the tuning section.

However, the carrier density in the active region of the laser is clamped above threshold, which can be derived from the stationary solution of equation (3.7) neglecting the spontaneous term R_{sp}. This makes electronic tuning impossible in all-active device such as the DFB laser. Thus, a passive Bragg grating can be integrated longitudinally such as the DBR laser, which allows fast electronic switching [3]. Nevertheless, the tuning range of an electronic tuning semiconductor is limited by the $\Delta\lambda/\Delta\lambda \approx \Delta n'_{\text{neff}}/n'_{\text{neff}}$, which is about 15 nm under normal circumstances. Schemes to extend the tuning range beyond the limit are necessary to cover the full band of the erbium-doped fibre amplifier (EDFA) used in WDM systems, which in principle can be realised by changing the refractive index difference instead of the refractive index itself [2].

3.2 Fast Switching Widely Tunable Lasers

In this section, the Vernier effect of the SG-DBR for extending the tuning range of normal electronic tuning DBR lasers is considered. The fast switching characteristics of the laser are also presented by using simulation results.

3.2.1 The Vernier Effect

From equation (3.10) it is demonstrated that the reflection peak separation of an SG-DBR is inversely proportional to the sampling period L_s. To take advantage of the Vernier effect,

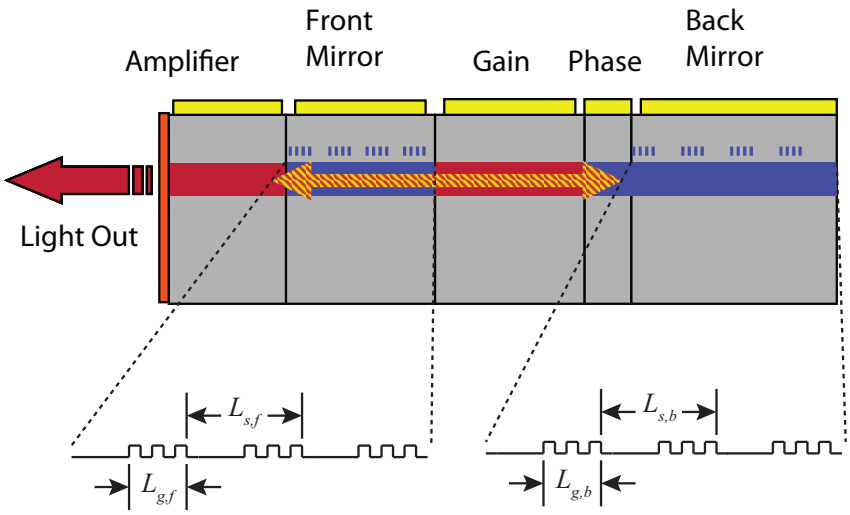

Figure 3.4: Structure diagram of an SG-DBR laser with integrated SOA.

we can fabricate two SG-DBRs at both the front and the back of the laser (see Figure 3.4), with sampling periods $L_{s,f}$ and $L_{s,b}$ being different [2, 8]. Figure 3.5a and Figure 3.5c show the power reflectivity of two SG-DBR with the sampling periods of 58 μm (red line) and 64 μm (blue line) respectively. The corresponding comb spacing is 5.6 nm for the front grating (P_f) and 5.1 nm for the back grating (P_b) according to equation (3.10). The smaller amount of reflectivity from the front grating is due to the fact that there are 10 sampling periods in the front SG-DBR while there are 12 sampling periods in the back SG-DBR, which provides higher feedback. The lasing mode occurs when the maxima of $\mathrm{R_f}$ (front grating) and $\mathrm{R_b}$ (back grating) are aligned, which is approximately 1545 nm for the case of Figure 3.5b.

As previously discussed, when there is an increase in the current on the front grating, the reflective index decreases according to equation (3.12). Therefore, the Bragg wavelength of the front grating is shifted towards low wavelengths based on the relationship described by equation (3.9). As illustrated in Figures 3.5c and 3.5d, the next aligned reflection peak is shifted towards the adjacent peak of the back grating at a wavelength of around 1550 nm (see Figure 3.5d). The actual current change on the front section is only to shift the refractive spectrum by $\Delta P = P_f - P_b$, which gives an aligned wavelength change of P_b due to the Vernier effect. Thus the tuning rate is enhanced by a factor of $F = P_{ave}/\Delta P$

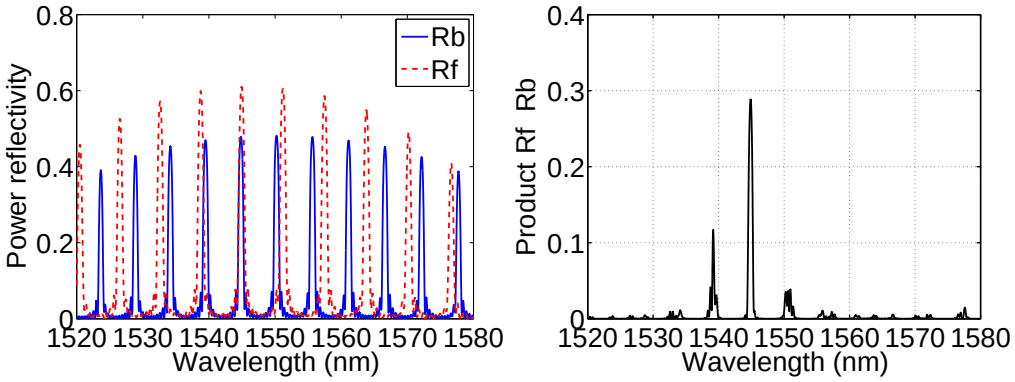

(a) $\mathrm{I_f} = 15\mathrm{mA}$ (b) $\mathrm{I_f} = 15\mathrm{mA}$

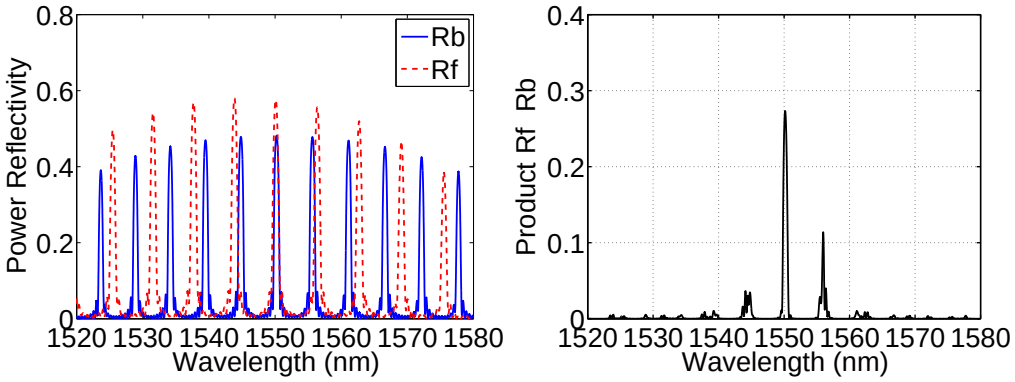

(c) $\mathrm{I_f} = 24\mathrm{mA}$ (d) $\mathrm{I_f} = 24\mathrm{mA}$

Figure 3.5: Power reflectivity of SG-DBRs with two different lengths of sampling period, which are 58 μm (red line) and 64 μm (blue line). Lasing occurs where the maxima of $\mathrm{R_f}$ (front grating) and $\mathrm{R_b}$ (back grating) are aligned. The tuning current on the front grating is 15 mA in (a) and (b), and 24 mA for (c) and (d).

comparing to the conventional $\Delta n'_{\mathrm{neff}}/n'_{\mathrm{neff}}$, where P_{ave} is the average grating spectrum period [8]. The wavelength tuning of the back grating is similar to the mechanism above, but the next aligned peak is shifted towards the adjacent peak at lower wavelength when the current on the back section is increased, which can be observed in Figure 3.6a, where the three-dimensional (3-D) surface of the lasing wavelength is obtained by varying the current on the front and back gratings. The wavelength between the two adjacent reflection peaks in Figures 3.5b and 3.5d is accessed by varying the current on both the front and back grating simultaneously [15]. It should be noted that there is more than one longitudinal mode in the aligned reflection peaks, therefore an additional phase section is integrated as shown in

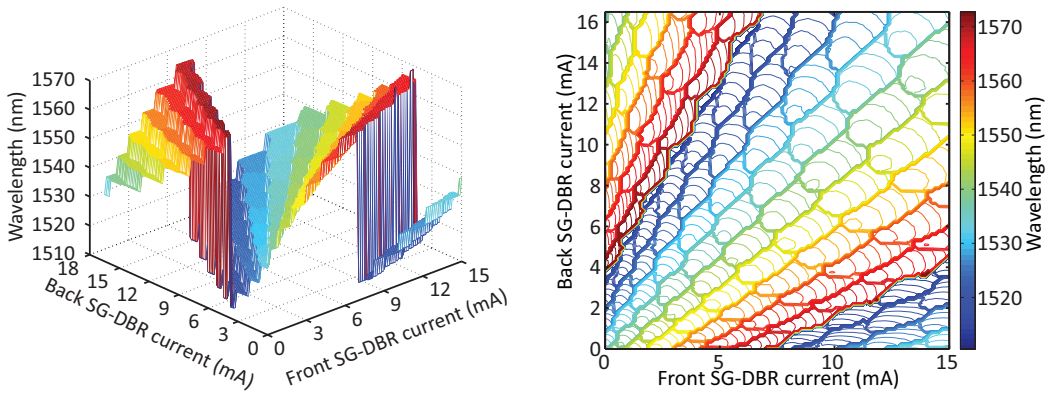

(a) (b)

Figure 3.6: Wavelength tuning curve of a SG-DBR laser. (a)3-D surface obtained by varying both the front and back SG-DBR current. (b)The contour of the 3-D curve in (a). Colour is used to delineate the wavelength.

Figure 3.4 to achieve fine tuning [16]. The longitudinal modes inside the same reflection peak is referred as to a supermode. In Figure 3.6b, each of the steps in the fan shaped wavelength tuning map represents a supermode, while the variation along the diagonal direction in each supermode are the longitudinal mode hops. The two boundaries of modes between the wavelength of 1570 nm and 1510 nm are called cycling jumps, which is due to the fact that the wavelength shift of one reflective comb (red line in Figure 3.5) is higher than the comb spacing of the other fixed grating (blue line in Figure 3.5). This is also called the repeat mode spacing which is equal to $F \cdot P_{ave}$ and limits the tuning range of the laser under the simulation to approximately 60nm.

The SG-DBR laser is just an example of using the Vernier effect to extend the tuning range. Other types of gratings with comb-like reflective spectrum can be used as well such as the SSG-DBR laser [9, 17]. In addition, the Vernier effect can be applied to the longitudinal modes from two cavities which have a different length [18]. An optimized coupling coefficient of both the phase and amplitude between the two sections is necessary to achieve better tuning capability [19] and higher SMSR [20]. Nevertheless, the Vernier effect is not the only method to achieve a wide tuning range of electronic switched lasers. The range of wavelength selection can be extended by using a set of gratings, each of which has a different Bragg wavelength [2]. As the sub-band of the total tuning range is selected digi-

tally, this grating structure is referred to as the digital supermode distributed Bragg reflector (DS-DBR) [21, 22]. A grating-assisted co-directional coupler (GACC) is a widely tunable coupler (> 60 nm) with low selectivity (~ 6 nm) of which the refractive index tuning range is relative to the difference in the index between the two coupled waveguide [23]. A second SG-DBR or SSG-DBR is required for the Grating assisted co-directional Coupler with Sampled Reflector (GCSR) lasers to maintain a relative high SMSR (> 30 dB). Analogous to GCSR and DS-DBR using combinations of various tuning and mode selectivity features, by having SG-DBR or SSG-DBR in the two passive branches of a Y-structure laser [24], an 'additive' Vernier effect is achieved, providing a better SMSR, because the two reflections from the branches are added in the modulated Y-structure (MGY) laser [25]. However the fabrication of the Bragg gratings especially sampled gratings requires sub-micro lithography and multiple epitaxial regrowth steps, which significantly increase the complexity and cost while reduce the yield.

3.2.2 Wavelength Switching

The wavelength of the longitudinal modes and the Bragg wavelength of the grating are both dependent on the refractive index and hence the switching characteristics of the tunable semiconductor laser are decided by the dynamics of the carrier density in the tuning sections of the laser, which is derived from equation (3.8) by neglecting the consumption of the carrier due to stimulated emission [3].

A static wavelength tuning curve as a function of the current on the front SG-DBR is plotted in Figure 3.7 along with a diagram illustrating the mode competition. The corresponding SMSR tuning curve is shown as the green dotted line in Figure 3.7a. At point **i**, the mode competition is between two adjacent longitudinal modes inside the same comb-like reflection peak (see the top figure in Figure 3.7b). When the current of the front grating is increased, as shown in Figure 3.5, the next aligned reflection peak moves to the adjacent peak with a higher wavelength, which agrees with the results in Figure 3.5. Therefore the most dominant side-mode changes from the adjacent longitudinal mode in the same reflection peak to the one in the adjacent reflection peak (see the middle figure in Figure 3.7b),

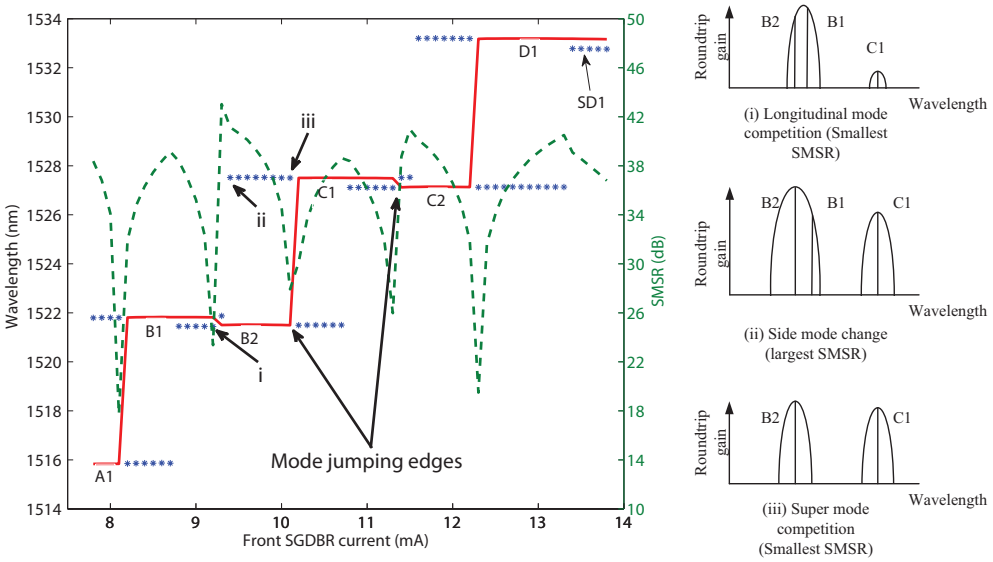

(a) (b)

Figure 3.7: (a)A static tuning curve of the switching range. The red step like line represents the main mode and the blue stars represent the corresponding side mode with the same tuning current. (b) A brief illustration of the mode competition of the three points in (a). (i) Adjacent longitudinal mode competition. (ii) Side mode change from adjacent longitudinal mode to the one in another roundtrip gain peak. (iii) Longitudinal modes in different roundtrip gain peaks competition.

where the highest SMSR is achieved. As the current further increases to point **iii**, the mode competition between the longitudinal modes in two different reflection peaks reaches the maximum, resulting in a mode jump corresponding to a drop in the SMSR tuning curve.

To investigate the wavelength switching dynamics, we apply a switching current I_{f} to the front SG-DBR, which is defined by:

$$I_{\mathrm{f}} = \begin{cases} I_{\mathrm{f1}} & t < t_{10}, \\ I_{\mathrm{f1}} + (I_{\mathrm{f2}} - I_{\mathrm{f1}}) \left(1 - e^{-\frac{t-t_{10}}{\tau_0}}\right) & t_{10} \leq t < t_{20}, \\ I_{\mathrm{f2}} - (I_{\mathrm{f2}} - I_{\mathrm{f1}}) \left(1 - e^{-\frac{t-t_{20}}{\tau_0}}\right) & t \geq t_{20}, \end{cases} \tag{3.14}$$

where I_{f1} and I_{f2} are the low and high levels of the switching current pulses, respectively, t_{10} and t_{20} are the time when the amplitude of the switching current starts to change, and τ_0 is the time constant. The mode competition during the switching from mode A1 to mode

D1 in Figure 3.7 is presented in Figure 3.8a based on the simulation using TMM and equations (3.7) and (3.8), where the green dotted line is the switching pulse with $I_{\mathrm{f1}} = 7.8mA$ and $I_{\mathrm{f2}} = 13.8mA$ [26]. The modes between the source mode (A1) and the destination mode (D1) lase successively (B1-B2-C1-C2) as the current increase from the low level to the high level and vice versa. The switching time is defined as the time from when the laser intensity of the source mode drops to 90% of its steady state value to when the laser intensity of the destination mode reaches 90% of its steady state value [27]. The forward switching (corresponding to the increase of the current) time is approximately 5 ns while the backward switching (corresponding to the decrease of the current) time is approximately 14 ns.

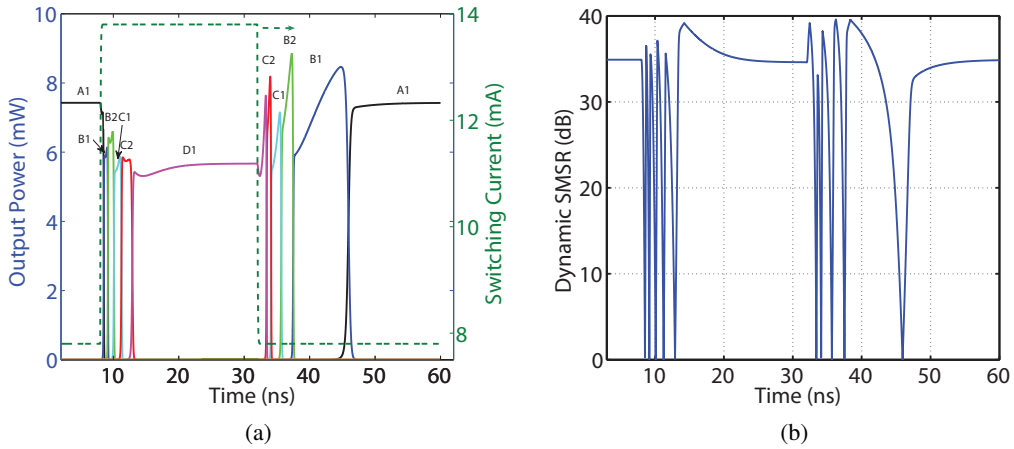

Figure 3.8: Transient characteristics of wavelength switching. (a) Output mode power, where the dot line represents the current applied on the front SG-DBR section. (b) Dynamic SMSR.

The backward switching time is found to be longer than the forward switching time which is due to the fact that the dynamics of the carrier density enhances the lasing of transient modes for a longer period, in particular mode B1 [28]. As shown in Figure 3.9, the 10 % to 90 % rise time of the carrier density is found to be 1.8 ns shorter than the corresponding fall time. Figure 3.9 also conveys that with a higher amplitude of the current pulse (7.8 to 13.8 mA), the carrier density can reach the same level ($9 \times 10^{23}/\mathrm{m}^3$) approximately 2.6 ns quicker than the case with a lower amplitude pulse (7.8 to 12.5 mA). Since the wavelength of the laser is related to the carrier density, a shorter forward switching time can be

achieved by using a pre-emphasis technique which modifies the drive current from a square wave to a wave with overshoot and undershoot at the rise and falling edge respectively [29].

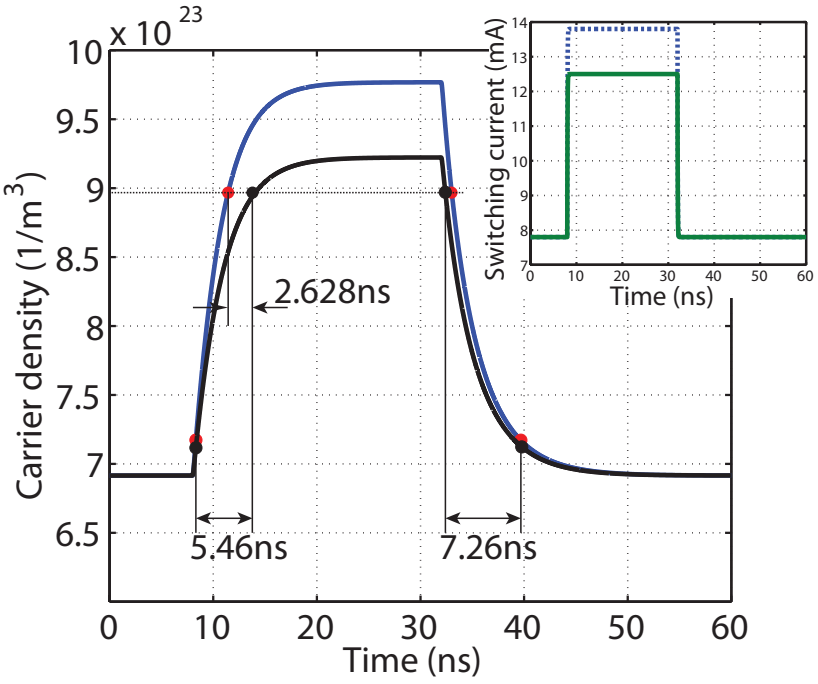

Figure 3.9: Time response of the carrier density of the front SG-DBR by a pulse-current with two different high levels (inset).

Wavelength switching between all channel combinations of a 64-channels SG-DBR laser in less than 5 ns has been achieved by using pre-emphasis amplitudes [27]. Figure 3.8b displays the evolution of the SMSR during the switching, which is referred to as the dynamic side-mode suppression ratio (DSMSR). The transient of DSMSR suffers degradations during switching due to the mode competition. Experimental results indicate that the period of deterioration of the DSMSR is almost two times longer than the switching time defined by the power of the source and destination modes [30]. These results confirm the possible performance degradations of WDM systems due to the 'pollution' resulting from the lasing of the intermediate modes (B1-C2). Thus, an integrated semiconductor optical amplifier (SOA) is desirable as a shutter to block the optical signal during the switching events (see Figure 3.4) [31]. For wavelength switching dynamics, other important issues that need to be studied are thermal effects and nonlinear gain. Nonlinear gain will possibly

lead to hysteresis in wavelength versus temperature characteristics [32]. Thermal effects can cause wavelength drift which will have a detrimental effect on system performance for some applications requiring fast switching [33]. A laser designed with low tuning currents is available to manage the parasitic thermal tuning [27].

3.3 Summary

In this chapter, the fundamentals of the FP laser are introduced. The FP laser has a lack of mode selection and lases with multiple longitudinal modes. The Bragg grating is used to select modes and yield single-mode lasing with high SMSR. By applying a sampling function on the conventional Bragg grating, a comb-like reflective spectrum is obtained and the spacing between each comb line is decided by the period of the sampling function. As the refractive index of the semiconductor laser can be controlled by injecting current or varying temperature, the wavelength of a semiconductor laser becomes tunable through different mechanisms. The tunable ECL, VCSEL and the microarray source have many features which are ideal for optical communication systems, such as narrow linewidth, a wide tuning range and are easily integrated into arrays. However, the long switching time, resulting from mechanical and thermal tuning effects, make these types of tunable lasers only useful for low speed applications in optical switching networks such as sparing and protection.

Electronic tuning lasers using free-carrier plasma effects can achieve switching times in the order of nanoseconds due to the short carrier lifetime. The limitations of the tuning range are overcome by using the Vernier effect, where two comb-like reflective spectra with slightly different spectral spacing and only one pair of the reflective peaks are aligned at a time. The static tuning method of the SG-DBR laser has been explained by simulation based on the TMM method. Then the switching dynamics are calculated by using the multi-mode rate equations approach. The mode competition during the switching, described by the DSMSR, is investigated which shows the importance of blocking the laser output during the switching process, in order to avoid interference with other WDM channels. The fast

switching time along with the wide tuning range make the SG-DBR an ideal candidate for optical switching networks which require nanosecond scale switching time, such as OPS and OBS.

For on-off keying (OOK) systems employing tunable lasers; the optical power, the tuning range, the SMSR and the switching speed are the main parameters that attract the most concern from the equipment providers. For tunable lasers being employed in coherent systems with both the amplitude and phase of the optical carrier being modulated, the phase noise of the laser is becoming more important. Hence, the characterization of the phase noise of fast tunable semiconductor lasers is vital for the system design. In the following chapter, the linewidth of the SG-DBR and its effect in system performance is characterized for both static and dynamic situations.

References

[1] J. Buus, "The effective index method and its application to semiconductor lasers," *IEEE Journal of Quantum Electronics*, vol. 18, no. 7, pp. 1083– 1089, Jul. 1982.

[2] J. Buus, M. Amann, and D. J. Blumenthal, *Tunable Laser Diodes and Related Optical Sources*, 2nd ed. Wiley-IEEE Press, Feb. 2005.

[3] L. Zhang and J. C. Cartledge, "Fast wavelength switching of three-section DBR lasers," *IEEE Journal of Quantum Electronics*, vol. 31, no. 1, pp. 75–81, Jan. 1995.

[4] J. Carroll, *Distributed feedback semiconductor lasers*. London: The Institution of Electrical Engineers [etc.], 1998.

[5] G. Agrawal, *Long-wavelength semiconductor lasers*. New York: Van Nostrand Reinhold, 1986.

[6] G. Bjork and O. Nilsson, "A new exact and efficient numerical matrix theory of complicated laser structures: properties of asymmetric phase-shifted DFB lasers," *Journal of Lightwave Technology*, vol. 5, no. 1, pp. 140– 146, Jan. 1987.

[7] L. A. Coldren, "Monolithic tunable diode lasers," *IEEE Journal of Selected Topics in Quantum Electronics*, vol. 6, no. 6, pp. 988–999, Dec. 2000.

[8] V. Jayaraman, Z. M. Chuang, and L. A. Coldren, "Theory, design, and performance of extended tuning range semiconductor lasers with sampled gratings," *IEEE Journal of Quantum Electronics*, vol. 29, no. 6, pp. 1824–1834, Jun. 1993.

[9] H. Ishii, F. Kano, Y. Tohmori, Y. Kondo, T. Tamamura, and Y. Yoshikuni, "Narrow spectral linewidth under wavelength tuning in thermally tunable super-structure-grating (SSG) DBR lasers," *IEEE Journal of Selected Topics in Quantum Electronics*, vol. 1, no. 2, pp. 401–407, Jun. 1995.

[10] L. Coldren, G. Fish, Y. Akulova, J. Barton, L. Johansson, and C. Coldren, "Tunable semiconductor lasers: A tutorial," *Journal of Lightwave Technology*, vol. 22, no. 1, pp. 193–202, Jan. 2004.

[11] F. Riemenschneider, M. Maute, H. Halbritter, G. Boehm, M. C. Amann, and P. Meissner, "Continuously tunable long-wavelength MEMS-VCSEL with over 40-nm tuning range," *IEEE Photonics Technology Letters*, vol. 16, no. 10, pp. 2212–2214, Oct. 2004.

[12] J. D. Berger, Y. Zhang, J. D. Grade, H. Lee, S. Hrinya, and H. Jerman, "Widely tunable external cavity diode laser based on a MEMS electrostatic rotary actuator," in *Optical Fiber Communication Conference and Exhibit, 2001. OFC 2001*, vol. 2. IEEE, Mar. 2001, pp. TuJ2–TuJ2.

[13] C. J. Chang-Hasnain, "Tunable VCSEL," *IEEE Journal of Selected Topics in Quantum Electronics*, vol. 6, no. 6, pp. 978–987, Dec. 2000.

[14] H. Hatakeyama, K. Kudo, Y. Yokoyama, K. Naniwae, and T. Sasaki, "Wavelength-selectable microarray light sources for wide-band DWDM applications," *IEEE Journal of Selected Topics in Quantum Electronics*, vol. 8, no. 6, pp. 1341– 1348, Dec. 2002.

[15] G. Sarlet, G. Morthier, and R. Baets, "Control of widely tunable SSG-DBR lasers for dense wavelength division multiplexing," *Lightwave Technology, Journal of*, vol. 18, no. 8, pp. 1128–1138, 2000.

[16] R. O'Dowd, S. O'Duill, G. Mulvihill, N. O'Gorman, and Y. Yu, "Frequency plan and wavelength switching limits for widely tunable semiconductor transmitters," *IEEE Journal of Selected Topics in Quantum Electronics*, vol. 7, no. 2, pp. 259–269, Apr. 2001.

[17] H. Ishii, F. Kano, Y. Yoshikuni, and H. Yasaka, "Mode stabilization method for superstructure-grating DBR lasers," *Lightwave Technology, Journal of*, vol. 16, no. 3, pp. 433–442, 1998.

[18] L. Coldren and T. Koch, "Analysis and design of coupled-cavity lasers–Part i: Threshold gain analysis and design guidelines," *IEEE Journal of Quantum Electronics*, vol. 20, no. 6, pp. 659– 670, Jun. 1984.

[19] F. K. Khan and D. T. Cassidy, "Widely tunable coupled-cavity semiconductor laser," *Applied Optics*, vol. 48, no. 19, pp. 3809–3817, Jul. 2009.

[20] J. Jin, L. Wang, T. Yu, Y. Wang, and J. He, "High side-mode suppression ratio widely wavelength switchable v-coupled-cavity semiconductor laser," *Optics Letters*, p. accepted for publication, 2011.

[21] A. J. Ward, D. J. Robbins, G. Busico, N. D. Whitbread, P. J. Williams, D. C. Reid, and J. R. Rawsthorne, "Modelling of phase-grating based wideband tuneable lasers with simplified quasi-digital wavelength selection," *Optoelectronics, IEE Proceedings -*, vol. 150, no. 2, pp. 199– 204, Apr. 2003.

[22] A. J. Ward, D. J. Robbins, G. Busico, E. Barton, L. Ponnampalam, J. P. Duck, N. D. Whitbread, P. J. Williams, D. C. Reid, A. C. Carter, and M. J. Wale, "Widely tunable DS-DBR laser with monolithically integrated SOA: design and performance," *IEEE Journal of Selected Topics in Quantum Electronics*, vol. 11, no. 1, pp. 149– 156, Feb. 2005.

[23] M. Oberg, S. Nilsson, K. Streubel, J. Wallin, L. Backbom, and T. Klinga, "74 nm wavelength tuning range of an InGaAsP/InP vertical grating assisted codirectional coupler laser with rear sampled grating reflector," *IEEE Photonics Technology Letters*, vol. 5, no. 7, pp. 735–737, Jul. 1993.

[24] O. Hildebrand, D. Baums, W. Idler, K. Dutting, G. Laube, and K. Wunstel, "The y-laser: a multifunctional device for optical communication systems and switching

networks," *Journal of Lightwave Technology*, vol. 11, no. 12, pp. 2066–2075, Dec. 1993.

[25] J. O. Wesstrom, S. Hammerfeldt, J. Buus, R. Siljan, R. Laroy, and H. de Vries, "Design of a widely tunable modulated grating y-branch laser using the additive vernier effect for improved super-mode selection," in *Semiconductor Laser Conference, 2002. IEEE 18th International*. IEEE, 2002, pp. 99– 100.

[26] K. Shi, Y. Yu, R. Zhang, W. Liu, and L. P. Barry, "Static and dynamic analysis of side-mode suppression of widely tunable sampled grating DBR (SG-DBR) lasers," *Optics Communications*, vol. 282, no. 1, pp. 81–87, Jan. 2009.

[27] J. E. Simsarian, M. C. Larson, H. E. Garrett, H. Xu, and T. A. Strand, "Less than 5-ns wavelength switching with an SG-DBR laser," *IEEE Photonics Technology Letters*, vol. 18, no. 4, pp. 565–567, Feb. 2006.

[28] Y. Yu and R. O'Dowd, "Influence of mode competition on the fast wavelength switching of an SG-DBR laser," *Journal of Lightwave Technology*, vol. 20, no. 4, pp. 700–704, Apr. 2002.

[29] P. J. Rigole, M. Shell, S. Nilsson, D. J. Blumenthal, and E. Berglind, "Fast wavelength switching in a widely tunable GCSR laser using a pulse pre-distortion technique," in , *Conference on Optical Fiber Communication. OFC 97*. IEEE, Feb. 1997, pp. 231–232.

[30] J. P. Engelstaedter, B. Roycroft, F. H. Peters, and B. Corbett, "Heterodyne method for time resolved spectral analysis of fast laser wavelength switching," *IEEE Photonics Technology Letters*, vol. 21, no. 20, pp. 1517–1519, Oct. 2009.

[31] L. Ponnampalam, N. D. Whitbread, R. Barlow, G. Busico, A. J. Ward, J. P. Duck, and D. J. Robbins, "Dynamically controlled channel-to-channel switching in a full-band DS-DBR laser," *IEEE Journal of Quantum Electronics*, vol. 42, no. 3, pp. 223– 230, Mar. 2006.

[32] K. Petermann, *Laser diode modulation and noise*. Dordrecht ;;Boston ;Tokyo ;Norwell MA: Kluwer Academic Publishers ;;KTK Scientific Publishers ;;Sold and distributed in the U.S.A. and Canada by Kluwer Academic Publishers, 1991.

[33] H. Wang and Y. Yu, "A new theoretical model to analyze temperature distribution and influence of thermal transients of an SG-DBR laser," *IEEE Journal of Quantum Electronics*, vol. PP, no. 99, pp. 1–1, Sep. 2011.

Chapter 4

Characterization of SG-DBR Lasers

As seen in Chapter 2, reconfigurable and fast switching networks are becoming imperative for tackling the bottleneck problems caused by increasing data rates. Meanwhile, advanced modulation formats along with coherent or self-coherent receivers have been widely used in long-haul transmission systems to improve the spectral efficiency (SE), and therefore the aggregate data rate of a single wavelength-division multiplexing (WDM) channel is further increased. In Chapter 3, electronically controlled tunable lasers which can be switched in nanosecond time-scales, due to short carrier lifetimes, are demonstrated. Sampled-grating distributed Bragg reflector (SG-DBR) lasers using the Vernier effect have achieved a wide tuning range, high side-mode suppression ratio (SMSR) and switching time of nanoseconds, which make them a good candidate for the use as a transmitter in coherent dynamic networks.

For optical switching systems employing on-off keying (OOK), the mode power and the SMSR are the main parameters that affect the transmission and switching performance. However, for coherent systems, the phase noise of semiconductor lasers at a fixed wavelength or during a wavelength switching event becomes increasingly more important. In this chapter, the phase noise of SG-DBR lasers and its effect in self-coherent systems will be discussed. First, the theory of the phase noise of tunable semiconductor lasers will be briefly introduced. Subsequently, the phase noise of SG-DBR lasers will be characterized and the performance degradation due to the linewidth effect of the laser in a differential

binary phase shift keying (DPSK) transmission system will be examined. In addition, a calibration method will be presented to locate narrow linewidth operating points of the laser. Next, a method of measuring the dynamic linewidth of SG-DBR lasers during fast wavelength switching events will be shown, and the time-resolved bit error rate (BER) of a packet switching differential quadrature phase shift keying (DQPSK) system will also be investigated.

4.1 Laser Phase Noise

The phase noise of single mode semiconductor lasers originates from spontaneous emission. For widely tunable lasers such as SG-DBR lasers using passive tuning sections, additional noise is introduced as there is no gain-clamping mechanism in the current controlled tuning sections. The phase noise of a laser is normally measured by the full-width half-maximum (FWHM) spectral width, and this linewidth is broadened as a result of the additional noise introduced in the passive sections. In this section, different types of phase noise of electronically tuned semiconductor lasers will be studied and different characterization techniques will be investigated.

4.1.1 White FM Noise

The effect of spontaneous emission events is illustrated in Figure 4.1. According to the theory developed by Henry [1], each spontaneous emission event causes a phase and an intensity change:

$$\Delta\phi_i = P^{-1/2}\sin(\theta_i) \tag{4.1}$$

$$\Delta P_i = 2P^{-1/2}\cos(\theta_i) + 1, \tag{4.2}$$

where, the average intensity, P, is chosen to be equal to the average number of photons in the cavity by using a normalized complex amplitude of the optical field collaboration:

$$E(t) = \sqrt{P(t)}\exp(j\phi(t)) \tag{4.3}$$

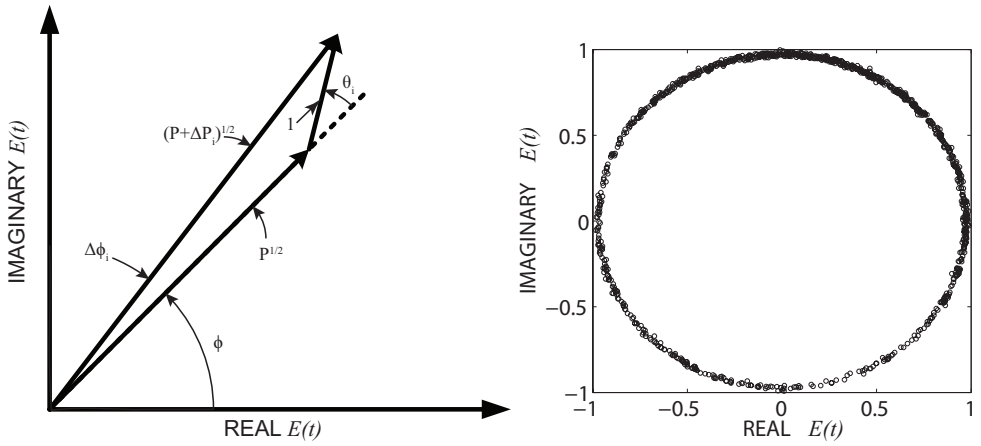

(a) (b)

Figure 4.1: (a) The instantaneous changes of the phase, ϕ, and intensity, I, of the optical field caused by the i th spontaneous emission event (adapted from [1]). (b) Complex amplitude, E, for laser light.

where, $\phi(t) = \omega_0 t + \phi_0 + \phi_{ns}$. ϕ_0 is the initial phase and ϕ_{ns} is the laser phase noise as denoted by Seimetz [2]. These fluctuations alter the phase of the optical field directly as described by equation (4.1). Meanwhile, the instantaneous change in field intensity causes relaxation oscillations of carrier density in the laser in order to restore steady-state field intensity. The wavelength of the laser is related to the refractive index and therefore the carrier density as shown in equation (3.12). Hence, the intensity fluctuations due to spontaneous emissions result in a delayed phase shift of the laser field [1]. These two effects can be in incorporated into the rate equations by adding Langevin force terms $F_\phi(t)$ and $F_P(t)$ [3]. Considering a single mode lasing for simplicity, equation (3.7) may then be written as:

$$\frac{dP(t)}{dt} = v_g \cdot (g - \alpha) \cdot P(t) + R_{ps} + F_P(t). \tag{4.4}$$

Similarly one may write the phase rate equation as:

$$\frac{d\phi(t)}{dt} = \frac{1}{2}\alpha_H g_N \left(N\left(t\right) - N_{th}\right) + F_\phi(t), \tag{4.5}$$

where,

$$\alpha_H = -\frac{\partial n^{'}/\partial N}{\partial n^{''}/\partial N} \tag{4.6}$$

represents the coupling between the imaginary and real parts of the refractive index, which yield the delayed phase fluctuations. N_{th} is the threshold carrier density from the steady state solution of equation (3.8). The spectral density of the frequency noise (FM-noise), derived from the equations above, is given as:

$$W_{\dot{\phi}_{ns}} = \frac{R_{sp}}{2P}(1 + \alpha_H^2 |H(j\omega)|^2), \tag{4.7}$$

where, $|H(j\omega)|$ is the small signal modulation transfer function [3]. For frequencies $\omega_m \ll \omega_r$, where ω_r denotes the relaxation resonance frequency, the FM-noise spectrum can be considered as white noise with $W_{\dot{\phi}_{ns}} = \frac{R_{sp}}{2P}(1 + \alpha_H^2)$.

The phase of the laser can therefore be understood as a random walk. Within a time interval τ, the phase exhibits a random phase change of:

$$\Delta\phi_{ns}(\tau) = \phi_{ns}(t) - \phi_{ns}(t - \tau). \tag{4.8}$$

Figure 4.1b shows the random walk process of a laser module simulated by using a commercial software package (VPIsystems). A total number of 1024 samples at 156.25 M samples per second are plotted with the linewidth of the laser module being set as 1 MHz. For white FM-noise, the mean square value of this phase change is obtained as [3]:

$$\begin{aligned} \langle \Delta\phi_{ns}^2 \rangle &= \langle (\phi_{ns}(t) - \phi_{ns}(t - \tau))^2 \rangle \\ &= -\frac{\tau^2}{2\pi} \int_{-\infty}^{+\infty} W_{\dot{\phi}_{ns}} \frac{\sin^2(\omega\tau/2)}{(\omega\tau/2)^2} d\omega \qquad (4.9) \\ &= W_{\dot{\phi}_{ns}} |\tau|. \qquad (4.10) \end{aligned}$$

The power spectral density (PSD) of the field, $E(t)$, is then obtained and exhibits a Lorentian-shaped spectrum [2, 3]:

$$W_E(\omega) = \frac{2\tau_c P}{1 + [(\omega - \omega_0)]^2} \tag{4.11}$$

which is centred at ω_0 with a FWHM bandwidth of:

$$\Delta\nu = \frac{\Delta\omega}{2\pi} = \frac{1}{\pi\tau_c} = \frac{W_{\dot{\phi}_{ns}}}{2\pi}. \tag{4.12}$$

If the frequency, f (Hz), is used instead of angular frequency, ω (rad/s), the relationship above is modified as $\Delta\nu = W_{\dot{\phi}_{ns}f}\pi$, where $W_{\dot{\phi}_{ns}f}$ represents the FM spectrum density as a function of frequency measured in Hz [4, 5]. The linewidth of semiconductor laser derived from spontaneous emissions is also referred to as the Schawlow Townes-Henry linewidth.

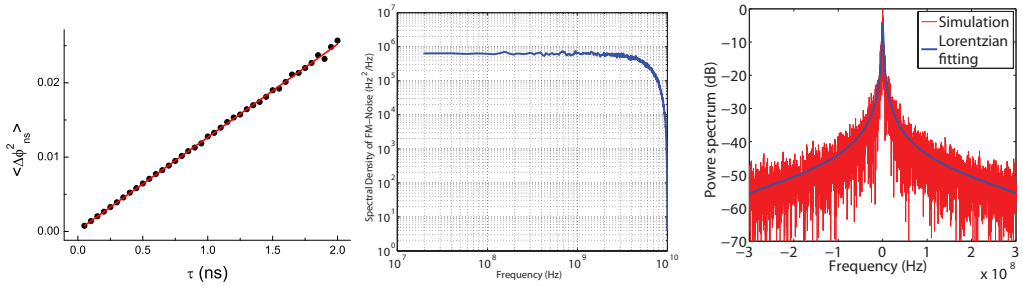

(a) (b) (c)

Figure 4.2: (a) The mean square value of the phase change. (b) The FM-noise spectrum. (c) The field spectrum.

The mean square value of the random phase change, the FM spectrum and the PSD for the optical field are calculated based on the simulated data in Figure 4.1b and the results are displayed in Figure 4.2. In order to get an accurate estimation, the number of samples in Figure 4.1b is extended to 2^{17} at a sampling rate of 20 GHz while the set linewidth value remains 1 MHz . The linear relationship between the mean square value of the phase change described by equation (4.10) is explicitly demonstrated in Figure 4.2a. The slope of the linear fitting is 1.25288e7 $\mathrm{rad}^2/\mathrm{s}$, which yields a value of 1.9940 MHz. The actual calculated value is double of the set value (1 MHz), which is due to a homodyne method being used to characterize the linewidth in the simulation. This results in a convolution between the optical spectrum and the delayed replica. The FM-noise spectrum is plotted in Figure 4.2b. The spectral density is approximately constant from 10 MHz to 1 GHz with an average value of $6.3002 \times 10^{-5}\mathrm{Hz}^2/\mathrm{Hz}$. The roll-off of the curve after 1 GHz is due to the

finite sampling rate which limits the signal bandwidth to the Nyquist frequency. According to equation (4.12), the calculated linewidth from the FM-noise spectrum is 1.9793 MHz. The optical field spectrum is shown in Figure 4.2c along with a Lorentzian fit. The FWHM bandwidth of the fitting curve is 2.2622MHz. The two values calculated from the FM-noise spectrum and the optical field spectrum are twice of the set value. This is also caused by the use of the homodyne method. A detailed description of the linewidth measurement techniques will be given in Sections 4.2 and 4.3. The results above have proven the relationship between the laser linewidth, the mean square value of the the phase change and the FM-noise spectral density as described in equations (4.9), (4.11) and (4.12).

4.1.2 Additional FM Noise

Strong linewidth broadening caused by additional FM-noise has been observed for multi-section electronically tuned semiconductor lasers using the free-carrier plasma effect [6, 7]. There are two main contributions to the additional FM-noise: the injection-recombination shot noise (IRSN) and the 1/f noise. These two types of FM-noise are exhibited not only in the passive sections but also the active sections of multi-section tunable lasers. However, the gain-clamping mechanism suppresses carrier density fluctuations in the active sections. Therefore, the linewidth broadening, induced by the additional FM-noise, has much less effect in the active section and can usually be neglected [8, 9].

The IRSN is caused by the shot noise effect of the carrier injection and recombination leading to instantaneous frequency fluctuations. The power spectral density of this type of FM-noise is given as [8]:

$$W_{\dot{\phi}_{ns}} = 4e\frac{c^2}{\lambda^4}\left(\frac{d\lambda}{dI_t}\right)^2 \frac{I_{t0}}{1+(2\pi f\tau_d)^2}, \tag{4.13}$$

where, I_{to} is the average tuning current in the passive section and τ_d is the differential carrier density lifetime. The excess linewith broadening due to the IRSN in the tuning section is then obtained as [9]:

$$\Delta\nu_{ex} = 4\pi\left(f_e\tau_d\right)^2\frac{I_t}{e}, \tag{4.14}$$

where, f_e represents the tuning efficiency.

Although the IRSN may explain the major part of the tuning-induced linewidth broadening of the electronically tuned lasers, a larger broadening is still observed. This noise is attributed to the occurrence of a 1/f noise in the current tuning multi-section semiconductor laser [8]. The nature of the 1/f noise is not clear at present, and some of the papers by Amann show that this additional broadening stems from the internal noise sources, which could be the recombination at the surfaces of the tuning sections [8, 10].

4.1.3 Phase Noise Characterization Methods

As we have seen, since tunable semiconductor lasers exhibit different types of FM-noise, it is therefore vital to accurately characterize the phase noise of these devices. The laser phase noise is usually characterized by measuring the linewidth of the laser which is defined in terms of the FWHM of the PSD of the optical field (see Figure 4.2c). Grating-based optical spectrum analysers do not offer the measurement resolution required for laser linewidth measurement. Coherent detection can be employed to downshift the signal from an optical frequency to an intermediate frequency (IF) (f_{IF}), where an RF spectrum analyser (also known as the electrical spectrum analyser (ESA)) with excellent spectral resolution can be utilized [11]. There are mainly two categories of coherent detection distinguished by whether an local oscillator (LO) or a decorrelated replica of the incident light is used to down convert the signal to the RF domain, and these are referred to as heterodyne and homodyne measurements respectively.

Today's current controlled multi-section widely tunable lasers, such as SG-DBR lasers, can readily cover a tuning range of more than 40 nm by varying the current on the tuning sections. Hence, the wavelengths of the LO in a heterodyne system need to be adjusted to keep the IF within the bandwidth of the ESA, while the lasing wavelength of the tunable laser is changing during a characterization of all current combinations. Therefore, it is difficult to use automatic control when characterizing laser linewidths [12]. Hence, homodyne detection is desired for the linewidth measurement of widely tunable semiconductor lasers where the requirement of an LO is eliminated. However, the central RF frequency is

zero for the homodyne measurement while most ESAs have high noise levels in the very low-frequency region. Laser intensity noise may also significantly affect the measurement accuracy [11].

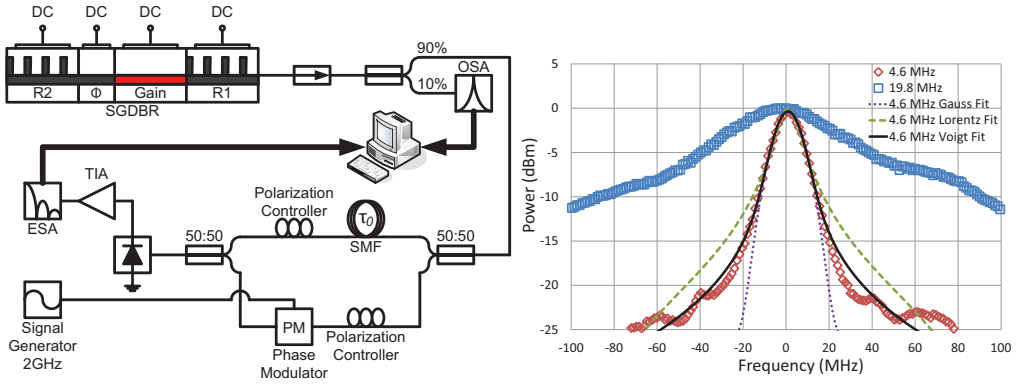

(a) (b)

Figure 4.3: (a) Experimental setup of the linewidth characterization using the delayed self-heterodyne method. (b) Measured lineshape of the SG-DBR laser with a linewidth of 19.8 MHz (□) and 4.6 MHz (♢). The lineshape is also fitted with a Lorentzian (solid black line), a Gaussian (purple dots) and a Voigt (green dashes) function respectively.

To improve the performance of the homodyne measurement, the IF is moved away from DC and set to greater than $\Delta\nu$ to avoid the accuracy concern at the low-frequency region [11, 12]. This leads to the use of self-heterodyne measurement. Figure 4.3a shows the setup of the delayed self-heterodyne linewidth measurement technique, where a $LiNbO_3$ phase modulator is used to frequency shift the detected heterodyne beat signal to 2 GHz thereby enhancing the measurement accuracy. The differential delay of the fibre is required to be much longer than the coherence time of the optical signal ($\Delta\tau \gg \tau_c$). The fibre delay of a 12 km single mode fibre (SMF) is approximately 60 μs, which corresponds to a frequency resolution of 17 kHz for the linewidth measurement.

The lineshape measured using the self-heterodyne method for two operating points of an SG-DBR laser is displayed in Figure 4.3b. By fitting the lineshape with Lorentzian, Gaussian and Voigt functions, the lineshape of the SG-DBR laser is found to be closer to the Voigt function. The self-heterodyne spectrum of the laser is the convolution of the Lorentzian spectrum associated with the white frequency noise and the approximate Gaussian spectrum resulting from the 1/f noise [4]. However, high speed coherent systems are

much less dependent on the component of linewidth originating from the 1/f noise. A simple way to reduce the effect of this component on the linewidth value is to deduce the laser linewidth from the width of the lineshape 10 or 20 dB down from the peak. In the following sections, the linewidths measured by the self-heterodyne method are deduced from the -10 dB width of the lineshape except for those points for which the -10 dB width are not available because of strong lineshape broadening. In this case, we measured the -3 dB width. The actual linewith of the laser equals to the 1/2 of the 3 dB width while it equals $1/(2\sqrt{9})$ of the 10 dB width [12].

4.2 Phase Noise Characterization of SG-DBR Lasers

SG-DBR lasers consist of four sections, each controlled by a separate current source. Therefore, a set of four controlling currents (known as an "operating point") are required to give the emission at a particular international telecommunication union (ITU) specified wavelength. There are multiple potential operating points at the same emission wavelength, each of which exhibits different lasing parameters such as the SMSR and the linewidth. In this section, the importance of characterizing the phase noise of SG-DBR lasers will be shown, in order to choose the operating point where linewidth is narrow enough to support advanced modulation formats. A fast calibration method for SG-DBR lasers based on achieving narrow linewidth emission will also be proposed.

4.2.1 Effect of Linewidth on DPSK System

In order to examine the effect of linewidth on a DPSK transmission system, a relatively low bit rate at 1.25 Gb/s is chosen, as lower bit rates and higher orders of modulation format have more stringent requirement for laser linewidth. The system setup is shown in Figure 4.4. The transmitter consists of the SG-DBR laser tuned to the ITU grid channel at 194.2 THz followed by a Mach-Zehnder modulator (MZM) biased at the null point for the DPSK transmission. Four separate current controllers (Thorlabs ITC 502) are used to drive the laser. The noise characterization of the controller shows that it has a noise power

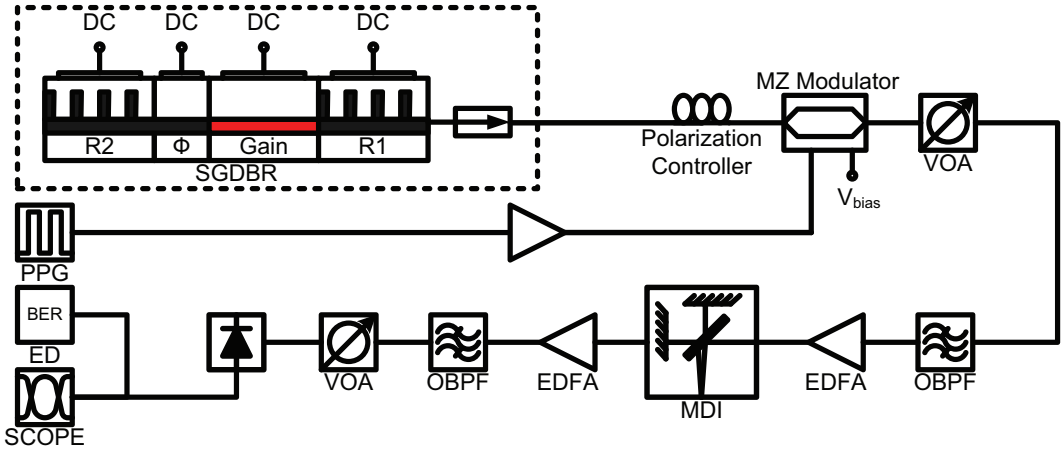

Figure 4.4: Experimental setup for DPSK transmission system.

of -75.00dBm over a span of 200MHz from DC. The modulator is driven by a $2^{31}-1$ bits pseudorandom bit sequence (PRBS) signal at 1.25 Gb/s from a pulse pattern generator (PPG). The power falling on the receiver is monitored and adjusted using a variable optical attenuator (VOA). The receiver consists of a pre-amplifier and a power amplifier. The erbium-doped fibre amplifiers (EDFAs) are both followed by 2nm optical bandpass filter (OBPF) to reduce the amplified spontaneous emission (ASE) noise. A Michelson delay interferometer (MDI) with a delay of 800 ps is used as a demodulator for the 1.25 Gb/s DPSK signal. The free-space MDI has approximately 10 dB loss, and has been placed after the first amplification stage to ensure that the power falling on the photoreceiver remains constant, which is adjusted by the second VOA. The photoreceiver is connected to the error detector and oscilloscope that are used to examine the system performance.

Table 4.1: Drive currents for the two operation points

I_a (mA)	I_f (mA)	I_b (mA)	I_p (mA)	Linewidth (MHz)
100	32.0	0	0	4.6
100	32.4	65.76	5.74	19.8

Two operating points in Figure 4.3b at the same ITU channel with linewidths of 19.8 MHz and 4.6 MHz are selected to investigate their effects on DPSK system. The drive current on each section of the laser for these two operating points is shown in Table 4.1. The

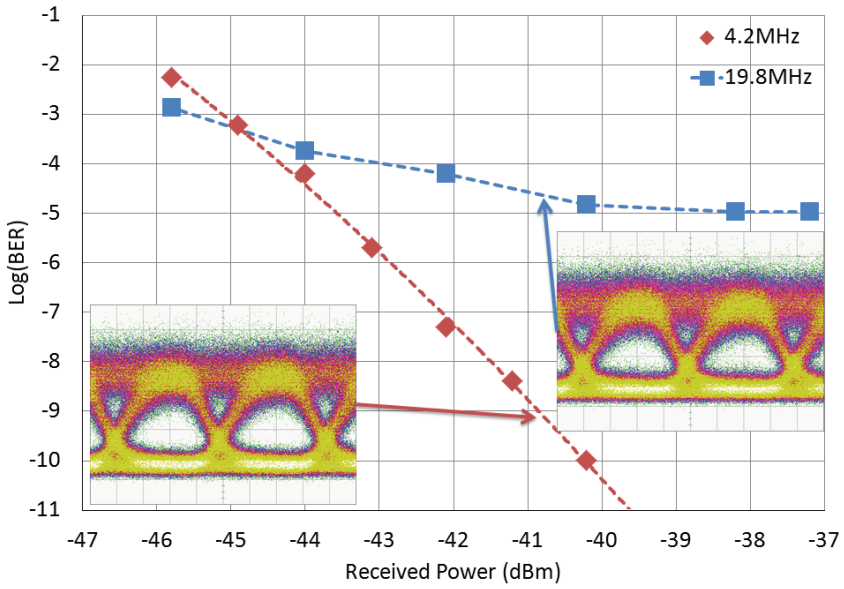

Figure 4.5: BER of 1.25 Gb/s DPSK transmission using a SG-DBR laser at 194.2 THz channel with a linewidth of 19.8MHz (♦) and 4.6MHz (■). The inset shows the received eye at power of -41.8 dBm for the two linewidth.

corresponding output power for these two operating points is +2.62 dBm and +3.95 dBm respectively. Although there is a large variation of linewidth, the SMSR of these two operating points are both above 50dB. The corresponding BER obtained from the error detector is shown in Figure 4.5. Error free DPSK transmission at linewidth of 4.6 MHz is achieved, whereas when the linewidth of the laser is 19.8 MHz, a hard error floor at 1×10^{-5} is observed. There is no further improvement of the BER when the received power is above -38 dBm. As described in Section 2.2.4, the product of the laser linewidth and the symbol period $\Delta\nu Ts$ is required to be less than 1% to operate with a $<$1 dB penalty at the BER equal to 10^{-4} for DPSK systems. Hence, the measurement results are in accordance with this criterion as the linewidth requirement at 1.25 Gb/s is approximately 12 MHz. The phase noise can be seen in the inset as the random dots spreading across the open eye. Linewidth of SG-DBR lasers can vary from 4 MHz to more than 20 MHz with different combinations of tuning currents. When the laser is employed in a transmission system utilizing advanced modulation formats, where the information is conveyed on both the intensity and phase of the optical carrier, it is imperative to include the laser linewidth into the calibration process

for these wavelength tunable devices.

4.2.2 Linewidth Characterization Results

The two comb-like reflection spectra produced by the front and back sampled gratings of SG-DBR lasers exhibit different spacing. Therefore, only one of the reflection peaks can be best aligned due to the Vernier effect. The phase current is used to frequency shift longitudinal modes in order to fine tune the emitted wavelength. The relative position between the longitudinal modes and the reflective spectra of the two reflectors varies with different combinations of drive current. As a result, the characteristics of the output of the laser fluctuate as the drive current changes.

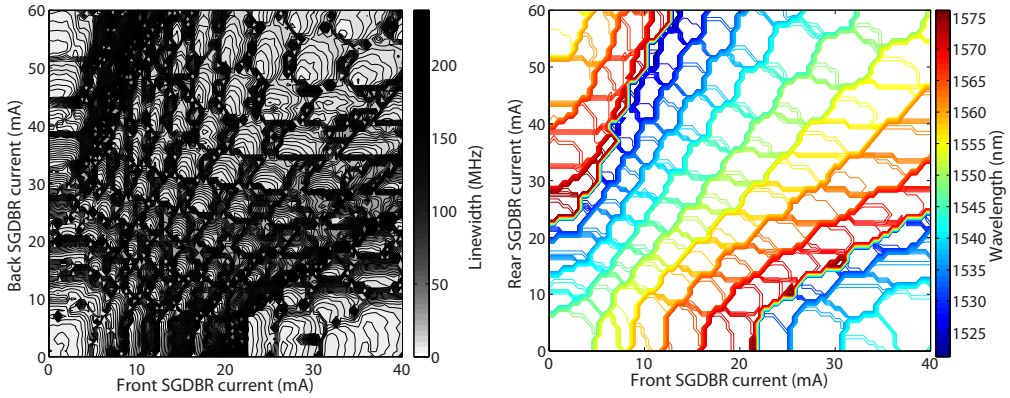

(a) (b)

Figure 4.6: The tuning maps of the SG-DBR laser versus front and back grating currents. (a) Linewidth. (b) Wavelength.

The delayed self-heterodyne method is used to measure the linewidth of a commercial SG-DBR laser from JDSU (see Figure 4.3a). Four identical current control modules (Thorlabs LDC8002) are used, and plugged into a rack chassis (Thorlabs PRO8000) with GPIB interface. The linewidth tuning map of the SG-DBR laser is shown in Figure 4.6a. The phase current and the gain current are set to 0 mA and 100 mA respectively. Compared to the wavelength tuning map in Figure 4.6b, it can be seen that the linewidth rises dramatically to tens of MHz at the mode boundaries and falls abruptly to around 5 MHz after the mode hop occurs. This is in qualitative agreement with the simulation results in [13]. How-

ever, the experiment showed a larger than expected degradation of the linewidth. This is attributed to the fact that carrier density variation caused by mode competition at the mode boundaries is not included into the Schawlow Townes-Henry linewidth.

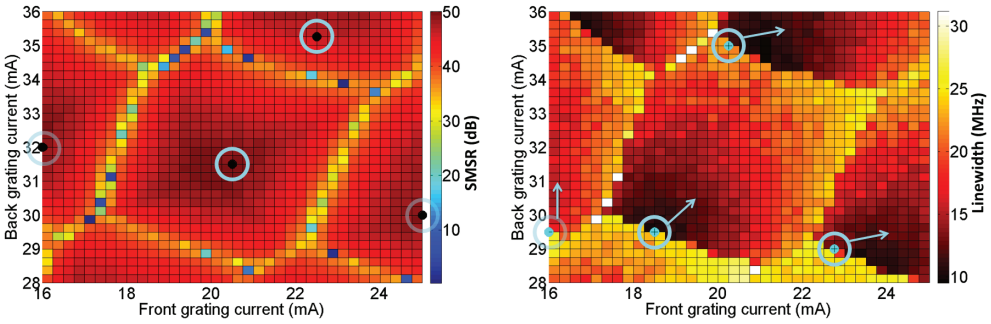

(a) (b)

Figure 4.7: Operating points (filled circles) with (a) highest SMSR and (b) lowest linewidth in different longitudinal modes. The arrows indicate the modes to which the operating points belong.

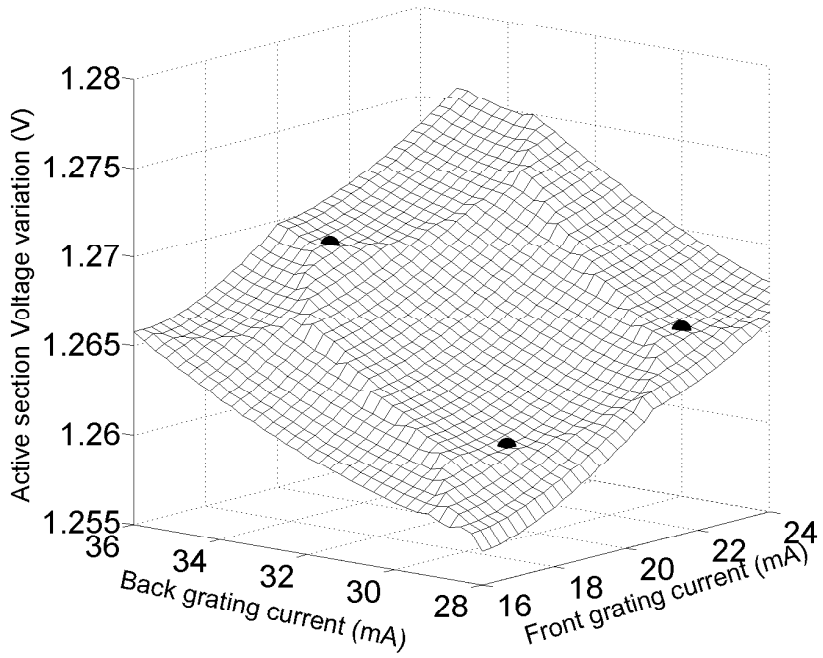

Figure 4.8: Voltage across the active section of the SG-DBR laser and the minimum points inside each longitudinal mode (black dots).

Figure 4.7 shows the tuning map of the SMSR and the linewidth of a single longitudinal

mode as a function of front and back grating currents. From Figure 4.7a, it is evident that the optimum point of SMSR is located in the centre of the mode, where a longitudinal mode is perfectly aligned with the reflection peaks of the two sampled gratings [14]. In an ideal loss-less case, this point is correlated with the local minimum of the voltage across the gain section [14, 15], which means the minimal threshold carrier density or gain in the active region [16]. However, due to the carrier-induced loss, this minimum is shifted to lower front and back currents and is no longer correlated with the minimum SMSR. As the Schawlow-Townes-Henry linewidth of the SG-DBR laser has been shown to correlate with the threshold gain [13], the minimum voltage across the gain section can be used to locate the optimum point of lowest linewidth. It is demonstrated in Figure 4.7b that the operating point with the lowest linewidth is located around the left bottom edge of the mode, which is in accordance with the shift of the voltage minimum of the same mode as shown in Figure 4.8. The linewidth at this point (see the filled circle in Figure 4.7b) is 10.33 MHz, which is 7 MHz lower than linewidth of the operating point with the highest SMSR (see the filled circle in Figure 4.7a). The SMSR of these two points are both above 39 dB. Although the operating optimum points of the linewidth are close to the mode boundaries, the wavelength hysteresis has been found to be negligible ($< 0.1\ \mathrm{mA}$) in the calibrations. Additional signal processing algorithm will be required to set these points further away from the mode boundaries for devices which have a strong hysteresis at high power levels.

For optical transmission networks employing OOK, the SMSR is the main criterion when choosing the operating points of SG-DBR lasers. As systems move towards advanced modulation formats, the linewidth of the laser increases in importance. As a result, it is necessary to find a calibration method that offers good SMSR along with narrow linewidth.

4.2.3 Linewidth Calibration Technique

Wavelength calibration is time consuming, and it has been stated that the measurements of all combinations of input currents used to obtain 100 ITU channels, could take up to one week to complete [17]. However, each device is sufficiently different to require a full calibration and data from a different laser will not suffice [18].

Different methods have been proposed to realize fast generation of the lookup table for SG-DBR lasers. A linear optical filter can be used to discriminate the wavelength variation into output power variation, which can be quickly measured and recorded [17]. Data processing techniques can then be applied to find the mode boundaries and the stable operating points [18]. An alternative method involves monitoring the in-phase modulation components on the front and back grating of a superstructure-grating distributed Bragg reflector (SSG-DBR) [15]. A trial function is calculated from the two components used for wavelength locking in order to locate the voltage minimum in the ($\mathrm{I_{front}}$, $\mathrm{I_{rear}}$) plane.

Both of the these methods are aimed at finding the operating points located in the centre of each longitudinal mode where the two reflective peaks of the front and back grating are aligned with a longitudinal mode, which means that the highest SMSR is achieved [14]. However, as shown in the previous section, the optimum linewidth of distributed Bragg reflector (DBR) lasers is not correlated with the peak SMSR but the voltage minimum. This single measurement of the active voltage as a function of the front and back grating currents combined with simple data processing allows us gather all the information required to choose the subset of operating points that will then be characterized in greater detail. This voltage versus ($\mathrm{I_{front}}$, $\mathrm{I_{rear}}$)-plane is defined as V1. The minimum voltage point of each mode shown by the dots in V1 corresponds to the circles in Figure 4.7b and represents the operating point with the minimal linewidth.

In Figure 4.8, the mode boundaries are blurred by a gradually increasing trend in the voltage with respect to the increased current on the front and back grating which may be caused by the carrier-induced loss and the leakage current from the other sections. In order to sharpen the mode boundaries, a low pass digital filter is applied to V1 and we define this new plane after filtering as V2. By subtracting V2 from V1, a plane with sharpened mode boundaries is obtained, which is defined as V3. Figure 4.9a shows V3 with an extended tuning range of 0-40 mA on the front grating and 0-35 mA on the back grating. The boundaries of each mode have been sharpened while the fluctuation inside each mode has been flattened. Hence, V3 can then be used to do edge detection and labelling of different modes in the same way as described in [18].

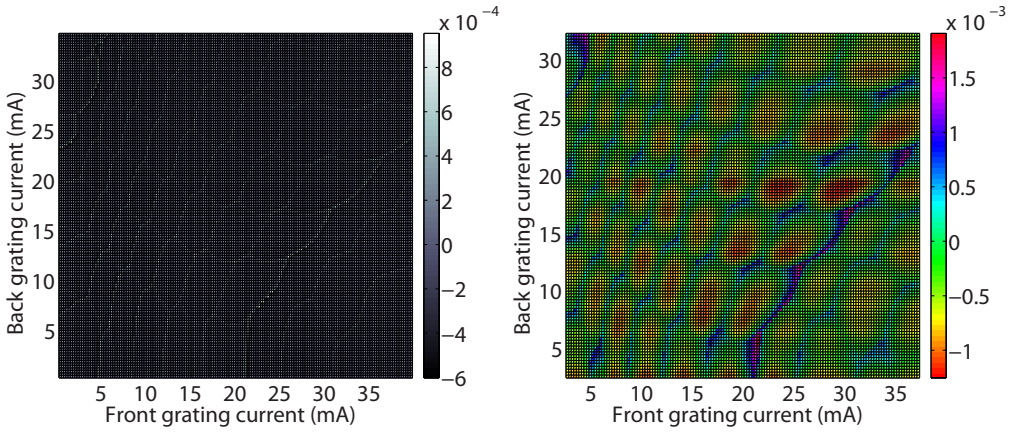

Figure 4.9: (a) Signal plane V3 with sharpened mode boundaries. (b) Signal plane V5 after removing the gradually varying trend.

In order to correct the voltage value for the carrier-induced losses and match the local minimum with the operating points with highest SMSR, an average filter is applied to V1. The filtered plane is defined as V4, which corresponds to the steadily increasing slope shown in Figure 4.8. The plane after subtracting V4 from V1 is defined as V5 (Figure 4.9b). The minimum points are now located in the centre of each mode and these points coincide with the operating points with high SMSR (see Figure 4.7a).

After selecting the operating points for a specific phase current (0 mA for the results above), a new phase current is then applied and a new group of operating points can be chosen. Finally, the wavelength and linewidth of these "suitable" operating points will be characterized in greater detail and compared with ITU wavelength specifications. Operating points which match ITU wavelengths and offer the lowest linewidth will be stored along with the currents [15, 17]. If output power control is desired these steps above can be repeated for different gain currents.

Two commercial SG-DBR lasers are calibrated by using our technique. Each section of the SG-DBR laser is independently driven, and a high resolution voltmeter is used to measure the voltage across the active section. Using the method above on the first SG-DBR laser, the operating points of 60 different longitudinal modes are found within a 140×160 grid of points, corresponding to a variation in current of 40 mA on the front grating and

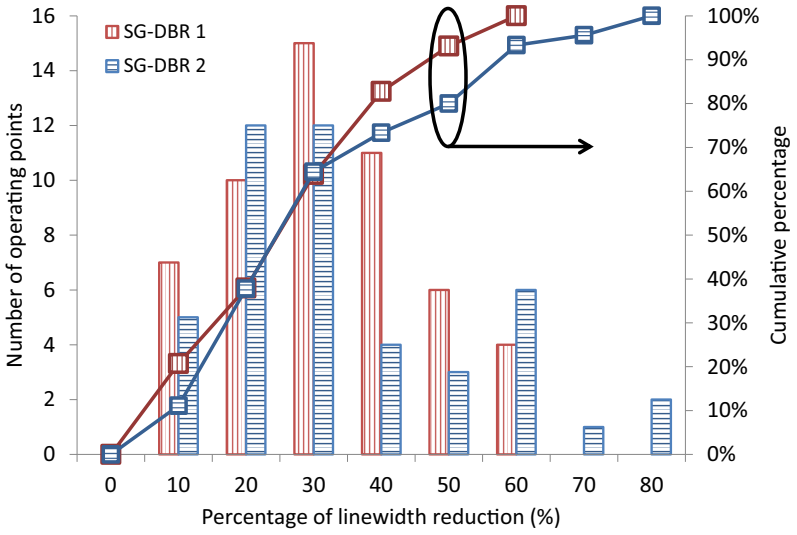

Figure 4.10: Histogram of linewidth reduction between the operating points with highest SMSR and narrowest linewidth.

35 mA on the back grating with a 0.25 mA step. The speed of the measurement can be greatly increased by using a data acquisition (DAQ) card, where a 400×400 grid of points can be taken in 1 minute [17]. Operating points chosen for optimum linewidth are located by using the voltage (I_{front}, I_{rear})-plane (V1) directly, while operating points with optimum SMSR are chosen by using the signal plane V5. The histogram of the reduction in linewidth between these two types of operating points is plotted in Figure 4.10. Linewidth reductions of up to 60 % are observed for this laser. For the second SG-DBR laser, with an integrated semiconductor optical amplifier (SOA), the gain section is biased at 80 mA while the SOA is biased at 90 mA. Forty different longitudinal modes are found in a 120×100 grid of points. The histogram of linewidth reduction of the second SG-DBR laser is also shown in Figure 4.10. Similar reductions can be observed between these two devices and the linewidth reduction of the second device can be up to 80 %. This reduction in linewidth can result in significant improvement in system performance when these devices are used in phase shift keying systems. It should also be noted that the SMSR of the operating points of the two SG-DBRs lasers with reduced linewidths are above 37dB and 30dB respectively.

4.3 Dynamic linewidth and Time-resolved BER

In the previous section, it is seen that the linewidth of SG-DBR lasers is becoming increasingly significant when the lasers are employed in coherent communication systems using advanced modulation formats. Since current controlled tunable lasers such as SG-DBR lasers are a key component in future fast switching coherent networks, it is necessary to characterize the time required for the phase noise of the laser to stabilize sufficiently after a switching event. However, the transformation of the phase noise from the time domain to the frequency domain (required to facilitate the measurement of the FWHM of the spectrum) makes it complicated to extract the linewidth dynamics during wavelength switching [19]. In this section, a new linewidth characterization method will be proposed. The phase noise of the laser can be derived using an optical quadrature front end. As the instantaneous phase of the laser is recorded in the time domain, the transient variation of the linewidth during switching can be calculated by dividing the captured time domain signal into short gating windows at different times during the switching interval.

4.3.1 Linewidth Characterization Using an Optical Quadrature Frontend

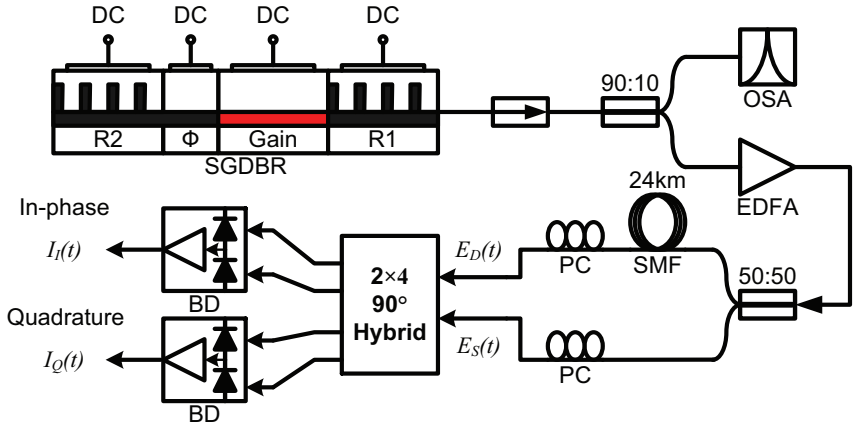

Figure 4.11: Setup of the linewidth characterization using a delayed self-homodyne technique with an optical quadrature front end.

The setup diagram of the proposed linewidth characterization method is shown in Figure 4.11. In contrast with the conventional delayed self-homodyne (DSH) technique, the

optical field, $E_S(t)$, and the delayed replica, $E_D(t)$, do not interfere directly on the photodetector [12]. The two optical fields defined as:

$$E_S(t) = \sqrt{P_S} \cdot e^{j(\omega_S t + \phi_S)} \cdot e^{j\phi_{n_S}(t)} \cdot \mathbf{e}_S \tag{4.15}$$

$$E_D(t) = \sqrt{P_D} \cdot e^{j(\omega_D t + \phi_D)} \cdot e^{j\phi_{n_D}(t)} \cdot \mathbf{e}_D \tag{4.16}$$

are superposed in a 2×4 90 ° hybrid whose output signals are detected by two balanced detector (BD). $E_S(t) + E_D(t) \exp[j\left(\frac{\pi}{2}n\right)]$, with n=0,1,2,3, represents the four outputs from the 90° hybrid. P_S and P_D represent the continuous wave (CW) powers, ω_S and ω_D are the angular frequencies, ϕ_S and ϕ_D are the initial phases, ϕ_{n_S} and ϕ_{n_D} are the phase noise and $\mathbf{e}_S$ and $\mathbf{e}_D$ represent the polarization unit vectors of the two optical fields. A micro-optics-based dual polarization coherent mixer is used in our experiment with two polarization controllers (PCs) to maximize $\mathbf{e}_S \cdot \mathbf{e}_D$. After detecting the output fields with the upper and lower BD, the in-phase and quadrature photocurrents are obtained as:

$$I_I(t) = R\sqrt{P_S P_D} \cos[\Delta\omega t + \phi_n(t) + \phi_0]\mathbf{e}_S\mathbf{e}_D + i_{sh_I} \tag{4.17}$$

$$I_Q(t) = R\sqrt{P_S P_D} \sin[\Delta\omega t + \phi_n(t) + \phi_0]\mathbf{e}_S\mathbf{e}_D + i_{sh_Q} \tag{4.18}$$

where, i_{sh_I} and i_{sh_Q} represent the overall shot-noise photocurrents in the in-phase and quadrature arms respectively [2]. The angular frequency offset $\Delta\omega$, the overall laser phase noise, $\phi_n(t)$, and the initial phase offset, $\phi_0(t)$, are defined as

$$\Delta\omega = \omega_S - \omega_D, \quad \phi_n(t) = \phi_{n_S}(t) - \phi_{n_D}(t), \quad \phi_0 = \phi_S - \phi_D. \tag{4.19}$$

Considering the actual phase evolution of the laser as random walk, the random phase change within a time interval, τ, is defined as:

$$\Delta\phi_n(t) = \phi_n t - \phi_n(t - \tau). \tag{4.20}$$

If a white frequency noise with a constant spectral density is assumed, according to equations (4.10) and (4.12), the variance of the phase change, $\Delta\phi_n$, is given as:

$$\langle \Delta\phi_n^2(\tau) \rangle = 2\pi\Delta\nu_{eff}|\tau|. \tag{4.21}$$

The beat-linewidth, $\Delta\nu_{eff}$, is given by the sum of the linewidth of the laser and the delayed replica. Since the delay of the 24 km SMF is approximately 120 μs, which is much longer than the coherence time of the laser, the two optical signals, $E_S(t)$ and $E_D(t)$, can be assumed to be decorrelated. Therefore the beat-linewidth:

$$\Delta\nu_{eff} = \Delta\nu_S + \Delta\nu_D = 2\Delta\nu, \tag{4.22}$$

where, $\Delta\nu$ is the linewidth of the laser.

In order to employ the processing methods above, the in phase and quadrature signals, $I_I(t)$ and $I_Q(t)$, are sampled and recorded by using a high speed A/D converter, which is a 10 GHz bandwidth real time oscilloscope in the experiment. Subsequently, the instantaneous phase and the linewidth of the laser can be derived by using equations (4.19) to (4.22). It should be noted that an EDFA is used to increase the amplitude of the signals in order to mitigate the effect of the shot-noise.

4.3.2 Static Linewidth

The linewidths at different emission powers of the same SG-DBR laser from JDSU and a distributed-feedback (DFB) laser from ILX are derived by using the method described above. The back section of the SG-DBR laser is biased at 53.6 mA while the phase and front section are left unbiased. The time interval, τ, in this calculation is chosen to be the reciprocal of the sample rate, which is set at 20 G samples per second (GS/s). A total number of 200,223 samples per sweep are recorded for the calculation and this corresponds to a frequency resolution of $\sim$ 100kHz, which imposes a resolution limit on the measured linewidths. After the time averaging in equation (4.21), the errors between successive sweeps are found to be less than 10%. The derived linewidths of the two devices

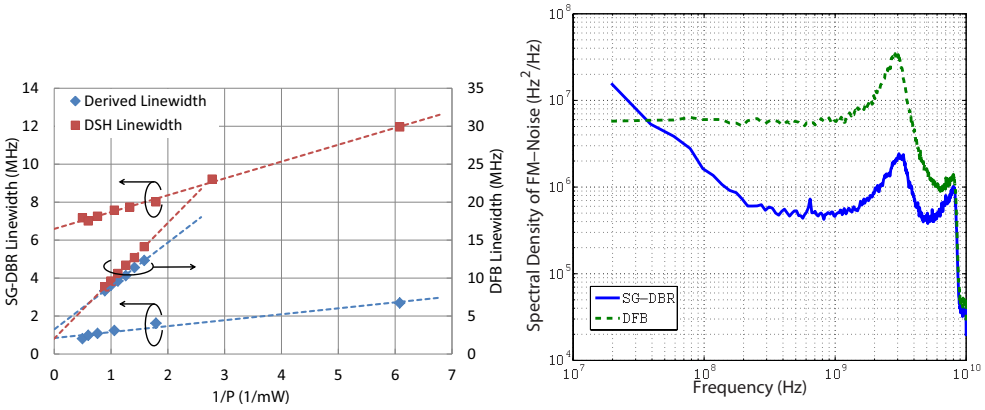

(a) (b)

Figure 4.12: (a) Derived linewidths (♦) using this method and the DSH linewidth (■) of an SG-DBR laser (left) and a DFB laser (right) as a function of 1/power. (b) FM-noise spectrum measured at P=1 mW.

with different output powers are shown in Figure 4.12a. The bias current on the two devices varied from threshold current (I_{th}) to roughly $2 \times I_{th}$. These linewidths are compared to the linewidths measured using the DSH method (referred to as DSH linewidth). There is a good agreement between the derived and DSH linewidth of the DFB laser, but there is a large difference between the two linewidths of the SG-DBR laser. The reason for this discrepancy can be explained by plotting the PSD (see Figure 4.12b) of the FM-noise derived using equation (4.20). The SG-DBR possesses considerable 1/f noise powers with frequency components up to approximately 200 MHz, due to the 1/f carrier noise and injection-recombination shot noise as described in Section 4.1.2 [6]. It is shown in Section 4.2.2 that in the presence of appreciable 1/f noise, the DSH measurement will overestimate the true Lorentzian-shaped optical linewidth, compared to our derived results which are sampled at a rate much higher than the 1/f noise component. In contrast, the FM-noise of the DFB laser exhibits a constant spectral density out to the relaxation oscillation frequency (or the absence of an appreciable 1/f noise component). In high speed optical transmission systems, white FM noise is more detrimental to the system performance than 1/f noise [20]. Hence, only how quickly the white noise settles down in the dynamic wavelength switching experiments will be considered and investigated further in Section 4.3.3. There is also an

underestimation of the linewidth obtained by our method at low optical powers, attributed to the fixed value of τ at the sample interval. This can result in a deviation from the linear relationship in equation (4.21) [3]. Correction for this nonlinear relationship can be achieved by taking a second measurement at a lower sampling rate.

4.3.3 Dynamic Linewidth

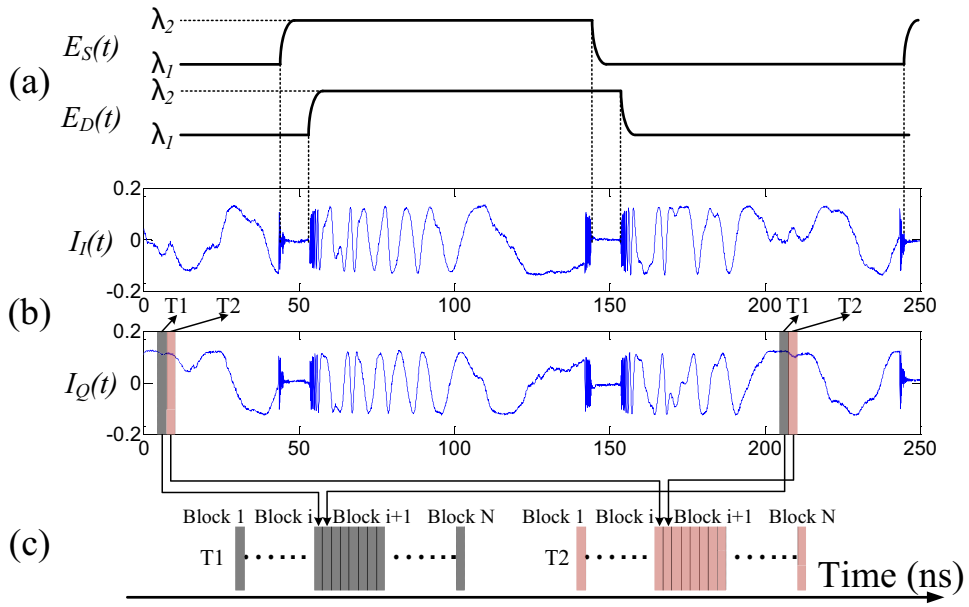

Figure 4.13: (a) Wavelength variation during the switching of the signal and the delayed replica. (b) Measured in phase and quadrature photocurrent. (c) Schematic illustration of dynamic linewidth measurement.

As the phase noise is estimated in the time domain, it is feasible to examine the phase noise variation during the wavelength switching of the SG-DBR laser. Four supermodes denoted as $\lambda 1$ to $\lambda 4$ are accessed by driving the back grating section with a current from 66 mA to 29.6 mA. The corresponding wavelengths of these four modes are 1547.3 nm, 1553.49 nm, 1560.03 nm and 1566.74 nm respectively. The lasing wavelength decreases as the current on the back grating increases due to the Vernier effect. By driving the back grating section of the laser with a square wave with variable low and high levels, the laser

can be switched between the four supermodes. The frequency of the square wave is set to be 5 MHz with a rise time of less than 100 ps.

Figure 4.13a illustrates the wavelength-time relationship between the signal and the delayed replica. Due to the bandwidth limitation of the system, imposed by the bandwidth of the oscilloscope in this experiment, only beat signals with frequency components ($\Delta\omega$) less than 10 GHz can be recorded [21]. It can be seen in Figure 4.13b, that the frequency of the beat signal decreases as the laser stabilizes to its final wavelength. As the signal $E_S(t)$ settles to its target wavelength earlier than the signal $E_D(t)$, $E_S(t)$ works as a local oscillator in this delayed homodyne system, where $\Delta\nu_S$ is a constant stable value and $\Delta\nu_D$ is derived as the dynamic linewidth of the laser using equation (4.22).

After the instantaneous phase of the laser is derived from the in-phase and quadrature components, the dynamic phase noise characteristics of the laser can be estimated by dividing the signal into a number of short gating windows (1 ns). These gate windows are applied at the same position (T1) of each period, and then the resultant gated signals, or blocks (see Figure 4.13c), are assembled together. The random phase change $\Delta\phi_n$ is calculated within each block, and the variance of $\Delta\phi_n$ is computed for all the blocks at the same position. Then the gate windows are moved to the next position (T2) with a step of 1 ns. A total number of 300 sweeps with 50 periods in each sweep are captured and processed. This averaging reduced the noise level. In practice it is possible to measure without averaging, but this will reduce the temporal resolution in the dynamic linewidth curve.

The linewidth dynamics of two switching combinations of the SG-DBR laser are investigated using this method. The results including both forward and backward switching are shown in Figure 4.14. The start point of the time scale (0 ns) is chosen to be when the laser settled within ± 0.5 GHz of its destination frequency (required for dense wavelength division multiplexing systems). The linewidth switching time is defined as the time taken for the linewidth to reduce to 110% of its final static value from the start point. It corresponds to approximately 20 ns switching time when the laser is switched between two adjacent supermodes ($\lambda 1$ and $\lambda 2$). This switching time increases to approximately 35 ns when the laser is switched from $\lambda 4$ to $\lambda 1$ and the linewidth is found to still be fluctuating after 45 ns

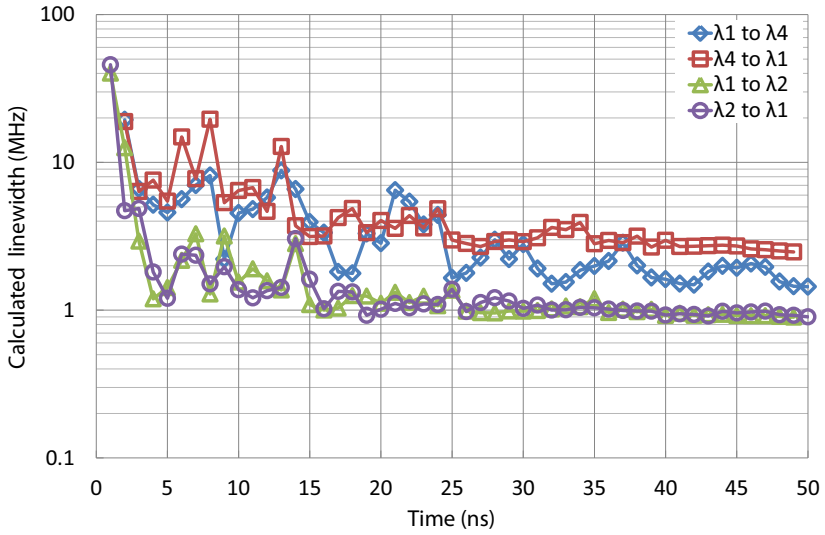

Figure 4.14: Dynamic linewidth of two different switching combinations.

from the start for the backward switching from $\lambda 1$ to $\lambda 4$. This is mainly due to the lasing of the intermediate modes ($\lambda 2$ and $\lambda 3$) during the switching which increases the wavelength switching time.

4.3.4 Time Resolved BER

As proved in Section 4.3.3, the linewidth of SG-DBR lasers requires a few tens of nanoseconds to reach its steady state value. For this reason, it is worthwhile to examine the effect of the linewidth dynamics in a packet switching scenario with phase modulation formats. In this section, the time resolved BER in a 10.7 Gbaud DQPSK packet transmission system is measured by switching the SG-DBR between two supermodes at wavelengths $\lambda 1$ and $\lambda 2$ as denoted in Section 4.3.3.

The experimental setup is shown in Figure 4.15. The output of the clock generator is split to trigger the oscilloscope and a digital delay pulse generator (PG) from Stanford Research Systems. The timing diagram of the output of the switching signal and the gate pulse is shown in the inset of Figure 4.15. The frequency of the square wave is 10 MHz which corresponds to a switching period of 100 ns ($\mathrm{T_S} = 50\mathrm{ns}$). The time delay ($\mathrm{T_D}$) between the falling edge of the gate pulse and the rising edge of the square wave is programmable

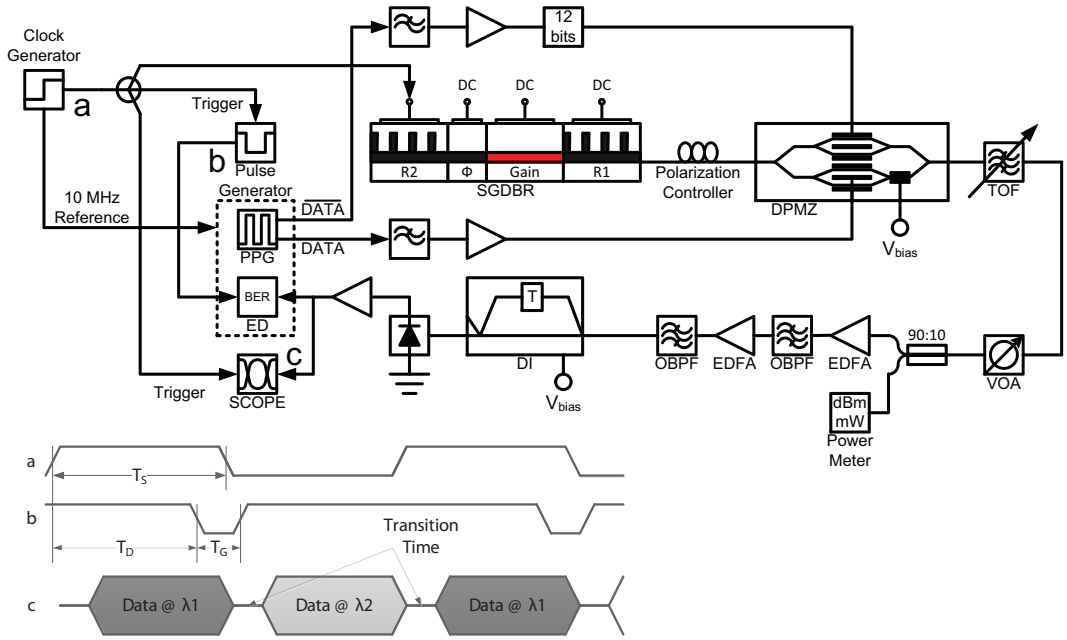

Figure 4.15: Experimental setup of time resolved BER measurement. The inset shows the timing diagram at points a, b and c.

from 0 up to $2T_S$ with a resolution of less than 10 ps. The gate pulse is then applied to the error detector (ED) of an Anritsu signal quality analyser. By running the ED in burst mode, only errors inside the gating window are captured and computed. In the experiment, the gate pulse width, T_G, is set to equal 2 ns and T_D is swept from 0 to 100 ns with a 100 ps step.

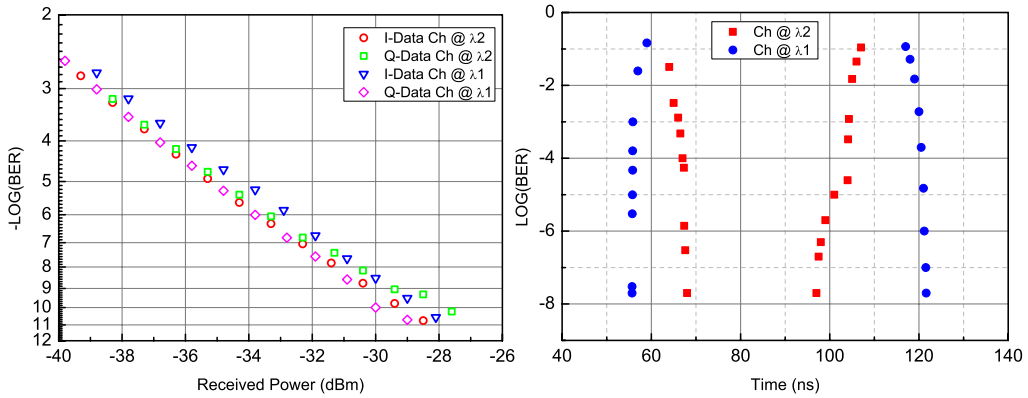

(a) (b)

Figure 4.16: (a) BER vs received power in static scenario, (b) time resolved BER in switching scenario.

An in-phase and quadrature (IQ) modulator is driven by two complementary data outputs from a PPG running a PRBS with a pattern length of $2^{15} - 1$. A delay of 12 bits is introduced in one arm of the IQ modulator in order to decorrelate the streams such that they represent independent in-phase and quadrature components of the data stream. A 10.7 Gb/s one bit Mach-Zehnder delay interferometer (MZDI) is implemented at the receiver side to differentially demodulate the in-phase or quadrature data independently. The static BER is measured separately for the I and Q components of the received signal at each wavelength as shown in Figure 4.16a. Receiver sensitivities of between -29dBm and -30dBm at a BER of 1×10^{-9} are observed for I and Q on each wavelength channel.

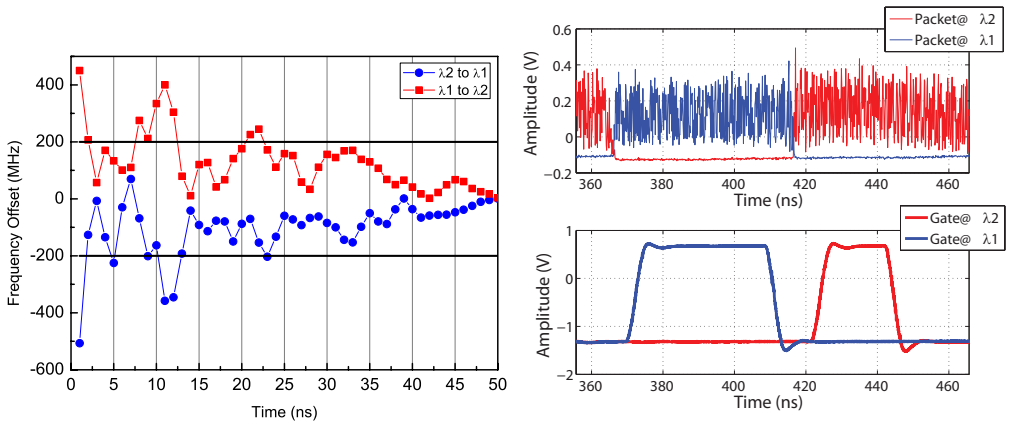

(a) (b)

Figure 4.17: (a) Frequency offset. (b) Measured data packets and maximum error free gating pulses.

Figure 4.16b shows the measured time resolved BER of the two packets. It can be observed that the time required to switch from $\lambda 1$ to $\lambda 2$ and obtain error free transmission at this wavelength is approximately 12 ns while it takes approximately 24 ns to switch back to $\lambda 1$. It should be noted that the linewidth required for a 10.7 Gbaud DQPSK to operate with a < 1 dB penalty at the BER equal to 10^{-4} is approximately 50 MHz (see Section 2.2.4). However, as shown in Figure 4.14, soon after the frequency of the laser is settled within ± 0.5 GHz of its destination frequency, the linewidth of the laser is less than 50 MHz, which is low enough to support 10.7 Gbaud DQPSK transmission. The reason that the switching time obtained from the time resolved BER is longer than linewidth dynamics

is due to the frequency detuning of the MZDI. As mentioned in Section 2.2.4, the maximum tolerable detuning of the interferometers maybe as low as 200 MHz at 20 Gb/s DQPSK systems [22]. The frequency offset can be derived from time averaging of the instantaneous frequency [3]. In turn, the instantaneous frequency is calculated from the derivative of the instantaneous phase of the in-phase and quadrature components [23]. Figure 4.17a shows the frequency offset calculated from the switching between $\lambda 1$ and $\lambda 2$ with the same time scale as in Figure 4.14. A settling time of 25 ns is required for the frequency offset to be less than 200 MHz, which agrees with the time resolved BER measurements. Figure 4.17b shows the oscilloscope traces of the measured data packets and the corresponding maximum error free gating pulses [24], which indicates a guard band of 20 ns is required. The shorter gating pulse of the data packet of $\lambda 2$ is attributed to the longer frequency setting time of this mode, crucial for phase modulated formats. The length of the two maximum error free gating pulses also agree with the time resolved BER measurement shown in Figure 4.16b.

4.4 Summary

In this chapter, the origins of the semiconductor laser phase noise is investigated. The spontaneous emission introduces random phase and intensity fluctuations. The intensity fluctuations subsequently produce a delayed phase shift because of the coupling between the imaginary and the real parts of the refractive index. For frequencies which are much less than the relaxation frequency, the FM-noise spectrum can be considered as a white noise spectrum, corresponding to a Lorentzian lineshape. However, for wavelength tunable semiconductor lasers integrated with passive tuning sections, they exhibit different types of additional FM noise such as the IRSN and 1/f noise. The additional noise causes significantly broadening of the linewidth measured by using the standard delayed self-heterodyne technique and also change the lineshape from a Lorentzian to a Voigt function. However white frequency noise is more crucial in high speed coherent systems. The linewidth measured by the self-heterodyne are deduced from the -10 dB width of the lineshape to reduce the effect of the additional low frequency FM-noise.

By using the delayed self-heterodyne method, the linewidth of the SG-DBR lasers is examined. The results of a DPSK transmission system with different values of linewidth show the importance of using the laser linewidth as a calibration parameter, when selecting operating points for the SG-DBR lasers in coherent systems. The linewidth of the lasers is found to be correlated with the active voltage and not the SMSR, which enables a fast calibration method for SG-DBR lasers based on the voltage versus the front and back grating current measurement combined with data processing. Two SG-DBR lasers are calibrated by using this method. A linewidth reduction of up to 80% is observed between the calibration methods that aim for highest SMSR and lowest linewidth.

While the SG-DBR laser is used in fast switching coherent networks, the linewidth dynamics of the laser during the switching become increasingly important, especially for systems that employ higher order modulation formats. However, the transformation of the phase noise from the time domain to the frequency domain makes it complicated to extract the linewidth dynamics during wavelength switching. A DSH method using an optical quadrature front end is presented. Static measurements validate this method of calculating the white FM-noise linewidth, which is more important in high speed transmission system. The advantage of this method is that the phase noise of the laser is derived in the time domain and can be sampled and processed offline, which enables the examination of the linewidth dynamics of the signal at a specific time during the switching. The linewidth switching time of a commercial SG-DBR laser is found to be within tens of nanoseconds range. A time resolved BER measurement shows the importance of the frequency offset in fast packet switching networks with self-coherent receivers. This characterization technique, including both the phase noise and frequency dynamics, offers 1 ns time resolution and 17 kHz frequency resolution which is the best achievable for laser phase noise measurements to the best of our knowledge [19, 23]. Therefore it could be important for the development and optimization of future fast reconfigurable photonic systems that utilise advanced modulation format transmission.

References

[1] C. Henry, "Theory of the linewidth of semiconductor lasers," *IEEE Journal of Quantum Electronics*, vol. 18, no. 2, pp. 259– 264, Feb. 1982.

[2] M. Seimetz, *High-order modulation for optical fiber transmission*. Dordrecht, New York: Springer, 2009.

[3] K. Petermann, *Laser diode modulation and noise*. Dordrecht ;;Boston ;Tokyo ;Norwell MA: Kluwer Academic Publishers ;;KTK Scientific Publishers ;;Sold and distributed in the U.S.A. and Canada by Kluwer Academic Publishers, 1991.

[4] L. B. Mercer, "1/f frequency noise effects on self-heterodyne linewidth measurements," *Journal of Lightwave Technology*, vol. 9, no. 4, pp. 485–493, Apr. 1991.

[5] K. Kikuchi and K. Igarashi, "Characterization of semiconductor-laser phase noise with digital coherent receivers," in *Optical Fiber Communication Conference and Exposition (OFC/NFOEC), 2011 and the National Fiber Optic Engineers Conference*. IEEE, Mar. 2011, pp. 1–3.

[6] S. Nakagawa, G. Fish, A. Dahl, P. Koh, C. Schow, M. Mack, L. Wang, and R. Yu, "Phase noise of widely-tunable SG-DBR laser," in *Optical Fiber Communications Conference, 2003. OFC 2003*. IEEE, Mar. 2003, pp. 461– 462 vol.2.

[7] P. Signoret, M. Myara, J. P. Tourrenc, B. Orsal, M. H. Monier, J. Jacquet, P. Leboudec, and F. Marin, "Bragg section effects on linewidth and lineshape in 1.55-m DBR tunable laser diodes," *IEEE Photonics Technology Letters*, vol. 16, no. 6, pp. 1429–1431, Jun. 2004.

[8] J. Buus, M. Amann, and D. J. Blumenthal, *Tunable Laser Diodes and Related Optical Sources*, 2nd ed. Wiley-IEEE Press, Feb. 2005.

[9] M. C. Amann and R. Schimpe, "Excess linewidth broadening in wavelength-tunable laser diodes," *Electronics Letters*, vol. 26, no. 5, pp. 279–280, Mar. 1990.

[10] M. C. Amann, R. Hakimi, B. Borchert, and S. Illek, "Linewidth broadening by 1/f noise in wavelength-tunable laser diodes," *Applied Physics Letters*, vol. 70, no. 12, pp. 1512–1514, Mar. 1997.

[11] R. Hui and M. O'Sullivan, *Fiber optic measurement techniques*. Amsterdam ;;London :: Elsevier/Academic Press,, 2009.

[12] D. Derickson, *Fiber optic test and measurement*. Upper Saddle River N.J.: Prentice Hall PTR, 1998.

[13] K. Shi, F. Smyth, P. M. Anandarajah, D. Reid, Y. Yu, and L. P. Barry, "Linewidth of SG-DBR laser and its effect on DPSK transmission," *Optics Communications*, vol. 283, no. 24, pp. 5040–5045, Dec. 2010.

[14] H. Ishii, F. Kano, Y. Yoshikuni, and H. Yasaka, "Mode stabilization method for superstructure-grating DBR lasers," *Lightwave Technology, Journal of*, vol. 16, no. 3, pp. 433–442, 1998.

[15] G. Sarlet, G. Morthier, and R. Baets, "Control of widely tunable SSG-DBR lasers for dense wavelength division multiplexing," *Lightwave Technology, Journal of*, vol. 18, no. 8, pp. 1128–1138, 2000.

[16] J. Carroll, *Distributed feedback semiconductor lasers*. London: The Institution of Electrical Engineers [etc.], 1998.

[17] J. Dunne, T. Farrell, and R. O'Dowd, "Fast generation of optimum operating points for tuneable SG DBR laser over 1535-1565 nm range," in *Lasers and Electro-Optics, 1999. CLEO '99. Summaries of Papers Presented at the Conference on*, 1999, pp. 147–148.

[18] T. Farrell, N. Ryan, J. Levins, and T. Mullane, "United states patent: 7436864 - method for optimising the calibration process of a tuneable laser," Oct. 2008.

[19] A. Mishra, A. Ellis, L. Barry, and T. Farrell, "Time-resolved linewidth measurements of a wavelength switched SG-DBR laser for optical packet switched networks," in *OFC/NFOEC 2008 - 2008 Conference on Optical Fiber Communication/National Fiber Optic Engineers Conference*, San Diego, CA, USA, Feb. 2008, pp. 1–3.

[20] K. Kikuchi, "Effect of 1/f-type FM noise on semiconductor-laser linewidth residual in high-power limit," *IEEE Journal of Quantum Electronics*, vol. 25, no. 4, pp. 684–688, Apr. 1989.

[21] H. Joseph and D. Sadot, "A novel Self-Heterodyne method for combined temporal and spectral High-Resolution measurement of wavelength transients in tunable lasers," *IEEE Photonics Technology Letters*, vol. 16, no. 8, pp. 1921–1923, Aug. 2004.

[22] G. Bosco and P. Poggiolini, "On the joint effect of receiver impairments on direct-detection DQPSK systems," *Journal of Lightwave Technology*, vol. 24, no. 3, pp. 1323–1333, Mar. 2006.

[23] R. Maher and B. Thomsen, "Dynamic linewidth measurement technique using digital intradyne coherent receivers," *Optics Express*, vol. 19, no. 26, p. B313, Nov. 2011.

[24] M. Kauer, M. Girault, J. Leuthold, J. Honthaas, O. Pellegri, C. Goullancourt, and M. Zirngibl, "16-channel digitally tunable external-cavity laser with nanosecond switching time," *IEEE Photonics Technology Letters*, vol. 15, no. 3, pp. 371–373, Mar. 2003.

Chapter 5

A Three-Section Tunable Slotted Fabry-Pérot Laser

In Chapter 4, sampled-grating distributed Bragg reflector (SG-DBR) lasers with wide tuning range, high side-mode suppression ratio (SMSR) and fast switching dynamics are demonstrated as an ideal candidate for systems that utilize fast wavelength provisioning, such as optical packet switching (OPS). While wide and accurate tunability is a significant advantage for many applications, these devices are complex to manufacture and they may suffer from broad optical linewidth [1] due to the additional FM-noise. The system performance could be degraded by this additional noise, especially for those operated at low baud rate or employing higher order modulation formats.

In the last few years a new type of monolithic tunable laser fabricated by etching periodic perturbing slots into the laser ridge has been presented and demonstrated by researchers [2]. These lasers have a single growth fabrication, which significantly reduces the cost and complexity of fabrication while increasing the yield. This type of laser structure, known as the slotted Fabry-Pérot (SFP) laser, offers wide (discrete) tunability, high SMSR and sub-nanosecond switching [3]. In this chapter, one such laser with two single slots which separates the laser into three sections will be presented. In contrast to SFP lasers with periodic perturbations within the sections [4], this device has no perturbations within each of the three sections. Like the single mode devices based on a similar structure [5], this

type of tunable SFP laser will be shown here to also exhibit narrow linewidth. The structure and operation of the tunable three-section SFP laser will be studied, followed by a detailed characterization of the laser, including both static parameters and wavelength switching dynamics. The linewidth advantages of the laser will be demonstrated by employing the laser in both static and dynamic self-coherent systems.

5.1 Characterization of the SFP Laser

In this section, the single mode lasing and wavelength tunability achieved by the three-section SFP laser will be investigated. Afterwards the static characterization which includes the optical spectra, relative intensity noise (RIN), SMSR and the linewidth will be presented. The wavelength switching dynamics of the laser for use as a low cost transmitter in dynamic networks will also be characterized.

5.1.1 Device Structure and Operation

The structure of the laser is shown in Figure 5.1. Two single slots are etched into the ridge waveguide to separate the 647 μm long laser into three independently injected active sections. The wafer material is a standard 5 quantum well (QW) off-the-shelf laser structure from a global wafer supplier (IQE), with no regrowth steps. The quaternary compound $\mathrm{Al_xGa_{1-x}In_yAs_{1-y}}$ is used where x is the Aluminium mole fraction and y is the Indium mole fraction. The thickness of the quantum wells is 0.06 μm and 0.01 μm. The slots are formed in the same etch step as the laser ridge, and do not go through the active region. However, the depth is sufficient to perturb the mode and cause a reflection at the slot position [6]. The device is mounted in a standard 14 pin butterfly package with integrated thermoelectric cooler (TEC), and an 11 μm radius lens ended fibre is aligned and welded into position.

Unlike distributed Bragg reflector (DBR)-type lasers, there are no slots or perturbations within any of the sections to act as gratings. The reflections from each of the two slots that define the sections result in three mutually coupled Fabry-Pérot (FP) cavities. The lasing

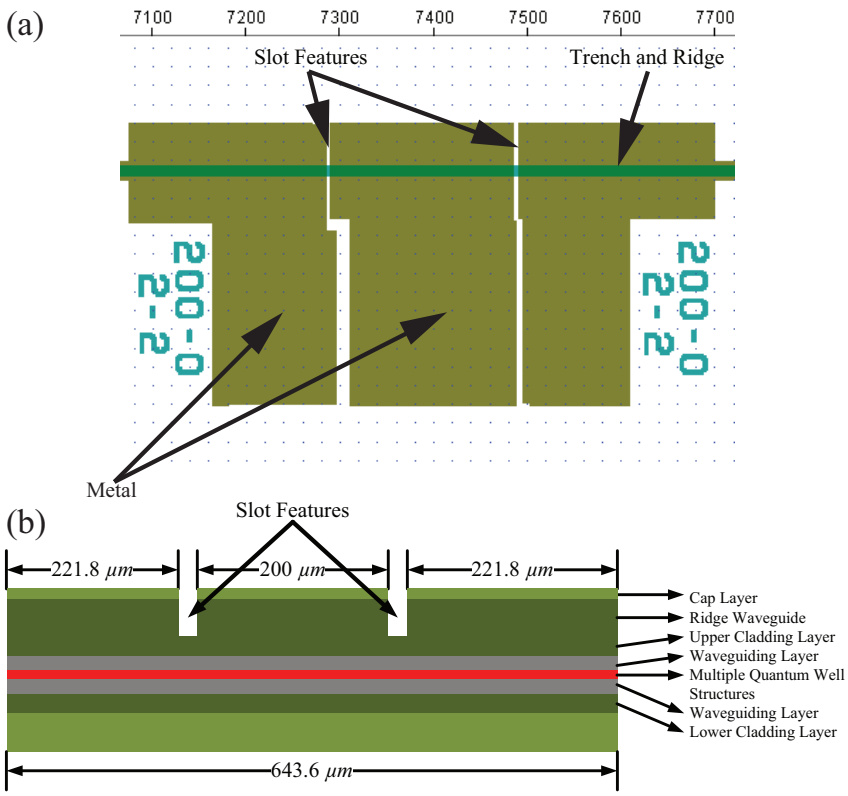

Figure 5.1: (a) Mask layout of the device. (b) Longitudinal structure of the three-section SFP laser.

wavelength is set by the overall gain and phase resonance conditions. These conditions can be adjusted by the current injected into each section, by which the local refractive index and gain is altered. The primary mode spacing is set by the overall length of the device (647 μm) with every third mode being preferentially selected due to the sectioning of the overall cavity. The feedback from the slots between the sections generates three sets of cavity modes which have mode spacings of approximately 200 GHz according to equation (3.6). Smaller mode spacing can be achieved by increasing the length of each section and vice versa.

For the packaged device, it is found that the mode spacing of the middle (200 μm) and the back (211 μm) sections is larger than that of the front section (236 μm), which can be attributed to the displacement of the cleave at the back facet over the intended position. Due to the Vernier effect only a single mode from the sets of cavity modes can be aligned. Unintended variations in the actual length of the sections results in a shift in the mode map

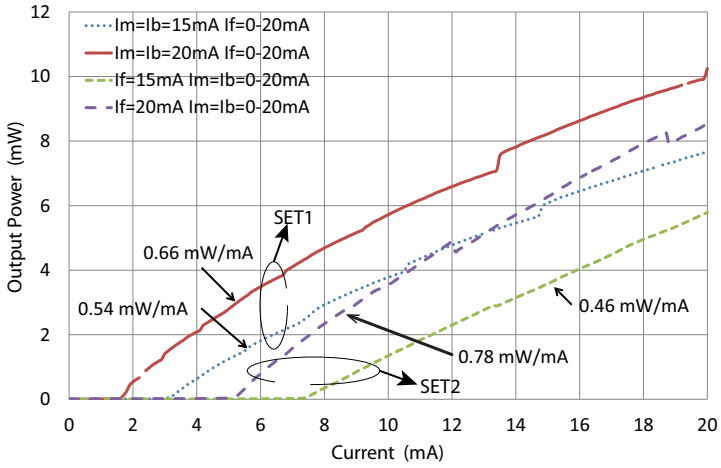

(a)

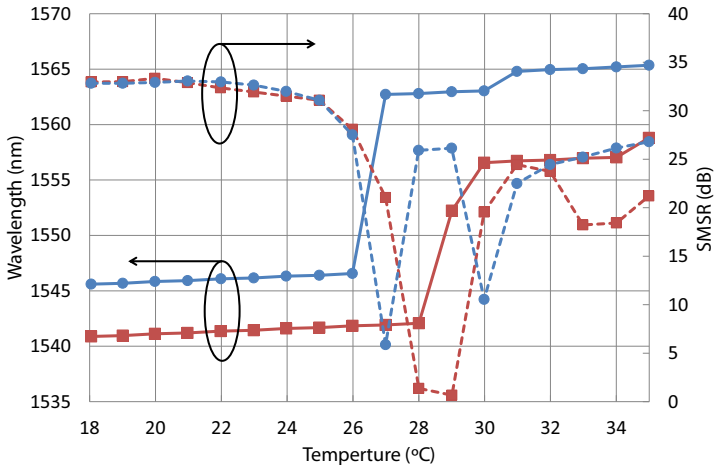

(b)

Figure 5.2: (a) Power versus current characteristic under different bias combinations. Ib, Im and If represent the current on the back, middle and front section respectively. (b) Temperature sensitivity of two different modes (■ and ●). The solid lines represent the lasing wavelength while the dotted lines represent the corresponding SMSR.

with current into the individual sections. This mode map is also dependent on the refractive indices of the individual sections which in turn are temperature dependent. Figure 5.2a shows the P-I curves of different bias combinations. The two sections (back and middle sections) with similar length were driven with the same conditions. From the figure we can see that the required current on the front section for threshold decreases with the increase of the bias on middle and back section, which means that the weakly clamped threshold carrier

density of the front section is decreased according to the increasing bias on the other two sections. The same phenomenon can also be observed for the total threshold current of the middle and back section with different bias on the front section. The figure also shows the slope efficiency of each P-I curve. The increase of the slope efficiency of two sets of curves in Figure 5.2a is also due to the decrease of the carrier density when the current on the other section/sections increases, which agrees with the additional optical loss caused by the carrier plasma effect as described by equation (3.13). According to the free carrier plasma effect, the refractive index is inversely proportional to the carrier density. The aligned lasing mode can be set to hop to another one by independently varying the current on the three sections. This can be seen from the kinks on the P-I curves in Figure 5.2a. Mode hops can also be generated by temperature variations. Therefore the laser chip is packaged with an integrated TEC. Figure 5.2b shows the temperature sensitivity of the device with two different lasing modes. From the figure we can see that single mode lasing (SMSR$>$30 dB) can be maintained within a range of 7 °C. The temperature dependence of wavelength is approximately 0.11 nm/°C for both modes. However multi-mode lasing can be observed when the temperature of the device exceeds 26 °C.

Therefore by varying the drive current to each section (0 to 60 mA), the gain and index of each section of the laser can be controlled. Figure 5.3 shows the wavelength and SMSR tuning curves as a function of the voltage applied to the front section (Figure 5.3a) and the total voltage applied to both the middle and the back section equally (Figure 5.3a). Similar to an SG-DBR laser using the Vernier effect, the tuning mechanism of the three-section SFP laser can be explained by using Figure 5.4. As illustrated above in Figure 5.2a, the increase of the bias on the middle and back section results in a decrease of the carrier density in the front section, which increases the refractive index according to the free-carrier plasma effect (see equation (3.12)). Consequently the cavity modes in the front section move towards higher wavelengths, which causes the aligned mode to hop to a higher wavelength as shown in Figure 5.3b. An increase of the bias on the front sections results in a increase of the refractive index in the back and middle sections, which moves the corresponding cavity modes in the back and middle section towards higher wavelengths.

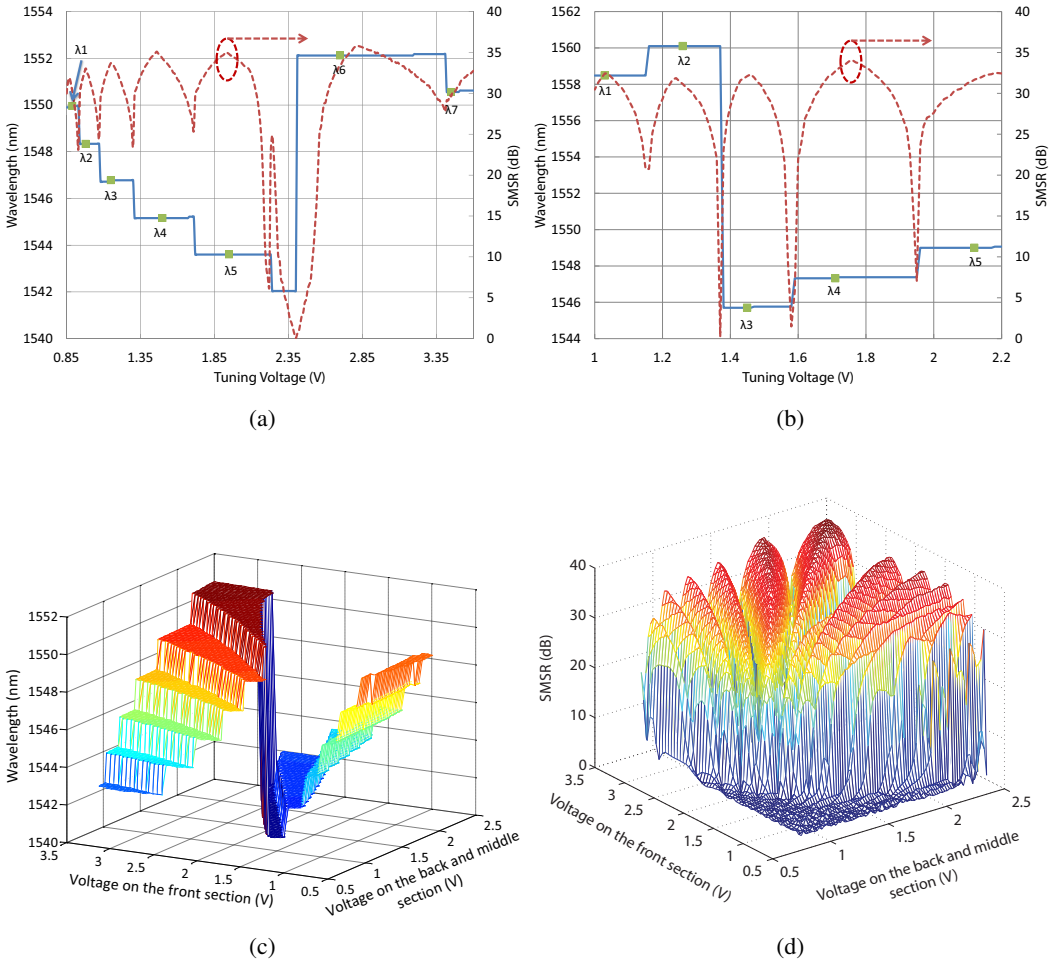

Figure 5.3: Wavelength (solid line) and corresponding SMSR (dotted line) tuning curves versus (a) voltage across the front section and (b) total voltage across both the middle and the back sections equally. The squares represent the chosen switching points. (c) 3D wavelength tuning map. (d) 3D SMSR tuning map.

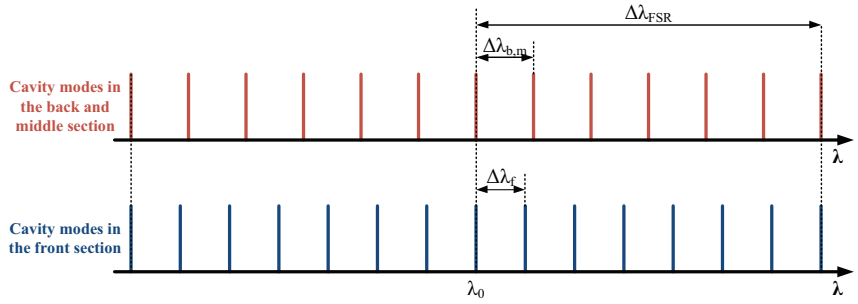

Figure 5.4: Schematic diagram illustrating the potential cavity modes inside different sections of the SFP laser.

Hence, the next aligned mode hops to a lower wavelength as shown in Figure 5.3a. The mode spacing in Figure 5.3a is 1.584 nm ($\Delta\lambda_{\mathrm{f}}$) while the mode spacing in Figure 5.3b is 1.62 nm ($\Delta\lambda_{\mathrm{b,m}}$). Figures 5.3c and 5.3d show the 3D wavelength and SMSR tuning maps. Continuous tuning of approximately 0.3 nm is achieved by tuning the voltage on the three sections simultaneously.

5.1.2 Device Characterization

The delayed self-heterodyne method is used to measure the linewidth of the SFP laser. Since no optical isolator is placed in the packaged device, which is different from the commercial SG-DBR lasers, external isolation is required to prevent optical feedback into the cavity. The setup is the same as used for the linewidth characterization of the SG-DBR laser shown in Figure 4.3a. The RIN measurements are taken using an 11 GHz photoreceiver with an integrated transimpedance amplifier (TIA). The output of the photoreceiver is split using a bias-tee with the DC component measured using a digital multimeter and the AC component measured using the electrical spectrum analyser (ESA).

Twenty five channels of the international telecommunication union (ITU) 100 GHz grid are found by applying tuning currents between 0 and 60 mA to each section of the SFP laser. The superimposed tuning spectra are shown in Figure 5.5a. A mode peak power variation of 7 dB across the channels is found. This is due to the active characteristic of the three tuning sections as both the carrier density and the photon density are changed according to the current changes. An integrated semiconductor optical amplifier (SOA) is desired to both increase and balance the output power of different wavelength channels [4]. The RIN spectra of the laser at six different channels are shown in Figure 5.5b. The averaged RIN within 200 MHz to 11 GHz frequency range was below -135 dB/Hz for the six measured channels. The output power of each of these channels is given in the legend of Figure 5.5b and as expected the higher power channels exhibit lower RIN.

Figure 5.6a shows the corresponding current on each section of the laser. As mentioned above, a power variation of 7 dB between the channels can be observed from this figure. The linewidth, calculated from the 20 dB spectral width ($2/\sqrt{99}$ times of the actual linewidth)

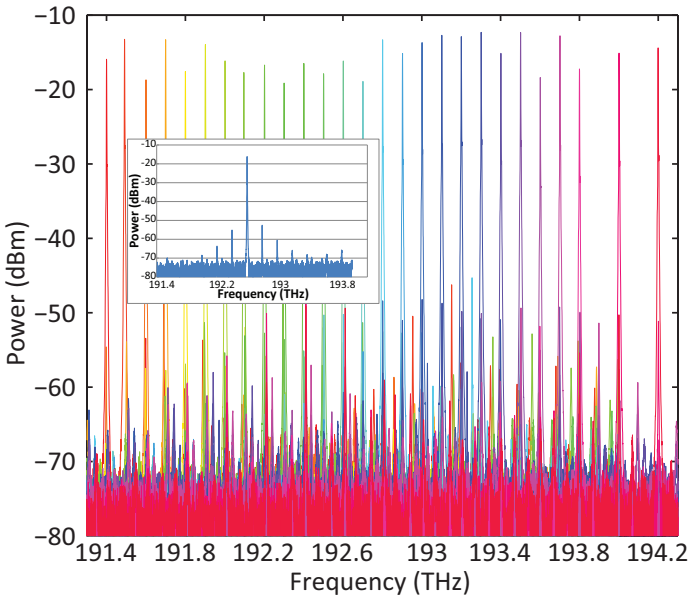

(a)

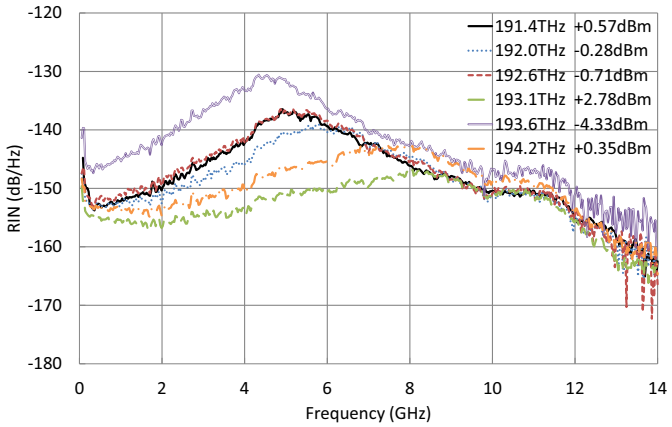

(b)

Figure 5.5: (a) Optical spectrum at different ITU channels. The inset shows the spectrum of the channel at 192.6 THz. (b) The RIN spectra of six ITU channels with different launch powers. Data is averaged over 20 sweeps.

averaged over 50 sweeps is shown in Figure 5.6a, along with the SMSR. The average value of linewidth is 538 kHz with a value below 800 kHz for all channels, and the SMSR of each channel is above 30 dB. The linewidth of the SFP laser, measured by the delayed self-heterodyne method, is found to be six times less than the linewidth of the SG-DBR lasers characterized by the same setup. This could be attributed to the fact that all the sections in the SFP lasers are active and additional phase noise described in Section 4.1.2

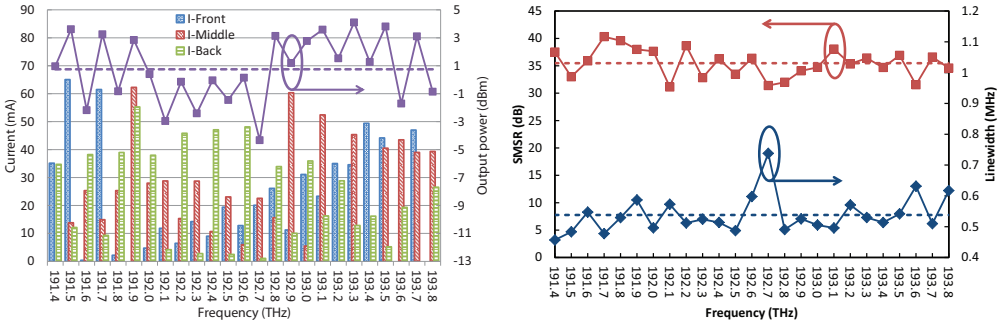

(a) (b)

Figure 5.6: (a) Drive currents on each section and the output power of different ITU channels. (b) Linewidth and SMSR at different ITU channels. The dotted lines show the average values.

is reduced due to the gain-clamping mechanism. Some other papers also show that the narrow linewidth characteristics of the single-mode SFP lasers are due to symmetric facet reflectivities and low α-factor comparing to single-mode distributed-feedback (DFB) lasers [5, 7].

5.2 Applications of SFP Lasers in Dynamic Coherent Networks

In this section, the SFP laser and the SG-DBR laser will be employed in the 1.25 Gb/s differential binary phase shift keying (DPSK) transmission system in order to show the narrow linewidth benefit of the SFP laser. The wavelength switching dynamics of the three-section SFP laser along with latency in a 10.7 Gbaud differential quadrature phase shift keying (DQPSK) packet transmission system will also be examined.

5.2.1 Static DPSK Transmission

Identical DC current sources (Thorlabs ITC 502) are used for both lasers. The worst measured linewidth of the SFP laser is approximately 738 kHz at channel 194.2 THz. The bias condition for this channel is 26.18 mA on the middle section, 34.87 mA on the back section and 10.15 mA on the front section. For the SG-DBR, the two operating points at the channel of 194.2 THz are chosen. Both exhibited SMSR greater than 45 dB but the linewidths

varied (as shown in Figure 4.3b) from 4.6 MHz to 19.8 MHz. Thus, the widest linewidth from the tunable SFP laser is over five times narrower than the narrowest linewidth channel of the SG-DBR laser.

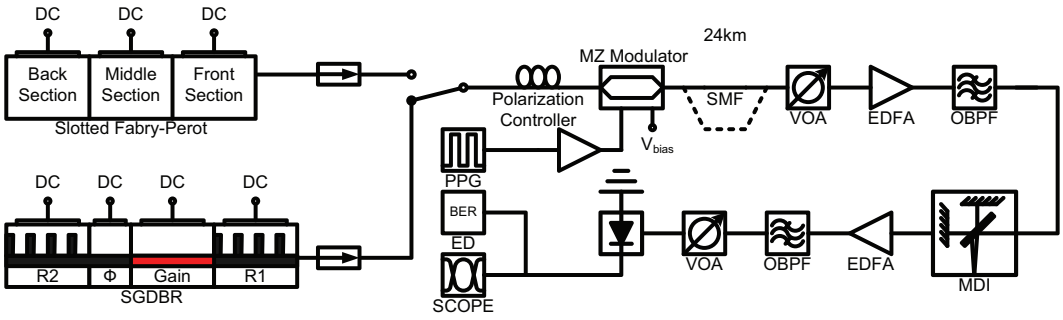

Figure 5.7: Experimental setup of the DPSK transmission system.

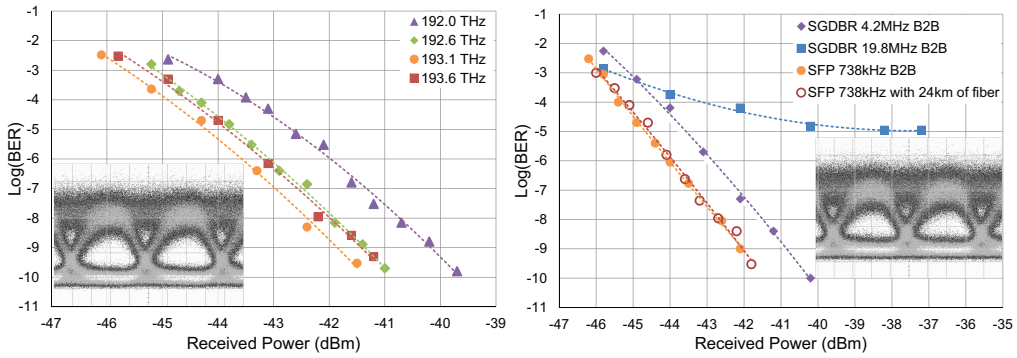

(a) (b)

Figure 5.8: BER of 1.25 Gb/s DPSK transmission using (a) the SFP laser at 4 ITU channels back to back, (b) the SG-DBR laser at 194.2 THz channel with 4.6 MHz and 19.8 MHz linewidth. The BER of 1.25 Gb/s DPSK transmission using the SFP laser at 194.2 THz without (●) and with (○) 24 km of fibre is also shown. The insets are the received eyes at power of -41.8 dBm for the (a) SFP laser and (b) the SG-DBR laser (19.8MHz).

The experimental setup is shown in Figure 5.7. Both lasers were butterfly packaged and optically isolated. The other parts of the setup are operated in identical conditions to Figure 4.4. The corresponding demodulated bit error rate (BER) is displayed in Figure 5.8. It is important to note that by using a balanced detector, a 3 dB improvement in sensitivity could have been obtained. Five channels of the SFP laser are chosen for the experiment with frequencies between 192.0 THz and 194.2 THz with approximately 0.5 THz spacing.

Error free performance is achieved with the SFP laser at each channel (see Figure 5.8) spread across the operating wavelengths of the device. The 192.0 THz channel suffers a performance penalty due to the reduction in the erbium-doped fibre amplifier (EDFA) gain as it is towards the edge of the EDFA operating region. The 194.2 THz channel of the SFP laser and the 194.2 THz channel of the SG-DBR laser are chosen for comparison. As shown in Figure 5.8b, a 1 dB penalty at a BER of 1×10^{-9} is experienced by the SG-DBR laser due to its linewidth of 4.6 MHz, compared to the 738 kHz linewidth of the SFP laser. An error floor at 1×10^{-5} is observed when the linewidth of the SG-DBR laser is 19.8 MHz. The received eyes at -41.8 dBm of the SFP laser and the SG-DBR laser with 19.8 MHz linewidth are shown as the insets in Figure 5.8. Figure 5.8b also shows the performance of the SFP laser being transmitted through 24 km of standard single mode fibre (SMF). As expected, the penalty between the curves without fibre and with 24 km of fibre is negligible because at such low data rates the dispersion effect of the fibre is small.

5.2.2 Wavelength Switching

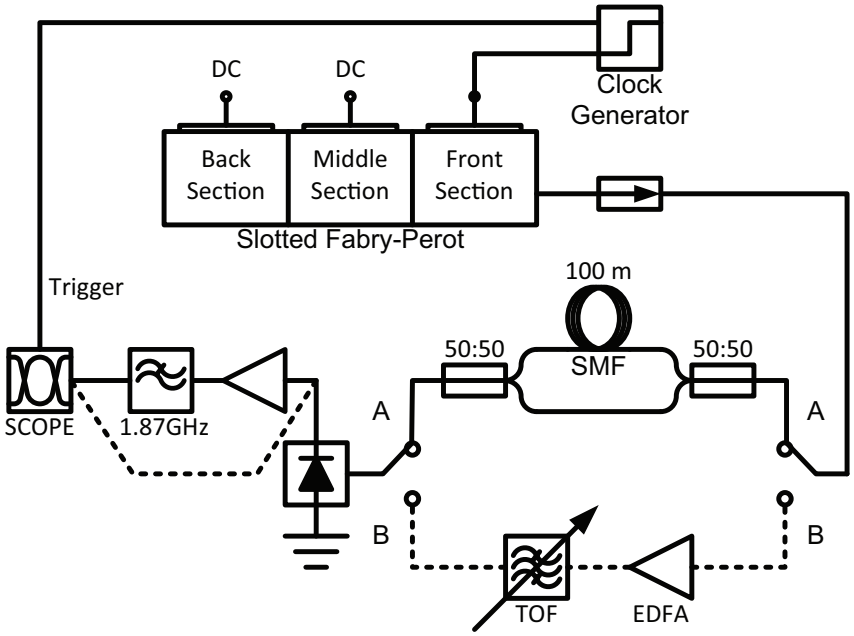

Figure 5.9: Experimental setup of wavelength switching using tunable filter method (dotted line B) and self heterodyne method (solid line A).

Next generation optical networks require nanosecond scale switching times to support fast reconfiguration and optical burst and packet switching. The static characterization in Figure 5.3 shows different modes with a spacing of approximately 200 GHz that are obtained by varying the voltage on either the front section or both the middle and back section simultaneously. In the case of Figure 5.3a, the current on the middle and back section are constantly set at 25.1 mA and 22 mA respectively, and in the case of Figure 5.3b, the current on the front section is 37.4 mA. The hysteresis in wavelength switching between the increase and decrease of the tuning voltage is found to be negligible in these two tuning scenarios. The experimental setup used for wavelength switching is shown in Figure 5.9. By driving the front section with a clock generator from Stanford Research Systems, the emitted wavelength is switched from $\lambda 1$ to $\lambda 7$ and back to $\lambda 1$ (see Figure 5.3a). The period of the square wave was 2.5 μs with a peak-to-peak amplitude (Vpp) of 2.56 V biased at 2.17 V. The rise time of the clock generator was less than 100 ps. A second output of the clock generator with the same waveform was used to trigger the sampling oscilloscope. The same setup is also used to switch the emitted wavelength by driving both the middle and the back section of the SFP laser simultaneously. An electrical power splitter was used at the output of the clock generator and a square wave with a Vpp of 0.225 V biased at 1.485 V was applied on the two sections simultaneously in order to switch the output wavelength between $\lambda 2$ and $\lambda 4$ in Figure 5.3b.

Tunable Optical Filter Method

In order to examine the switching dynamics of different modes, a tunable optical filter (TOF) is used as shown in Figure 5.9 [8] (see the dotted line B). This filter (with a 3 dB bandwidth of 27 GHz) is tuned to the wavelengths of each switching points as shown in Figure 5.9. The filtered signal is then detected by an 11 GHz photoreceiver. The measured electrical signals from the oscilloscope are shown in Figure 5.10. Figures 5.10a and 5.10b shows the transient dynamics when the SFP laser is switched from the point at $\lambda 1$ to the point at $\lambda 7$ in Figure 5.3a. The intermediate modes of $\lambda 2$ to $\lambda 6$ are lasing successively in both forward (see Figure 5.10a) and backward (see Figure 5.10b) switching, which corre-

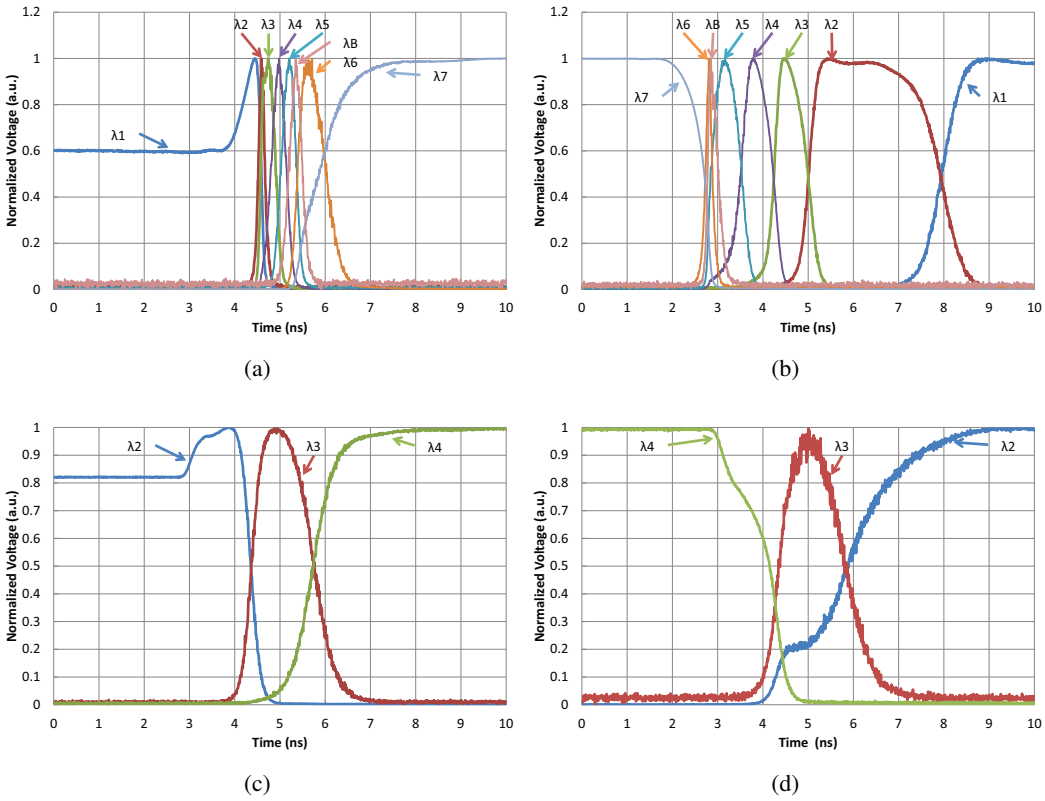

Figure 5.10: Switching waveforms of different modes when the SFP laser is switched from (a) $\lambda 1$ to $\lambda 7$ and (b) $\lambda 7$ to $\lambda 1$ in Figure 5.3a, (c) $\lambda 2$ to $\lambda 4$ and (d) $\lambda 4$ to $\lambda 2$ in Figure 5.3b.

sponds to the increase and decrease of the tuning voltage respectively. The rise in output power at the beginning of the forward switching is due to the increase of voltage between the source and destination mode. We define the switching time as the duration between the time when the power drops to a level of 90% of the maximum of the source mode and the time when the power increases to a level of 90% of the maximum of the destination mode. The switching time between $\lambda 1$ and $\lambda 7$ is approximately 5.66 ns for backward switching and 2.69 ns for forward switching. The backward switching takes a longer time due to the fact that the backward dynamic of carrier density enhances the lasing of the spurious modes $\lambda 2$ to $\lambda 6$ for a longer period (see Figure 3.9), a phenomenon which has also been found in the switching of SG-DBR lasers [9] and Grating assisted co-directional Coupler with Sampled Reflector (GCSR) lasers [10].

The switching of the middle and back section simultaneously is also examined by

switching the emitted wavelength of the SFP laser from the point at $\lambda 2$ to the point at $\lambda 4$ in Figure 5.3b. The forward and backward switching times of these switching combinations are found to be 2.13 ns and 4.41 ns respectively. Despite the larger wavelength difference, the faster switching time observed here is due to the smaller amplitude of the switching voltage, which reduces the number of intermediate modes between the source and the destination mode [11]. These results indicate that nanosecond switching times are feasible when switching one or more sections of the SFP laser simultaneously which will be required to align the emitted wavelength exactly to the ITU grid.

It should also be noted that the residual packets at the mode we are switching from, as well as the intermediate lasing modes, are undesired as they could interfere with the other channels in the dense WDM (DWDM) networks. The laser has to be isolated from the network during the switching to achieve the dark tuning or hitless tuning [12]. An integrated SOA can be used to shutter the output during the switching [13], hence there is no light emitting into the undesired channels before the wavelength sets into the destination channel.

Self-heterodyne Method

In order to more accurately measure how long it takes for the laser to switch to within a certain tolerance of the target frequency ($\sim$2% of a 100 GHz grid), we used the self-heterodyne method as shown in Figure 5.9 (see the solid line A) [14]. The length of the SMF is 100 m which corresponds to a delay of 470 ns. By placing a 1.87 GHz low pass electrical filter after the photodetector, the time required for the laser to get (and remain) within 1.87 GHz of the target frequency when it is switching can be determined.

The detected electrical signal is displayed in Figure 5.11 as the laser is switching between $\lambda 2$ and $\lambda 4$ in Figure 5.3b under the same conditions as described in Fig. 5.10. The DC component corresponds to the time the laser is operating outside the bandwidth of the electrical filter. The differing mean value of the beat signals is due to the fact that the two modes have a different output power. $\lambda 4$ exhibits a higher optical power than $\lambda 2$ because the driving voltage at $\lambda 4$ is 0.45 V higher than that at $\lambda 2$ (see Figure 5.3b). From Figure 5.11

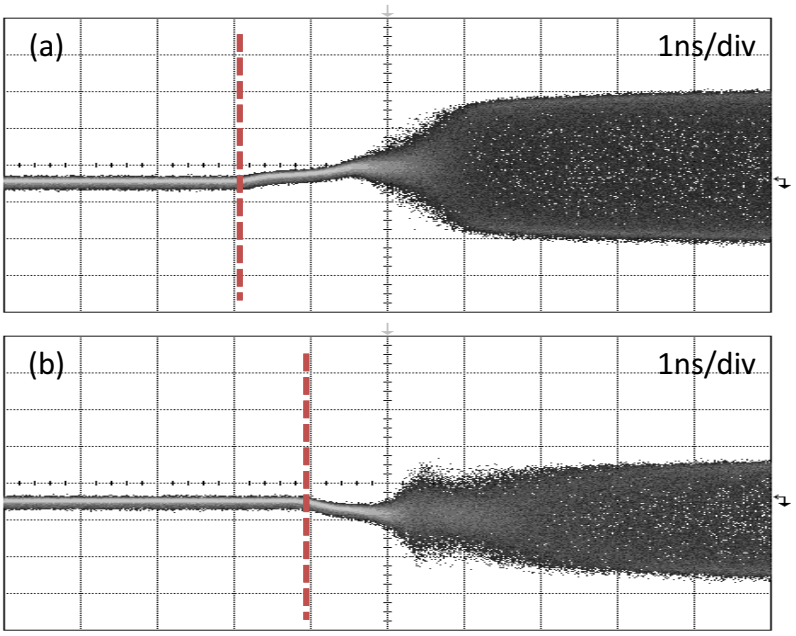

Figure 5.11: Beating signal generated when the laser get into 1.87 GHz range of the target frequency (a) $\lambda 4$ and (b) $\lambda 2$ in Fig. 2 (b). The dotted lines represent the beginning of the switching event.

we can see that the laser has completed its switch to 1.87 GHz of target wavelength ($\lambda 4$) after about 2.9 ns, and it takes about 3.3 ns to complete its switch to target wavelength ($\lambda 2$).

Table 5.1: Switching Combination (TOF Method/Self Heterodyne Method)

(ns)	$\lambda 2$	$\lambda 4$	$\lambda 6$	$\lambda 7$
$\lambda 2$		1.46/3.63	2.18/2.70	1.94/2.00
$\lambda 4$	3.42/3.85		1.09/1.47	1.59/1.26
$\lambda 6$	4.12/4.74	2.74/2.26		1.39/3.36
$\lambda 7$	3.62/6.00	3.01/2.78	1.17/1.77	

Twelve combinations of switching time evaluated from both the TOF and the self-heterodyne measurements between four modes in Figure 5.3a are shown in Table 5.1. The channel names on the vertical row represent the source mode whereas the ones on the horizontal row represent the target mode. A switching time of ≤ 6 ns can be achieved for each

of these switching combinations. Fourteen switching combinations between the modes shown in Figures 5.3a and 5.3b are measured, and the switching time histograms of all of these combinations are shown in Figure 5.12. It can be observed in the histogram that in general forward switching is faster than backward switching. The maximum switching time of the fourteen switching combinations measured is less than 7 ns for both the TOF and the self-heterodyne methods indicating this type of laser's suitability for use as a transmitter in fast wavelength switching systems.

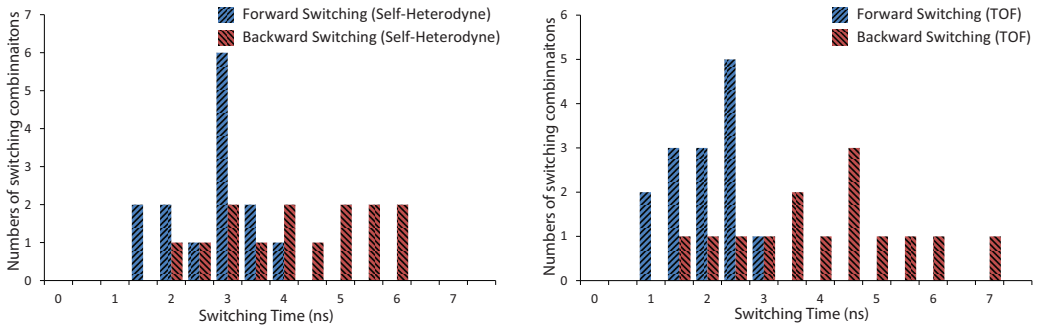

(a) (b)

Figure 5.12: Histogram of the switching time of different switching combinations.

5.2.3 Time Resolved BER

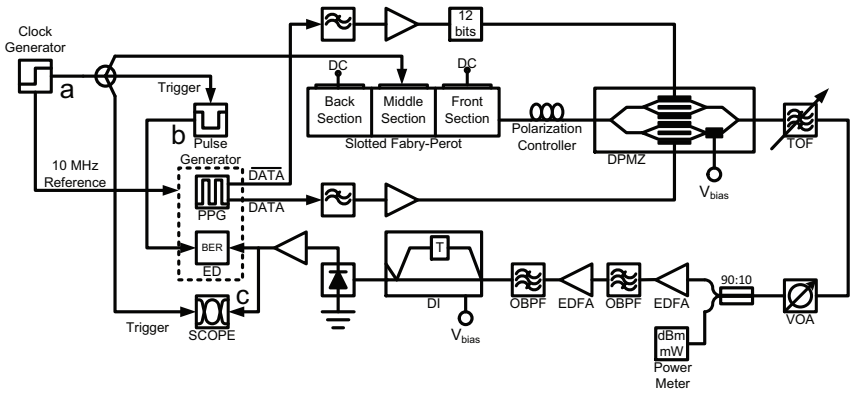

Figure 5.13: Experimental setup of time resolved BER measurement.

Experimental results in Section 4.3 show that the linewidth of the SG-DBR laser is less than 50 MHz when the frequency offset of the laser is stabilized into the range of ± 0.5 GHz. However, for high speed phase shift keying (PSK) systems with the differential detection,

the frequency offset of the SG-DBR laser plays a more important role than the linewidth as demonstrated in Figure 4.17. A guard band of 20 ns is shown to be required for error free transmission in a 10.7 Gbaud DQPSK packet switching system. In order to examine the linewidth dynamics combined with mode transients of the SFP laser, the SFP is employed in the same time resolved BER test bed as the SG-DBR laser and the setup of the test bed is displayed in Figure 5.13. In this case, the SFP laser is switched between two channels at 193 THz and 192.8 THz with 200 GHz spacing and the switching square wave is applied on the middle section alone, with a Vpp of 0.5 V biased at 1.01 V.

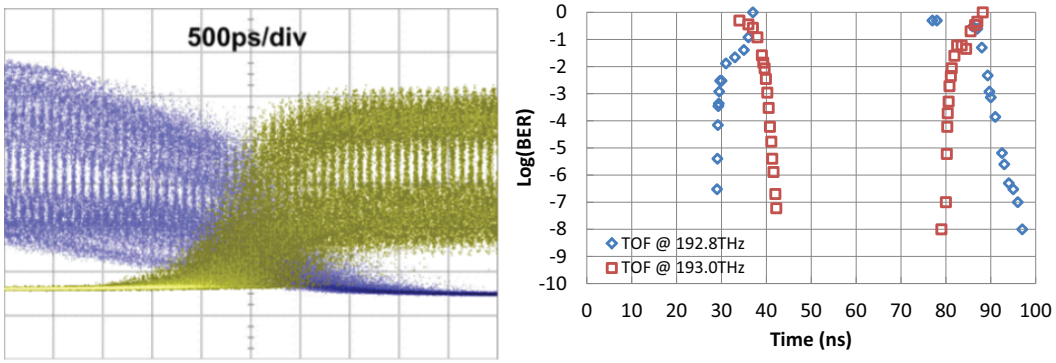

(a) (b)

Figure 5.14: (a) Oscilloscope traces of the in-phase components of received packets at the end of the 192.8 THz packet and the beginning of the 193.0 THz packet. (b). Time resolved BER as the laser switches between 198.2 THz and 193 THz.

By locking the phase of the switching signal to that of the pulse pattern generator (PPG) with a 10 MHz reference signal, it is possible to trigger the sampling oscilloscope such that the packets and the eye diagram could be viewed simultaneously. This is shown in Figure 5.14a for the in-phase component of the end of the 192.8 THz channel packet and the beginning of the 193 THz packet. It is clear from this figure that the eye is open within approximately 2.5 ns of the beginning of the switch between the two channels. Figure 5.14b shows the measured time resolved BER on the two packets. It can be seen that the time taken to go from no measured errors on one channel to no measured errors on the other channel was approximately 16 ns for the forward switching and 12 ns for the backward switching. This time is referred to as latency to differentiate it from the wavelength switching time

discussed in the previous section. Ideally the latency should be as close to the switching time as possible. The reason for the discrepancy between the latency measured and that visible in Figure 5.14a is twofold: First, the threshold of the error detector was optimized for the centre of the packet so power and frequency variation at the beginning and end of the packet can result in errors. Second, the gating window covers a period of approximately 20 bits and as the window position is moved towards the switching event, a portion of it will eventually lie over a time period where the laser is not emitting on the measured wavelength, thereby distorting the error measurement. However the latency of the SFP laser in this DQPSK packet switching system is found to be comparable with a similar SFP laser in an on-off keying (OOK) packet switching system [15], which indicates that the latency in this packet transmission system using the SFP laser is dominated by the wavelength dynamics rather than the linewidth and frequency offset dynamics [16].

5.3 Summary

Compared to the state of the art tunable laser based on grating structures, the two slotted structure with the single growth fabrication process and only standard lithography reduces the cost while increasing the yield. Using the Vernier effect, this type of tunable device is demonstrated to be able to achieve discrete tuning over 25 available channels of 100 GHz ITU grid, with SMSR above 30 dB for all channels. Like discrete mode lasers, this type of tunable laser exhibits much narrower self-heterodyne linewidth compared to the passive tuning DBR-type lasers. Due to the gain-clamping effect, the additional FM-noise is suppressed in the three active sections of the SFP laser. Of the six channels measured a maximum average RIN of -135 dB/Hz indicates that this laser is suitable for high speed modulation of prevalent OOK formats.

Characterization of the laser shows that the linewidth of the device is less than 800 kHz for all the channels. The linewidth is found to be narrower than most of the commercially available tunable lasers characterized by using the delayed self-heterodyne method. By examining the performance of a 1.25 Gb/s DPSK transmission system employing the SFP

laser and the SG-DBR laser, the linewidth benefits of the SFP are demonstrated. Two methods are used to study the switching process of the tunable SFP laser. The appearance of intermediate modes is observed and results in an average switching time of 5 ns for different switching combinations between discrete modes. The time resolved BER of a 10.7 Gbaud DQPSK packet transmission system is also measured with a 2 ns gating pulse. A guard band of less than 20 ns is found to be required for error free transmission from the source to the destination channels. The fast switching speed of the tunable SFP laser, combined with its narrow linewidth and low cost fabrication may make it attractive for future dynamic networks employing advanced modulation formats.

References

[1] S. O'Brien, F. Smyth, K. Shi, J. O'Carroll, P. M. Anandarajah, D. Bitauld, S. Osborne, R. Phelan, B. Kelly, J. O'Gorman, F. H. Peters, B. Roycroft, B. Corbett, and L. P. Barry, "Design, characterization, and applications of Index-Patterned Fabry-Perot lasers," *IEEE Journal of Selected Topics in Quantum Electronics*, vol. 17, no. 6, pp. 1621–1631, Dec. 2011.

[2] R. Phelan, W. Guo, Q. Lu, D. Byrne, B. Roycroft, P. Lambkin, B. Corbett, F. Smyth, L. P. Barry, B. Kelly, J. O'Gorman, and J. F. Donegan, "A novel Two-Section tunable discrete mode Fabry-Perot laser exhibiting nanosecond wavelength switching," *IEEE Journal of Quantum Electronics*, vol. 44, no. 4, pp. 331–337, Apr. 2008.

[3] F. Smyth, E. Connolly, B. Roycroft, B. Corbett, P. Lambkin, and L. Barry, "Fast wavelength switching lasers using Two-Section slotted Fabry-Perot structures," *IEEE Photonics Technology Letters*, vol. 18, no. 20, pp. 2105–2107, Oct. 2006.

[4] D. Byrne, J. Engelstaedter, W. Guo, Q. Y. Lu, B. Corbett, B. Roycroft, J. O'Callaghan, F. Peters, and J. Donegan, "Discretely tunable semiconductor lasers suitable for photonic integration," *Selected Topics in Quantum Electronics, IEEE Journal of*, vol. 15, no. 3, pp. 482–487, 2009.

[5] R. Phelan, B. Kelly, D. Jones, C. Herbert, J. O'Carroll, M. Rensing, B. Cai, A. Kaszubowska-Anandarajah, P. Perry, J. Stopford, P. Anandarajah, L. P. Barry, and J. O'Gorman, "Discrete mode laser diodes with ultra narrow linewidth emission $<$

3kHz," in *Optical Fiber Communication Conference and Exposition and The National Fiber Optic Engineers Conference*. Optical Society of America, 2008, p. OThK5.

[6] B. Roycroft, P. Lambkin, S. Riesner, B. Corbett, and J. F. Donegan, "Transition from perturbed to Coupled-Cavity behavior with asymmetric spectral emission in ridge lasers emitting at 1.55 m," *IEEE Photonics Technology Letters*, vol. 19, no. 2, pp. 58–60, Jan. 2007.

[7] B. Kelly, R. Phelan, D. Jones, C. Herbert, J. O'Carroll, M. Rensing, J. Wendelboe, C. B. Watts, A. Kaszubowska, P. P. Anandarajah, C. Guignard, and L. R. Barry, "Discrete mode laser diodes with very narrow linewidth emission," *Electronics Letters*, vol. 43, no. 23, Nov. 2007.

[8] J. E. Simsarian, M. C. Larson, H. E. Garrett, H. Xu, and T. A. Strand, "Less than 5-ns wavelength switching with an SG-DBR laser," *IEEE Photonics Technology Letters*, vol. 18, no. 4, pp. 565–567, Feb. 2006.

[9] K. Shi, Y. Yu, R. Zhang, W. Liu, and L. P. Barry, "Static and dynamic analysis of side-mode suppression of widely tunable sampled grating DBR (SG-DBR) lasers," *Optics Communications*, vol. 282, no. 1, pp. 81–87, Jan. 2009.

[10] J. E. Simsarian, A. Bhardwaj, J. Gripp, K. Sherman, Y. Su, C. Webb, L. Zhang, and M. Zirngibl, "Fast switching characteristics of a widely tunable laser transmitter," *IEEE Photonics Technology Letters*, vol. 15, no. 8, pp. 1038–1040, Aug. 2003.

[11] Y. Yu and R. O'Dowd, "Influence of mode competition on the fast wavelength switching of an SG-DBR laser," *Journal of Lightwave Technology*, vol. 20, no. 4, pp. 700–704, Apr. 2002.

[12] J. Buus and E. J. Murphy, "Tunable lasers in optical networks," *Journal of Lightwave Technology*, vol. 24, no. 1, pp. 5– 11, Jan. 2006.

[13] L. Ponnampalam, N. D. Whitbread, R. Barlow, G. Busico, A. J. Ward, J. P. Duck, and D. J. Robbins, "Dynamically controlled channel-to-channel switching in a full-band

DS-DBR laser," *IEEE Journal of Quantum Electronics*, vol. 42, no. 3, pp. 223– 230, Mar. 2006.

[14] H. Joseph and D. Sadot, "A novel Self-Heterodyne method for combined temporal and spectral High-Resolution measurement of wavelength transients in tunable lasers," *IEEE Photonics Technology Letters*, vol. 16, no. 8, pp. 1921–1923, Aug. 2004.

[15] F. Smyth, K. Shi, P. M. Anandarajah, B. Roycroft, B. Corbett, F. H. Peters, and L. P. Barry, "Tunable slotted Fabry-Prot lasers for agile optical networks," in *Optical Fiber Communication Conference and Exposition (OFC/NFOEC), 2011 and the National Fiber Optic Engineers Conference*. IEEE, Mar. 2011, pp. 1–3.

[16] J. A. O'Dowd, V. M. Bessler, S. K. Ibrahim, A. J. Walsh, F. H. Peters, B. Corbett, B. Roycroft, P. O. Brien, and A. D. Ellis, "Implementation of a high speed time resolved error detector utilising a high speed FPGA," in *2011 13th International Conference on Transparent Optical Networks (ICTON)*. IEEE, Jun. 2011, pp. 1–4.

Chapter 6

Conclusion and Future Research

Conclusion

Current optical network deployments are starting to replace the silicon-based switch fabric, with optical switching technologies. The commercially available products have been presented by service providers such as Juniper Networks, Intune Networks and Ciena. The phase noise of the laser is vital for the switching systems where advanced modulation formats are employed. In this thesis, the phase noise of two types of electronically controlled tunable lasers are investigated; the sampled-grating distributed Bragg reflector (SG-DBR) laser and the slotted Fabry-Pérot (SFP) laser. The static and dynamic optical linewidth characteristics of these two types of lasers are measured, and can be summarized as follows:

1. **The SG-DBR laser:** The static linewidth of the SG-DBR laser is characterized using a standard delayed self-heterodyne method. The effect of the laser phase noise is also examined in a low speed differential binary phase shift keying (DPSK) systems. A new method is proposed to measure the laser phase noise in the time domain, which can be used to obtain the linewidth dynamics in a wavelength switching event. Additionally, the time resolved bit error rate (BER) of a 10.7 Gbaud differential quadrature phase shift keying (DQPSK) packet switching system is analysed by operating the error detector (ED) in burst mode. A summary of the key results in Chapter 4 are described below:

- A hard error floor at 1×10^{-5} is observed when the linewidth of the SG-DBR laser is 19.8 MHz, while error free transmission is achieved at the linewidth of 4.6 MHz for the same emission wavelength. The results show the importance of including the linewidth into the calibration process.
- The linewith tuning map of the SG-DBR laser measured with the standard delayed self-heterodyne method shows that the linewidth is not correlated with the side-mode suppression ratio (SMSR) but with the voltage of the gain section. A calibration method for SG-DBR lasers only using the voltage across the gain section combined with data processing techniques is developed and applied to characterize two SG-DBR lasers. The technique results in a linewidth reduction of up to 80% compared to techniques that only calibrate for the SMSR and the output power.
- The in-phase and quadrature component of the continuous wave (CW) optical field is recovered using an optical quadrature front end. The phase noise of the laser can then be derived from the instantaneous phase of the optical field. The major advantage of this technique, in contrast to conventional linewidth measurements in the frequency domain, is that this method enables the investigation of laser phase noise dynamics during wavelength switching events. The frequency offset after switching is found to be more important in high speed self-coherent systems, compared with the linewidth dynamics of the SG-DBR laser, in determining the time resolved BER of an DQPSK packet switching system.

2. **The three-section SFP Laser:** In Chapter 5, a new type of monolithic tunable laser fabricated by etching perturbing slots into the laser ridge is presented. The low linewidth and fast switching characteristics of the three-section SFP laser, combined with its low cost fabrication means that it may be suitable for use as a low cost transmitter in a dynamically switched coherent network. A summary of the key characterizations of the SFP laser are described below:

- Two single slots are etched into the ridge waveguide to separate the laser into three independently injected active sections. The middle and back sections are slightly longer than the front section. Therefore, using the Vernier effect, this type of laser is able to generate 25 channels with 100 GHz grid spacings.
- The linewidth of all the 25 channels is found to be less than 800 kHz. A 1 dB penalty at a BER of 1×10^{-9} is found comparing the performance of the SFP laser ($\Delta\nu = 738\text{kHz}$) with the SG-DBR laser ($\Delta\nu = 4.6\text{MHz}$) in a 1.25 Gbit/s DPSK system.
- The switching time of the SFP laser is characterized using the tunable optical filter (TOF) method and the self-heterodyne method. An average switching time of the SFP laser is found to be 5 ns between four discrete modes. The required guard band of the SFP laser in a 10.7 Gbaud DQPSK packet switching system is found to be less than 20 ns.

The narrow linewidth SFP laser can be used for systems with higher order modulation formats with two (or more) bits per symbol in order to achieve higher aggregate data rates with lower speed electronics.

Future Research

The techniques and devices demonstrated in this thesis can be used for further investigation of tunable lasers in coherent optical switching networks. Some of the potential research for the future is described below:

- The linewidth tuning map of the SG-DBR laser can be measured using the optical quadrature front end. The effect of the 1/f and white FM-noise at different current combinations of the SG-DBR laser can be examined in high speed coherent systems with higher order of modulation format such as 16 quadrature amplitude modulation (QAM).
- The linewidth of the SFP laser or other type of lasers can be characterized using

the optical quadrature front end in order to investigate the FM-noise spectrum of the device.

- The two types of tunable lasers can be utilized in fast tuning coherent burst mode receiver to allow higher order of modulation formats to be employed.

Appendix A

List of Publications Arising From This Work

A.1 Referred Journals

1. P. Anandarajah, K. Shi, J. O'Carroll, A. Kaszubowska, R. Phelan, L. Barry, A. Ellis, P. Perry, D. Reid, B. Kelly *et al.*, "Phase shift keyed systems based on a gain switched laser transmitter," *Optics Express*, vol. 17, no. 15, pp. 12 668–12 677, 2009.

2. R. Maher, K. Shi, P. Anandarajah, A. Kaszubowska, L. Barry, and Y. Yu, "Novel frequency chirp compensation scheme for directly modulated SG-DBR tunable lasers," *Photonics Technology Letters, IEEE*, vol. 21, no. 5, pp. 340–342, 2009.

3. K. Shi, Y. Yu, R. Zhang, W. Liu, and L. Barry, "Static and dynamic analysis of side-mode suppression of widely tunable sampled grating DBR (SG-DBR) lasers," *Optics Communications*, vol. 282, no. 1, pp. 81–87, 2009.

4. P. Anandarajah, A. Kaszubowska-Anandarajah, R. Maher, K. Shi, and L. Barry, "Characterization of wavelength tunable lasers for future optical communication systems," *Journal of Networks*, vol. 5, no. 2, pp. 152–157, 2010.

5. R. Maher, K. Shi, L. Barry, B. Kelly, R. Phelan, J. O'Gorman, P. Anandarajah *et al.*,

"Implementation of a cost-effective optical comb source in a WDM-PON with 10.7 Gb/s data to each ONU and 50km reach," *Optics Express*, vol. 18, no. 15, pp. 15 672–15 681, 2010.

6. D. Reid, K. Bondarczuk, K. Dexter, K. Shi, P. Anandarajah, L. Barry, W. Guo, J. O'Dowd, M. Lynch, A. Bradley *et al.*, "Two-photon-absorption-based OSNR monitor for NRZ-PSK transmission systems," *Photonics Technology Letters, IEEE*, vol. 22, no. 5, pp. 275–277, 2010.

7. K. Shi, D. Reid, L. Barry, Y. Yu, and F. Smyth, "Linewidth calibration of SG-DBR lasers," *Photonics Technology Letters, IEEE*, vol. 22, no. 23, pp. 1729–1731, 2010.

8. K. Shi, F. Smyth, P. Anandarajah, D. Reid, Y. Yu, and L. Barry, "Linewidth of SG-DBR laser and its effect on DPSK transmission," *Optics Communications*, vol. 283, no. 24, pp. 5040–5045, 2010.

9. K. Shi, F. Smyth, D. Reid, C. Browning, B. Roycroft, B. Corbett, F. Peters, and L. Barry, "Fast switching slotted Fabry-Perot laser for phase modulated transmission systems," *Journal of Lightwave Technology*, vol. 28, no. 23, pp. 3409–3416, 2010.

10. K. Shi, F. Smyth, D. Reid, B. Roycroft, B. Corbett, F. Peters, and L. Barry, "Characterization of a tunable three-section slotted Fabry-Perot laser for advanced modulation format optical transmission," *Optics Communications*, vol. 284, no. 6, pp. 1616–1621, 2010.

11. C. Browning, K. Shi, F. Smyth, B. Cardiff, P. Anandarajah, and L. Barry, "Performance enhancement of 10gb/s direct modulation optical OFDM by external optical injection," *Optics Communications*, vol. 285, no. 2, pp. 136–139, 2011.

12. S. O'Brien, F. Smyth, K. Shi, J. O'Carroll, P. Anandarajah, D. Bitauld, S. Osborne, R. Phelan, B. Kelly, J. O'Gorman *et al.*, "Design, characterization, and applications of index-patterned Fabry-Perot lasers," *Selected Topics in Quantum Electronics, IEEE Journal of*, no. 99, pp. 1–11, 2011.

13. K. Shi, R. Watts, D. Reid, T. Huynh, C. Browning, A. Prince, F. Smyth, and L. Barry, "Dynamic linewidth measurement method via an optical quadrature frontend," *Photonics Technology Letters, IEEE*, vol. 23, no. 21, pp. 1591–1593, 2011.

14. R. Watts, K. Shi, and L. Barry, "Time-resolved chirp measurement for 100Gbaud test systems using an ideal frequency discriminator," *Optics Communications*, Available online 27 December, 2011.

15. C. Browning, K. Shi, S. Latkowski, P. M. Anandarajah, F. Smyth, B. Cardiff, R. Phelan, and L. P. Barry, "Performance improvement of 10Gb/s direct modulation OFDM by optical injection using monolithically integrated discrete mode lasers," *Opt. Express*, vol. 19, no. 26, pp. B289–B294, Dec 2011.

A.2 Conference Papers

1. K. Shi, P. Anandarajah, D. Reid, F. Smyth, L. Barry, and Y. Yu, "SG-DBR tunable laser linewidth and its impact on advanced modulation format transmission," in *Lasers and Electro-Optics 2009 and the European Quantum Electronics Conference. CLEO Europe-EQEC 2009. European Conference on*. Munich, Germany: IEEE, June 2009, pp. 1–1.

2. L. Barry, C. Herbert, D. Jones, A. Kaszubowska-Anandarajah, B. Kelly, J. O'Carroll, R. Phelan, P. Anandarajah, K. Shi, and J. O'Gorman, "Discrete mode lasers for communications applications," in *Proceedings of the SPIE*, ser. Novel In-Plane Semiconductor Lasers VIII, A. A. Belyanin and P. M. Smowton, Eds., vol. 7230, 2009, pp. 72 300N–72 300N–12.

3. F. Smyth, K. Shi, P. Anandarajah, D. Reid, and L. Barry, "Influence of SG-DBR laser linewidth on 10.7 Gb/s DPSK and OOK transmission," in *Optical Communication, 2009. ECOC'09. 35th European Conference on*. Vienna, Austria: IEEE, September 2009, pp. 1–2.

4. K. Shi, F. Smyth, D. Reid, R. Maher, B. Roycroft, B. Corbett, F. Peters, P. Anandarajah, and L. Barry, "Self-coherent optical transmission using a narrow linewidth tunable slotted Fabry-Perot laser," in *Optical Fiber Communication (OFC), collocated National Fiber Optic Engineers Conference, 2010 Conference on (OFC/NFOEC)*. San Diego, USA: IEEE, March 2010, p. JWA35.

5. K. Shi, F. Smyth, D. Reid, B. Roycroft, B. Corbett, J. Song, P. O'Brien, F. Peters, and L. Barry, "Characterization of a novel three-section tunable slotted Fabry-Perot laser," in *Optical Fiber Communication (OFC), collocated National Fiber Optic Engineers Conference, 2010 Conference on (OFC/NFOEC)*. San Diego, USA: IEEE, March 2010, p. OWU3.

6. F. Smyth, C. Browning, K. Shi, F. Peters, B. Corbett, B. Roycroft, and L. Barry, "10.7 gbd dqpsk packet transmission using a widely tunable slotted Fabry-Pérot laser," in *Optical Communication (ECOC), 2010 36th European Conference and Exhibition on*. Torino, Italy: IEEE, September 2010, pp. 1–3.

7. F. Smyth, K. Shi, P. Anandarajah, B. Roycroft, B. Corbett, F. Peters, and L. Barry, "Tunable slotted Fabry-Pérot lasers for agile optical networks," in *Optical Fiber Communication Conference and Exposition (OFC/NFOEC), 2011 and the National Fiber Optic Engineers Conference*. Los Angeles, USA: IEEE, March 2011, pp. 1–3.

8. C. Browning, K. Shi, F. Smyth, B. Cardiff, P. Anandarajah, and L. Barry, "Direct modulation optical OFDM performance enhancement by external optical injection," in *Lasers and Electro-Optics Europe (CLEO EUROPE/EQEC), 2011 Conference on and 12th European Quantum Electronics Conference*. Munich, Germany: IEEE, May 2011, p. CI1_5.

9. T. N Huynh, K. Shi, F. Smyth, and L. P Barry, "DQPSK optical packet switching using an SG-DBR laser," in *Lasers and Electro-Optics Europe (CLEO EUROPE/EQEC), 2011 Conference on and 12th European Quantum Electronics Conference*. Munich, Germany: IEEE, May 2011, p. CI1_4.

10. C. Browning, K. Shi, S. Latkowski, P. Anandarajah, F. Smyth, B. Cardiff, R. Phelan, and L. Barry, "Performance improvement of 10gb/s direct modulation OFDM by optical injection using monolithically integrated discrete mode lasers," in *Optical Communication (ECOC), 2011 37th European Conference and Exhibition on*. Geneva, Switzerland: IEEE, September 2011, pp. 1–3.

11. T. Huynh, L. Nguyen, K. Shi, and L. Barry, "Coherent phase modulation detection for self-heterodyne phase noise measurement," in *Proceedings of the SPIE*, ser. Optical Transmission Systems, Subsystems, and Technologies IX, X. Liu, Ed., vol. 8309, Shanghai, China, 2011, pp. 830 920–830 920–7.